Spring 1998

Studies of Warm-Core Rings Using a Particle-in-Cell Method

John James Holdzkom II
Old Dominion University

STUDIES OF WARM-CORE RINGS USING A PARTICLE-IN-CELL METHOD

by

John James Holdzkom II
B.S. May 1992, Old Dominion University

A Dissertation submitted to the Faculty of
Old Dominion University in Partial Fulfillment of the
Requirements for the Degree of

DOCTOR OF PHILOSOPHY

OCEANOGRAPHY

OLD DOMINION UNIVERSITY
May 1998

Approved by:

A. D. Kirwan, Jr. (Co-Director of Advisory Committee)

C. E. Grosch (Co-Director of Advisory Committee)

J. A. Adam (Member)

T. B. Gatski (Member)

D. G. Lasseigne (Member)

ABSTRACT

STUDIES OF WARM-CORE RINGS USING A PARTICLE-IN-CELL METHOD.

John James Holdzkom II
Old Dominion University, 1998

Co-Directors of Advisory Committee: Dr. A. D. Kirwan, Jr.
Dr. C. E. Grosch

A particle-in-cell (PIC) model is developed and applied to problems involving the evolution of warm-core rings. Such models are a hybrid of conventional Eulerian and Lagrangian models. They are ideally suited for problems in which a lower layer outcrops to the surface, such as at the boundary of a ring.

The model is developed in three implementations. First, for purposes of model validation, a reduced gravity model is described. The PIC model reproduces the essential characteristics of analytical solutions to the reduced gravity equations and integral invariants are conserved to a high degree. Next, a 1.5-layer model is developed and used to study the effects of environmental forcing on the evolution of warm-core rings. This model incorporates forcing by a prescribed velocity field in the lower layer. Three solution regimes are found by varying components of the forcing. In the first regime, the eddy becomes elliptical and rotates anticyclonically. For solutions in this regime, a relationship between the forcing magnitude and ring rotation rate and ellipticity is obtained. In the second regime, the eddy becomes highly elliptical, sheds satellite vortices and then rotates as in the first regime. This regime has not been reported previously. In the third regime the eddy is stretched into an elongated filament and never reforms into a coherent vortex. The boundaries between these regimes are defined as a function of the forcing velocity components. Finally, the two-layer model is described. This model solves the primitive equations for a two-layer, shallow-water ocean. Thus, no assumptions or restrictions on the flow in either layer need be made. In order to test this model, three new analytical

steady-state solutions to the shallow-water equations are derived. Model results compare favorably to the analytical solutions.

A parallel algorithm for the PIC technique is given. All models were implemented on a parallel processing computer using Message Passing Interface. The parallel implementation of the models virtually eliminates restrictions on resolution, and timings show nearly a one-to-one speed-up with the number of processors with up to 16 processors.

Dedicated to my parents.

ACKNOWLEDGMENTS

This work was supported by the Office of Naval Research under contracts N00014-93-1-0842 and N00014-95-1-0803. I am also grateful for support from the Meredith Family Scholarship during 1996-1997 and from the Center for Coastal Physical Oceanography during 1992-1993. I also acknowledge the provision of computing time on the IBM SP2 at the Maui High Performance Computing Center.

The satellite imagery presented was processed at RSMAS using the DSP software package, which was developed by O. Brown and R. Evans.

I sincerely thank Drs. Denny Kirwan and Chet Grosch for their support throughout my tenure as a student. My experience as their student was enjoyable, as well as extremely educational. I am also thankful to the members of the faculty and staff who had an interest in my education at the Center for Coastal Physical Oceanography. I am especially thankful to the members of my dissertation committee, Dr. John Adam, Dr. Tom Gatski, and Dr. Glenn Lasseigne.

I also wish to thank Denny and Dede Kirwan for their gracious hospitality at their home and during several visits to foreign countries.

I am very fortunate to have shared my graduate experience with many students at the Center for Coastal Physical Oceanography. I especially benefited from sharing offices with Margaret Dekshenieks and David Smith. I also thank Julie Morgan for sharing her office with me daily for a lunch break.

I want to especially thank my family and friends. I appreciate the love, support, and encouragement of Mom, Dad, Chris, Donna, Grant, Jackie and Ryan. I am also grateful to the Janelli, Mulligan, Grossman, Roff, Szumloz, Potoski, Morgan, and Rea families for their encouragement, interest and support. I am fortunate to have made long-lasting friendships with Margaret Dekshenieks, Julie and Paul Morgan, Caitlin Mullen, and David Smith during my tenure as a graduate student.

Research sponsored in part by the Phillips Laboratory, Air Force Material Com-

mand, USAF, through the use of the MHPCC under cooperative agreement number F29601-93-2-0001. The U.S. Government is authorized to reproduce and distribute reprints notwithstanding any copyright notation thereon. The views and conclusions contained in this document are those of the authors and should not be interpreted as necessarily representing the official policies or endorsements, either expressed or implied, of Phillips Laboratory or the U.S. Government.

Contents

List of Tables

List of Figures

1 INTRODUCTION

1.1 Warm–core Rings

Mesoscale eddies are ubiquitous in the world's oceans. They are most often associated with western boundary currents, such as the Gulf Stream and Kuroshio Current, but they are also common near coastal currents and associated with features such as the Loop Current in the Gulf of Mexico and the Antarctic Circumpolar Current in the Southern Ocean. The most-studied eddies are probably those that shed from the Gulf Stream, and increasing our understanding of the dynamics of these eddies is the motivation of this study. However, with suitable scaling and parameter changes, the results could be applied to eddies of any system.

Warm-core eddies form from northward meanders of the Gulf Stream. These meanders may pinch off from the Gulf Stream and form a closed "ring" of anticyclonically rotating fluid containing a core of Sargasso Sea water. They typically last several months and eventually coalesce with the Gulf Stream. Brown et al. [1986] made a statistical study of warm-core rings from analysis of 10 years of satellite data. They found a bi-modal distribution in the lifetime of the rings, with the split at 140 days and an average of 54 and 229 days for short-lived and long-lived rings, respectively. The rings tend to move west-southwestward between the continental shelf break and the Gulf Stream front (the boundary between slope water and the Gulf Stream) at an average of 6.5 cm s^{-1} ($\approx$ 5.6 km d^{-1}). Brown et al. [1986] and Churchill et al. [1986] noted that this is significantly higher than the β-induced transport (i.e., caused by the variation of the Coriolis parameter with latitude) estimated by Nof [1983] for warm-core rings and is approximately equal to the velocity of the mean flow on the slope. Thus, advection is chiefly responsible for the translation of these rings. Brown et al. [1986] discovered that short-lived rings typically

The *Journal of Geophysical Research* was used as the journal model.

form further east than long-lived rings and coalesce with the Gulf Stream near the New England seamounts at about 68° W, which also coincides to a minimum in the distance between the shelf break and the Gulf Stream front. Long-lived rings tend to pass through this area and enter the Middle Atlantic Bight, which is defined as the region of the continental shelf between Cape Cod and Cape Hatteras. Eventually, these rings coalesce with the Gulf Stream near Cape Hatteras, where there exists a minimum in the width of the continental shelf. They calculated an average semi-major radius of 75 km at formation and found that the radius decreased with time until coalescence. During the span of the dataset, Brown et al. [1986] observed an average formation of 8 warm-core rings per year. Auer [1987] made similar findings of ring formation and lifetime statistics from a shorter but slightly more recent dataset.

Warm-core rings contain fluid of Sargasso Sea origin and thus have anomalously high salinity and temperature relative to the surrounding slope waters. Brickman and Ruddick [1990] reported a ring's T-S signal to be 10 to 20 standard deviations away from the mean of the surrounding fluid. The core of Sargasso Sea water also contains fluid with anomalous nutrient and oxygen levels and different biota [Joyce, 1984, Joyce et al. 1984]. Although mixing with the surrounding shelf water does occur, the core of the warm-core ring often remains distinct from the surrounding fluid throughout the lifetime of the ring.

Warm-core Ring 82-B (WCR 82-B), so named because it was the second ring observed to form in 1982, was the focus of the Warm-Core Rings Experiment in 1982 [see JGR, 90(C5), 1985] and is probably the most-studied ring in the history of oceanography. Figure 1 is an image of sea surface temperature in the Middle Atlantic Bight in which WCR 82-B is prominent. Warm Gulf Stream water is being pulled in a filament across the shelf and around WCR 82-B. Evidence of a cyclonic feature can be seen to the southeast of the ring. An older ring, WCR 81-F, is apparent

further to the southwest of WCR 82-B, where it is approaching coalescence with the Gulf Stream. Evans et al. [1985] presented a detailed chronology of the history of WCR 82-B. They observed many interactions between the ring and its surrounding environment and stressed that the ring was not an isolated feature. Brown et al. [1986] compared the characteristics of WCR 82-B to the statistical properties of 10 years of ring data and concluded that WCR 82-B was representative of most rings. Since the Warm-Core Rings Experiment there has been a surge of interest in observations and modeling of rings.

The evolution of mesoscale eddies is important in many aspects. Since they contain water with anomalous temperature and salinity, they are important in heat and salt budgets in the coastal ocean. The velocity structure associated with rings can induce a significant amount of cross-shelf transport by pulling streamers of shelf water offshore and slope water onshore as they traverse along the continental slope. Evans et al. [1985] documented several examples of such streamers associated with WCR 82-B. Churchill et al. [1986] reported on the cross-shelf transport induced as a warm-core ring passed through an array of moorings. They calculated that a typical slope water filament intruding onto the shelf may be responsible for 3-4% of the annual salt budget in the Middle Atlantic Bight and cite one observation of a large filament which could have been responsible for as much as 16% of the annual budget. Joyce et al. [1992] made a detailed study of cross-shelf transport induced by warm-core rings. They estimated that 0.2 – 2 rings per year act as effective agents for cross-shelf transport in the Middle Atlantic Bight. Their estimates indicate that rings play a significant, if not dominant, role in heat, salt, and nutrient budgets in the region. In addition, rings are energetic structures and contain currents of high velocity. They can influence the operations of offshore industries such as petroleum drilling and exploration. Glenn et al. [1990] studied a warm-core ring and forecast its position and characteristics for exploratory deepwater drilling operations off the

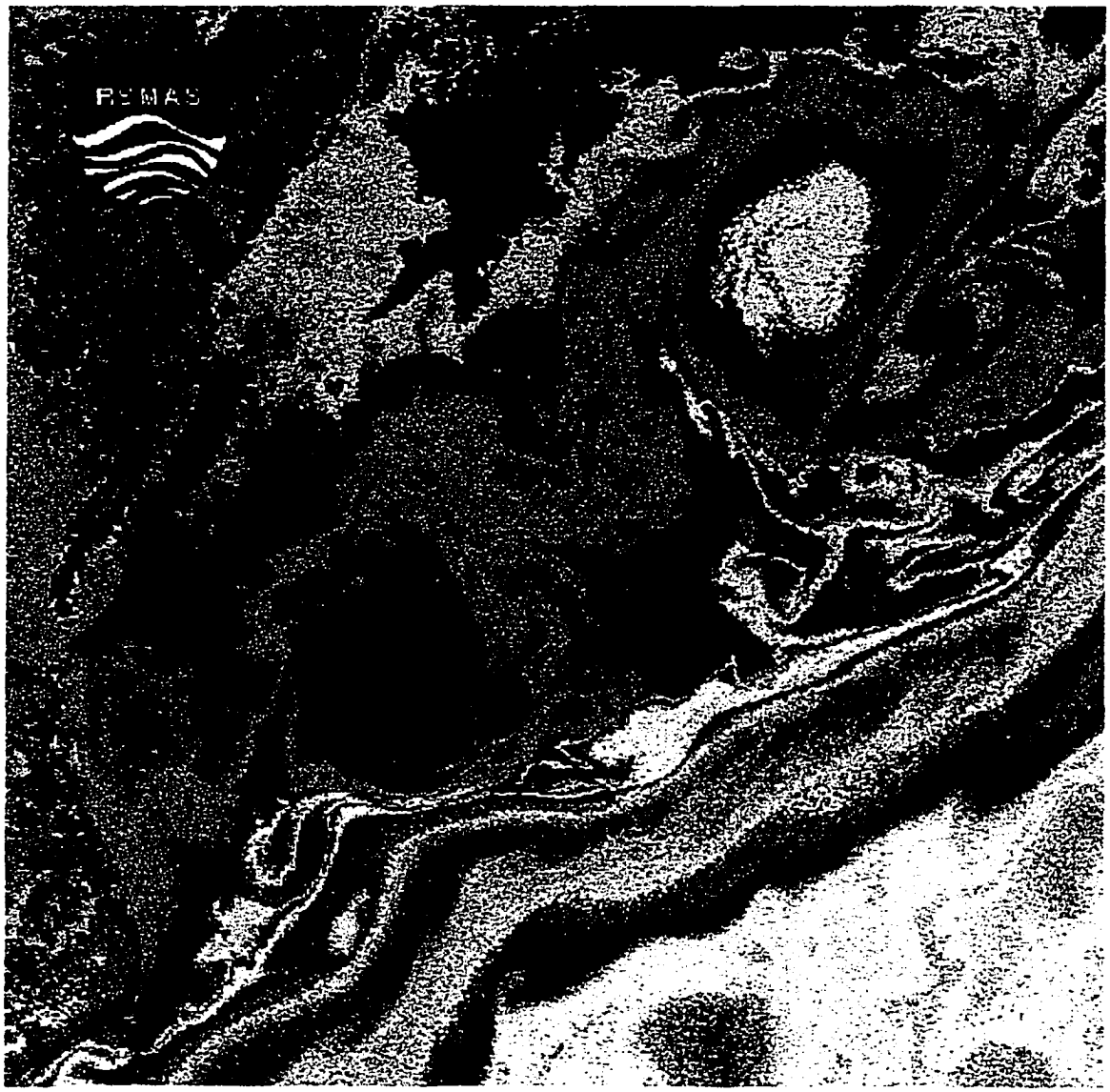

Figure 1: Sea surface temperature image of WCR 82-B in the Middle Atlantic Bight. The coastline of the Mid-Atlantic region of the United States is shown on the left of the figure. The Gulf Stream is passing diagonally across the bottom of the image. WCR 82-B is the light-colored circular feature in the upper right, and an older ring, WCR 81-F, is the darker circular feature offshore of the Chesapeake Bay.

east coast of the United States.

Most studies of warm-core rings treat them as isolated features. Theoretical studies typically consider rings to be comprised of a rotating upper layer lying atop a quiescent lower layer. Observational studies of rings usually focus on the rings themselves and not the properties of the surrounding fluid. However, recent advances in remote sensing technology have revealed a multitude of features resulting from interactions between rings and the coastal ocean and Gulf Stream. In particular, the application of "zebra" palettes, developed by Hooker and Brown [1994], to Advanced Very High Resolution Radiometer (AVHRR) sea surface temperature images shows an abundance of features such as cyclones, small-scale fronts, filaments, mushrooms, and squirts which appear to be associated with mesoscale eddies. The key development was the recognition that warm-core rings are not isolated features and may be significantly influenced by their exterior environment, as well as being a significant influence on that environment.

1.2 Particle-in-Cell Models

Particle-in-cell models are a powerful tool for studying the dynamics of warm-core rings. As in other layered models, the fluid is partitioned into horizontal layers of differing density. In each layer the hydrodynamic variables are assumed to be independent of the vertical coordinate but may vary horizontally. In most layered models in oceanography the evolution of time-dependent surface fronts, such as the boundary of a ring, is a source of great difficulty. At such fronts the lower layer outcrops to the surface, and the upper layer is nonexistent in some region. *A key property of the PIC technique is the ease in which problems with layer outcroppings can be solved.*

Most numerical simulations in oceanography utilize a Eulerian reference frame in which the dynamical equations are solved at fixed grid points or in fixed ele-

ments in a finite domain. The Lagrangian, or particle-following, approach may be more suitable to modeling certain phenomena but introduces difficulties such as the evaluation of spatial differences. Particle-in-cell methods, first developed by Harlow [1964] in plasma simulations, are a hybrid between Eulerian and Lagrangian techniques. With the PIC approach all gradient-type terms in the conservation of mass and momentum equations are computed at fixed grid points while the material derivatives are computed at particles. A critical aspect of the calculation is the interpolation of properties between the grid and the Lagrangian particles. As with other particle methods there is a trade-off between resolution and the number of particles. Since the computational load for large particle numbers increases only linearly with the number of particles for PIC methods, these can be more efficient than most other particle methods, for which the load increases as the square of the number of particles. An excellent general review of PIC and other particle methods is given by Hockney and Eastwood [1988].

As mentioned above, the PIC method easily allows outcropping fronts. The extent of any given layer is simply determined by the envelope of the particles in that layer, and this requires no special calculation or logic. Furthermore, the hybrid nature of the model allows sub-grid scale resolution of front location. An advantage of this high resolution is the potential to initialize the model with high resolution data such as that derived from AVHRR sea surface temperature data and high-frequency active radar data. Such high resolution data typically can not be incorporated into conventional models.

1.3 Objectives

To date, there have been no oceanographic PIC applications with multiple, dynamically complete layers. Most studies have used reduced gravity models, in which the lower layer motion is assumed to be negligible, and thus particles are only dis-

tributed in the active upper layer. The assumption of no lower layer motion excludes a potentially critical source of forcing on the upper layer.

The objective of this study is to develop and test a one-layer, "1.5-layer" and two-layer PIC model and to apply them to realistic problems of interest. The one-layer model will first be described and used for model testing and validation. The 1.5-layer model includes prescribed motion in the lower layer, which is shown to be an important forcing mechanism on the evolution of warm-core rings. The two-layer model incorporates particles in both layers governed by the primitive equations. Thus, no assumptions about the dynamics in either layer need be made. The two-layer model will be capable of resolving gravity waves, which quickly traverse the model domain. Therefore, one component of the study will be to determine and develop boundary conditions most suitable for the PIC model.

The problem to be addressed in this study is the effect of environmental forcing on the characteristics and stability of oceanic eddies. Specifically, the following questions will be addressed:

- How do vorticity, normal and shear deformation in the exterior layer affect the behavior and evolution of a warm-core ring? How do these components affect the ring separately and in combinations?
- Is there some limit to the magnitude and form of the forcing beyond which the ring becomes unstable?
- What specific advantages arise from the use of a particle-in-cell model as opposed to more conventional models?

1.4 Outline of this study

The remainder of this work is organized as follows. Section 2 reviews feature models previously used in oceanography to study warm-core rings and reviews the few

studies which used PIC models. The dynamical equations and modeling technique are discussed in section 3. Model results are presented in section 4. A discussion of the significance of the model results and modeling technique, as well as future applications, follows in section 5. Section 6 contains conclusions and is followed by a two-part appendix including the numerical details of the model and the decomposition and rotational properties of the velocity field utilized in the study.

2 BACKGROUND

2.1 Warm-Core Ring Feature Models

Within the last two decades, several specialized approaches have been developed to study oceanic rings. The resulting techniques have in common the ability to allow layer outcroppings with relative ease. They differ substantially in the form of forcing they allow, solution forms possible, and in their approach. A review of three of these specialized techniques follows.

Cushman-Roisin et al. [1985] introduced what is called here the lens equation solution. A lens is described as a finite volume of water, shaped as an elliptic paraboloid, lying atop a more dense lower layer. As shown by Kirwan and Liu [1991] the mass and velocity fields of the lens may be decomposed into deformation, divergence and vorticity components. Substitution of this decomposition into the reduced-gravity, shallow water equations results in eight nonlinear, coupled ordinary differential equations which describe the evolution of the velocity and mass fields of the lens. Usually this solution is described numerically, although a few exact analytical solutions have been found for special cases. This approach has the advantage of being relatively simple, but the disadvantage of restrictions on geometry and the form of the velocity and height fields. The velocity and height fields are required to be linear and parabolic, respectively, for all time. These requirements are somewhat restrictive, however, the solution is still useful for studying the basic properties of warm-core rings. The solutions of the lens equations are useful for evaluating other models, and in fact were used to test the models developed for this study. The lens solution is also limited by its ability to only represent monopoles and to only include simplified forcing.

The so-called "modon model" has been used extensively to study the dynamics of warm-core rings [e.g., Hooker et al., 1995]. A modon is an exact solution to the

quasi-geostrophic potential vorticity equations, in which the potential vorticity is piecewise continuous and uniquely related to the stream function. See Mied et al. [1992], Lipphardt [1995], and Kirwan et al. [1997] for details of the solution method. These solutions offer the advantage of representing rings as multi-pole structures. Furthermore, both baroclinic and barotropic modons may be represented. A disadvantage to the approach is its quasi-geostrophic nature. Ageostrophic dynamics are likely important to the evolution of rings but can not be included by the modon solution.

Point vortex models have also been used to study warm-core rings and between this and the aforementioned techniques, they are the most similar to particle-in-cell models. Hooker and Brown [1994] describe a point vortex model used to study WCR 82-B. Like PIC models, this model takes advantage of both Lagrangian and Eulerian reference frames. However, as noted by Pavia and Cushman-Roisin [1988] point vortex models differ from PIC models in that they require an integration, of vorticity, rather than a differentiation, of height. In addition, the point vortex models requires that a Poisson equation be solved at each time step. Point vortex methods suffer from being computationally expensive. Typically, for N point vortices they require on the order of N^2 operations per time step. Particle-in-cell models require only a small multiple of N operations per time step and thus scale much more easily.

Particle-in-cell models eliminate many of the restrictions of the above-mentioned approaches. The two-layer model uses the shallow-water primitive equations, thus allowing baroclinic and ageostrophic dynamics. The model may be configured to include a number of features with complex geometries including monopoles, dipoles, filaments, and jets. Furthermore, no assumptions need be made about the solution form, so restrictions on the geometry of the features are eliminated. Finally, the forcing can be quite general, and, although not implemented in this study, could include wind and topographic effects. One criticism of PIC models might be that

they are somewhat computationally intensive. Although it is not required, they are best run on supercomputers, especially for large problems with high resolution. However, PIC models compare favorably to point vortex and other particle methods with respect to complexity and computational expense.

2.2 Previous PIC Models in Oceanography

Despite the potential advantages of the method, the number of previous applications of the PIC method in oceanography is quite limited. Pavia and Cushman-Roisin [1988] pioneered the field by developing a PIC model with the dynamically simplified frontal geostrophic equations [Cushman-Roisin, 1986a]. Those equations are applicable to large eddies (three or more times the deformation radius) evolving over long time scales (days to months). Later, they extended the model to the reduced-gravity primitive equations and studied the merging of eddies with both the frontal geostrophic and primitive equations models [Pavia, 1989; Pavia and Cushman-Roisin, 1990]. Mathias [1992] extended a similar model to include a lower layer in quasi-geostrophic balance. This used particles only in the upper layer, while the lower layer was modeled using standard finite difference techniques. Recently, a group of scientists at Centro de Investigación Cientifica y de Educación Superior de Ensenada (CICESE) have developed a variation of the reduced gravity model that allows for horizontal inhomogeneities in the upper layer [Pavia et al., submitted; Ochoa et al., submitted]. This modification allows the incorporation of simplified thermodynamics in studying the stability of warm-core rings.

3 METHODS

3.1 Dynamical equations

3.1.1 Two-layer equations

As discussed in section 1.3, the model was implemented in three forms: one-layer, 1.5-layer, and two-layer. The two-layer model is most general, and those equation will be developed first. Subsequently, the 1.5-layer and one-layer model equations will be described in sections 3.1.2 and 3.1.3, respectively.

The dynamical basis for the applications considered here are the hydrodynamic equations for a two-layer fluid in a steadily rotating coordinate system. Following the notation of Hurlburt and Thompson [1973] these are,

$$\frac{d\mathbf{v}_1}{dt} + \mathbf{k} \times f\mathbf{v}_1 = -g\nabla(h_1 + h_2 + D) + \frac{\tau_S - \tau_I}{\rho_1 h_1} + A_h \nabla^2 \mathbf{v}_1, \tag{1}$$

$$\frac{dh_1}{dt} + h_1 \nabla \cdot \mathbf{v}_1 = 0, \tag{2}$$

$$\frac{d\mathbf{v}_2}{dt} + \mathbf{k} \times f\mathbf{v}_2 = -g\nabla(h_1 + h_2 + D) + g_* \nabla h_1 + \frac{\tau_I - \tau_B}{\rho_2 h_2} + A_h \nabla^2 \mathbf{v}_2, \tag{3}$$

$$\frac{dh_2}{dt} + h_2 \nabla \cdot \mathbf{v}_2 = 0, \tag{4}$$

where,

$$\frac{d}{dt} = \frac{\partial}{\partial t} + \mathbf{v}_i \cdot \nabla.$$

In these equations, $\mathbf{v}_i$ is the horizontal velocity vector for layer i; $\mathbf{k}$ is the vertical unit vector; f is the Coriolis parameter; g is the gravity constant; h_i are the instantaneous layer thicknesses; D is the bottom topography; τ_j are the stresses at the surfaces $j = S$ (upper surface), I (interface between the layers), and B (bottom surface); ρ_i

are the constant densities of each layer; A_h is the total horizontal viscosity coefficient; and $g_* = g(\rho_2 - \rho_1)/\rho_2$ is "reduced" gravity.

In the flat bottom case with no surface stresses, equations (1) and (3) reduce to

$$\frac{d\mathbf{v}_1}{dt} + \mathbf{k} \times f\mathbf{v}_1 = -g\nabla(h_1 + h_2) + A_h\nabla^2\mathbf{v}_1, \tag{5}$$

$$\frac{d\mathbf{v}_2}{dt} + \mathbf{k} \times f\mathbf{v}_2 = -g\nabla(h_1 + h_2) + g_*\nabla h_1 + A_h\nabla^2\mathbf{v}_2. \tag{6}$$

It is appropriate to non-dimensionalize (5) and (6) with a scheme similar to that used by Cushman-Roisin et al. [1985]. Thus, h is scaled by H (representative layer thickness), ∇ by $f/\sqrt{gH}$, time by f^{-1}, and $\mathbf{v}_i$ by $\sqrt{gH}$. The resulting non-dimensional equations describe the two-layer model used in this study:

$$\frac{d\mathbf{v}_1}{dt} + \mathbf{k} \times \mathbf{v}_1 = -\nabla(h_1 + h_2) + A_h\nabla^2\mathbf{v}_1, \tag{7}$$

$$\frac{d\mathbf{v}_2}{dt} + \mathbf{k} \times \mathbf{v}_2 = -\nabla(h_1 + h_2) + \delta\nabla h_1 + A_h\nabla^2\mathbf{v}_2, \tag{8}$$

where δ is the ratio $(\rho_2 - \rho_1)/\rho_2$, which is typically $O(10^{-3})$. The scaled, non-dimensional viscosity coefficient, A_h, was taken to be 1×10^{-5}, which corresponds to a dimensional value of 10^3 m^2 s^{-1}. This coefficient represents the sum of the turbulent and molecular viscosities; however, this sum is dominated by the turbulent viscosity coefficient. A brief note about the sensitivity of the model results to this parameter is made in section 4.3.2.

Since this problem is solved with a particle method the equations must be augmented by two path equations in each layer:

$$\frac{d\mathbf{x}_1}{dt} - \mathbf{v}_1 = 0, \tag{9}$$

$$\frac{d\mathbf{x}_2}{dt} - \mathbf{v}_2 = 0, \tag{10}$$

where $\mathbf{x}_i$ is the position vector in layer i.

The two-layer model incorporates particles in both layers governed by equations (7) – (10). In the PIC technique the particles conserve their height throughout the simulation; thus, equations (2) and (4) are satisfied identically and need not be solved.

3.1.2 1.5-layer equations

The two-layer model described above can be simplified significantly if flow in the lower layer is prescribed. This is commonly referred to as a 1.5-layer model. Generally, flow in the lower layer will be dependent on upper layer motions, but in cases in which the lower layer is much deeper than the upper, changes in the upper layer make only a negligible affect on the lower layer. In this case, flow in the lower layer can be prescribed to be independent of upper layer motions. Mathematical details of the decoupling of the layers is given below. Laboratory studies by Brickman and Ruddick [1990] suggested that this assumption is not unrealistic. In addition, viscosity was not used in the model results presented below for the 1.5-layer model; i.e., $A_h = 0$. The study by Olson et al. [1985] suggests that ring dynamics are nearly inviscid, especially in the ring core.

It is convenient to decompose the lower layer velocities into divergence, rotation, normal and shear deformation components. Thus, the lower layer velocities are prescribed as,

$$u_2 = (G/2 + G_N)x + (G_S - G_R)y, \tag{11}$$

$$v_2 = (G_S + G_R)x + (G/2 - G_N)y, \tag{12}$$

where G, G_N, G_S, and G_R are the divergence, normal and shear deformation and rotational components, respectively. This specification assumes linearity in x and y with the origin aligned with the center of the ring. It represents deviations from a mean background flow that might be advecting the eddy along the continental shelf; i.e., the mean flow has been removed for this study. Substituting (11) and (12) into (8), equation (8) (with $A_h = 0$) can be rewritten as,

$$\begin{aligned} -\frac{\partial(h_1+h_2)}{\partial x} &= -\delta\frac{\partial h_1}{\partial x} + [(G/2+G_N)x + (G_S-G_R)y](G/2+G_N) \\ &\quad +[(G_S+G_R)x + (G/2-G_N)y](G_S-G_R) \\ &\quad -[(G_S+G_R)x + (G/2-G_N)y], \end{aligned} \tag{13}$$

$$\begin{aligned} -\frac{\partial(h_1+h_2)}{\partial y} &= -\delta\frac{\partial h_1}{\partial y} + [(G/2+G_N)x + (G_S-G_R)y](G_S+G_R) \\ &\quad +[(G_S+G_R)x + (G/2-G_N)y](G/2-G_N) \\ &\quad +[(G/2+G_N)x + (G_S-G_R)y]. \end{aligned} \tag{14}$$

This can then by substituted into equations (7) to give,

$$\frac{d\mathbf{v}_1}{dt} + \mathbf{k}\times f\mathbf{v}_1 = -\delta\nabla h_1 + \mathbf{F}, \tag{15}$$

where from (13) and (14),

$$\begin{aligned} F_x &= [(G/2+G_N)x + (G_S-G_R)y](G/2+G_N) + [(G_S+G_R)x \\ &\quad +(G/2-G_N)y](G_S-G_R) - [(G_S+G_R)x + (G/2-G_N)y], \end{aligned} \tag{16}$$

$$\begin{aligned} F_y &= [(G/2+G_N)x + (G_S-G_R)y](G_S+G_R) + [(G_S+G_R)x \\ &\quad +(G/2-G_N)y](G/2-G_N) + [(G/2+G_N)x + (G_S-G_R)y]. \end{aligned} \tag{17}$$

With the prescription of lower layer flow, no particles are needed in the lower layer. Thus, there are only path equations for the upper layer. Equations (15) and (9) comprise the 1.5-layer model.

This model has the advantage of including flow in the exterior layer without requiring particles to be placed there. Thus, the total number of particles is greatly reduced, typically by an order of magnitude, from that in the complete two-layer model. The disadvantage, of course, is the assumption of independence between flow in the two layers. Only the upper layer may evolve dynamically.

3.1.3 Reduced gravity equations

The reduced gravity, or one-layer, model is formulated by requiring the lower layer to be motionless. Then, equations (8) reduce to,

$$-\frac{\partial(h_1+h_2)}{\partial x} = -\delta\frac{\partial h_1}{\partial x} \tag{18}$$

$$-\frac{\partial(h_1+h_2)}{\partial y} = -\delta\frac{\partial h_1}{\partial y}. \tag{19}$$

This can be substituted into equations (7) to give, after a non-dimensionalization similar to that used above,

$$\frac{d\mathbf{v}_1}{dt} + \mathbf{k}\times\mathbf{v}_1 = -\nabla h_1, \tag{20}$$

$$\frac{dh_1}{dt} + h_1\nabla\cdot\mathbf{v}_1 = 0. \tag{21}$$

As in the model with prescribed flow, no particles are necessary in the lower layer and the the particle path equations are given by (9). Results from the reduced gravity model are presented in section 4.2 for purposes of model validation. The model was extensively tested and described in Kirwan et al. [1997].

3.1.4 Lens Equations Solution

In the reduced gravity and 1.5-layer form, solutions to the PIC model can be compared to those of a simple analytic lens solution. This solution was first introduced by Cushman-Roisin et al. [1985] and has since been the subject of a considerable number of studies [e.g. Brickman and Ruddick, 1990, Ruddick 1987, Cushman-Roisin 1987, Kirwan and Lipphardt 1993, Kirwan et al. 1992, 1994, Kirwan and Liu 1991, Ripa 1987, Rogers 1989, Young 1986 and Holdzkom et al. 1995]. In these studies the lens thickness and velocity were specified as,

$$h = h_0(t) + B_{ij}(t)x_i x_j, \quad h \geq 0 \tag{22}$$

$$\begin{aligned} v_i &= G_{ij}(t)x_j, \quad h \geq 0 \\ &= 0. \qquad\quad h < 0 \end{aligned} \tag{23}$$

As shown in Kirwan and Liu [1991], the mass and velocity components can be represented as a nonlinear superposition of rotational, deformational and horizontal divergence modes. This decomposition is also reviewed for the velocity field in appendix B. Substitution of (22) and (23) into (15) yields 8 coupled nonlinear ordinary differential equations for $G_{ij}(t)$, $h_0(t)$ and $B_{ij}(t)$ (note that $B_{ij} = B_{ji}$). The resulting equations are,

$$\dot{h}_0 + h_0 G = 0, \tag{24}$$

$$\dot{B} + 2[BG + 2(B_N G_N + B_S G_S)] = 0, \tag{25}$$

$$\dot{B}_S + 2B_S G + G_S B - 2B_N G_R = 0, \tag{26}$$

$$\dot{B}_N + 2B_N G + G_N B + 2B_S G_R = 0, \tag{27}$$

$$\dot{G} + G^2/2 + 2(G_N^2 + G_S^2 - G_R^2 - G_R + B) = \mathcal{L}_\mathcal{G}, \tag{28}$$

$$\dot{G}_R + GG_R + G/2 = 0, \tag{29}$$

$$\dot{G}_N + GG_N - G_S + 2B_N = \mathcal{L}_\mathcal{N}, \tag{30}$$

$$\dot{G}_S + GG_S + G_N + 2B_S = \mathcal{L}_\mathcal{S}. \tag{31}$$

where the overdot denotes a time derivative and $\mathcal{L}_\mathcal{G}, \mathcal{L}_\mathcal{N}, \mathcal{L}_\mathcal{S}$ are forcing terms which can be calculated given the exterior flow. The lens boundary is restricted to be elliptical (including circular) for all time. Furthermore, the height field must be parabolic and the velocity field linear for all time. These 8 coupled equations can be solved using any standard numerical integrator. Here, a 4th-order Runge-Kutta solver was employed. Solutions to these equations will be referred to as lens equation solutions, or lens solutions, in this study.

3.2 Invariants

In the reduced-gravity formulation, Ball [1963, 1965] showed that there are five invariants for a lens. The first four are volume, V_T, angular momentum, L, energy, E, and potential vorticity, Q. These are given by,

$$V_T = \int h dA, \tag{32}$$

$$L = \int [xv - yu + (x^2 + y^2)/2] h dA, \tag{33}$$

$$E = \int (h/2)[u^2 + v^2 + h] dA, \tag{34}$$

$$Q = \int hF(q)dA, \quad q = (1 + \partial v/\partial x - \partial u/\partial y)/h, \tag{35}$$

where F is an arbitrary function of q. The fifth invariant is a nonlinear function involving the other invariants and will not be used in this study.

In the PIC paradigm, (32) is conserved exactly as the particles conserve their volume and the number of particles is invariant. Since velocity and position data are known for each particle, the angular momentum invariant can be calculated by summing the contribution from all particles. The energy invariant must be calculated in two steps. First, the kinetic energy is calculated from the velocity data at the particles. Then, the potential energy is calculated from the gridded height data. The sum of the two is the total energy. Calculation of the potential vorticity invariant poses a problem with the PIC method. Since velocity data is known only at the Lagrangian particles, calculation of the velocity gradients is difficult. Experimentation was done to interpolate velocity data to the grid in order to calculate the potential vorticity invariant. Even with gridded velocity data, evaluation of (35) is difficult because of the velocity discontinuity at the edge of the lens. This difficulty can be partially overcome by converting (35) to a contour integral using Stokes Theorem. However, then logic must be added to the code to locate the time-varying boundary of the lens. This code was added to the reduced gravity model for experimental purposes. The results indicated that (35) was conserved to within 5% over a 30 day model simulation. However, some of this error may be attributed to the difficulty in locating the lens boundary and evaluation of the contour integral about it. Since a significant amount of code was required solely for evaluation of (35), it was not evaluated for most of the model simulations reported below. Cushman-Roisin [personal communication] has proposed a modification to the PIC technique to guarantee exact conservation of potential vorticity. Progress on this modification has not been reported to date.

3.3 PIC Paradigm

As noted in section 1.2, PIC methods take advantage of both Lagrangian and Eulerian reference systems. As the Lagrangian particles move within a Eulerian grid, the body forces, such as local acceleration and Coriolis, are calculated at particles, while gradient-type terms, such as the height gradients, are calculated on a fixed grid. This amounts to calculating the terms on the left-hand-side of equations (7) and (8) (or equation (15) or (20) in the 1.5-layer and reduced gravity cases, respectively) at the particles and terms on the right-hand-side of the equations on the grid. Interpolation between the particles and the grid occurs at each time step. The volume and height of each particle is constant throughout the calculation, thus equations (2) and (4) are satisfied identically and need not be calculated.

The height gradients are determined by interpolating the height of each particle to the grid, calculating finite differences, and then interpolating those gradients back to the particles. Typically, a grid is required for each active layer. The PIC algorithm can be summarized as follows:

1. interpolate the heights of the particles to the grid,
2. calculate the finite difference approximation to ∇h_i on the grid,
3. interpolate ∇h_i from the grid to the particles,
4. integrate (7) – (10) from t to $t + \delta t$ using an appropriate integrator.

In the above, $i = 1, 2$ designates the layer number. Equations (7) – (8) are replaced by (15) or (20) in the 1.5-layer or reduced gravity case, respectively. This yields the position and velocity of each particle at the new time, and the process is repeated for the desired length of simulation.

3.4 Key PIC properties

There are several key differences between the approach used here and that used in previous PIC oceanographic studies. This approach is more rigorous in the derivation and application of interpolation between the particles and grid. Hockney and Eastwood [1988] identify two rules that tests with the reduced gravity model show are very important. First, the same interpolation weights must be used going to the grid from the particles as from the grid back to the particles. Second, the order of accuracy of the spatial finite difference derivatives must not be greater than that of the interpolation weights. If these rules are not enforced, the interpolation and difference operations produce a "self-force" at each particle. This causes each particle to be forced by its own contribution to the pressure gradient. Momentum then is not conserved. (See Kirwan et al. [1997] for the mathematical details of this self-force rule.) In other PIC models the first rule is upheld, being the simplest way to interpolate, but the second rule is not.

Also unlike previous oceanographic PIC studies, this study uses triangular-shaped-cloud (TSC) interpolation weights [Hockney and Eastwood, 1988]. These weights are explicitly given by the fraction of a particle overlapping each cell. Thus, assignment of particle volume and shape is not independent from the derivation of interpolation weights. As in prior approaches, each particle is assigned a finite volume where the total volume of the particles in a given layer is the same as the initial volume of that layer, and the height field on the grid is the sum of the interpolated particle heights. The particle shape used here is different from that of the finite volume particles used by many others, thus it is discussed in detail below. The height equation for a particle is defined as,

$$z_p = h_p(1 - |\xi_x|/\Delta)(1 - |\xi_y|/\Delta), \tag{36}$$

where $(\xi_x,\ \xi_y)$ are the component distances of the center of mass from the nearest cell center and Δ is the width of a grid cell. Note that $|\xi_x|,\ |\xi_y| \leq \Delta$. Each particle has an apex height, h_p, coincident with the horizontal position of its center of mass, and its height decays to zero at its boundaries. Figure 2 is a perspective of this shape. In general, the apex height varies between particles. Each particle has a square base with sides of length 2Δ. Therefore, it influences an area equal to four cells and generally will overlap into nine grid cells. Its location is specified by the coordinates of its center of mass.

The interpolation weights are determined as follows. First, consider the cross-section of a particle taken along the x-axis. As shown in figure 3, the particle will generally overlap into three grid cells. From (36), the normalized cross-sectional area of the particle overlying each cell can be shown to be,

$$\begin{aligned} w_{j-1} &= (1/2 - \xi_x/\Delta)^2/2, \\ w_j &= \{1 - (1/2)[1/2 + 2(\xi_x/\Delta)^2]\}, \\ w_{j+1} &= (1/2 + \xi_x/\Delta)^2/2, \end{aligned} \tag{37}$$

where the normalization factor is the cross-sectional area of the particle. The interpolation of the height of this particle to the overlapped cell centers is then given by $h_p w_{j-1}$, $h_p w_j$, $h_p w_{j+1}$ for the $j-1$, j, and $j+1$ cells, respectively. The hatched, open, and cross-hatched areas in figure 3 show how the height is partitioned at the three grid points.

The two-dimensional weights are simply the product of the one-dimensional weights in each direction. For a particle p this is,

$$w_p(\xi_x^p, \xi_y^p) = w_i(\xi_x^p) w_j(\xi_y^p). \tag{38}$$

Finally, the height at the ith, jth cell center is the weighted sum of all particles overlapping the cell. This is given by,

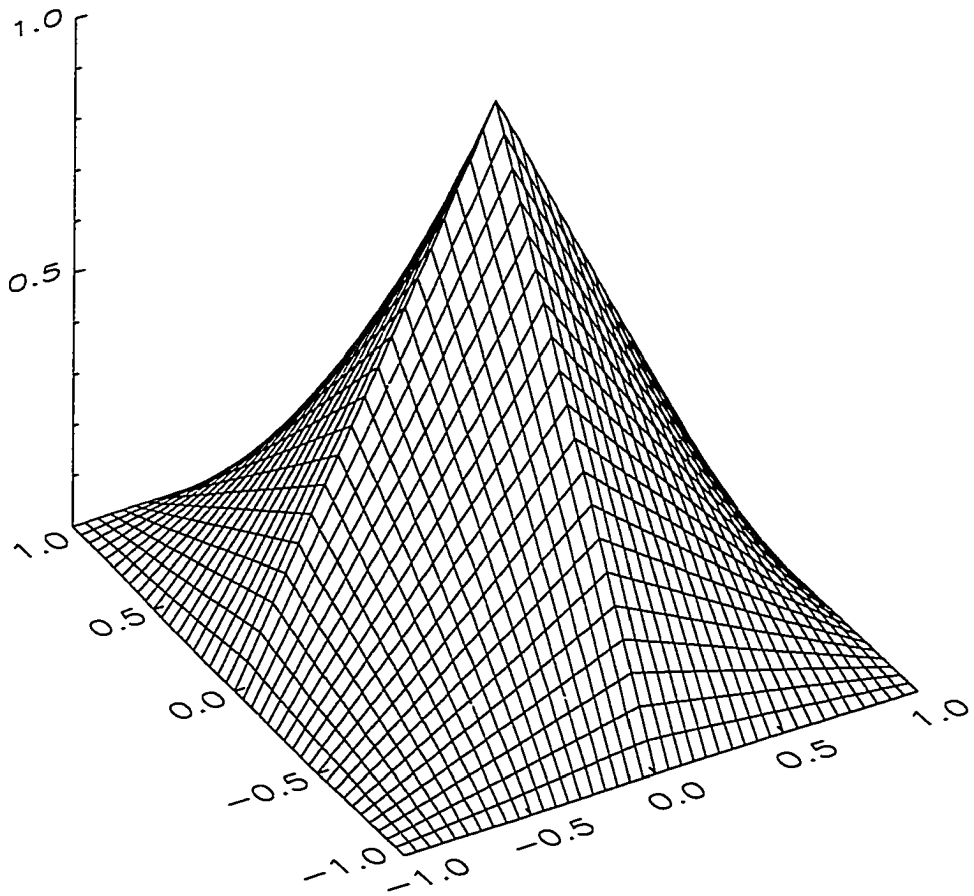

Figure 2: Perspective of the particle shape.

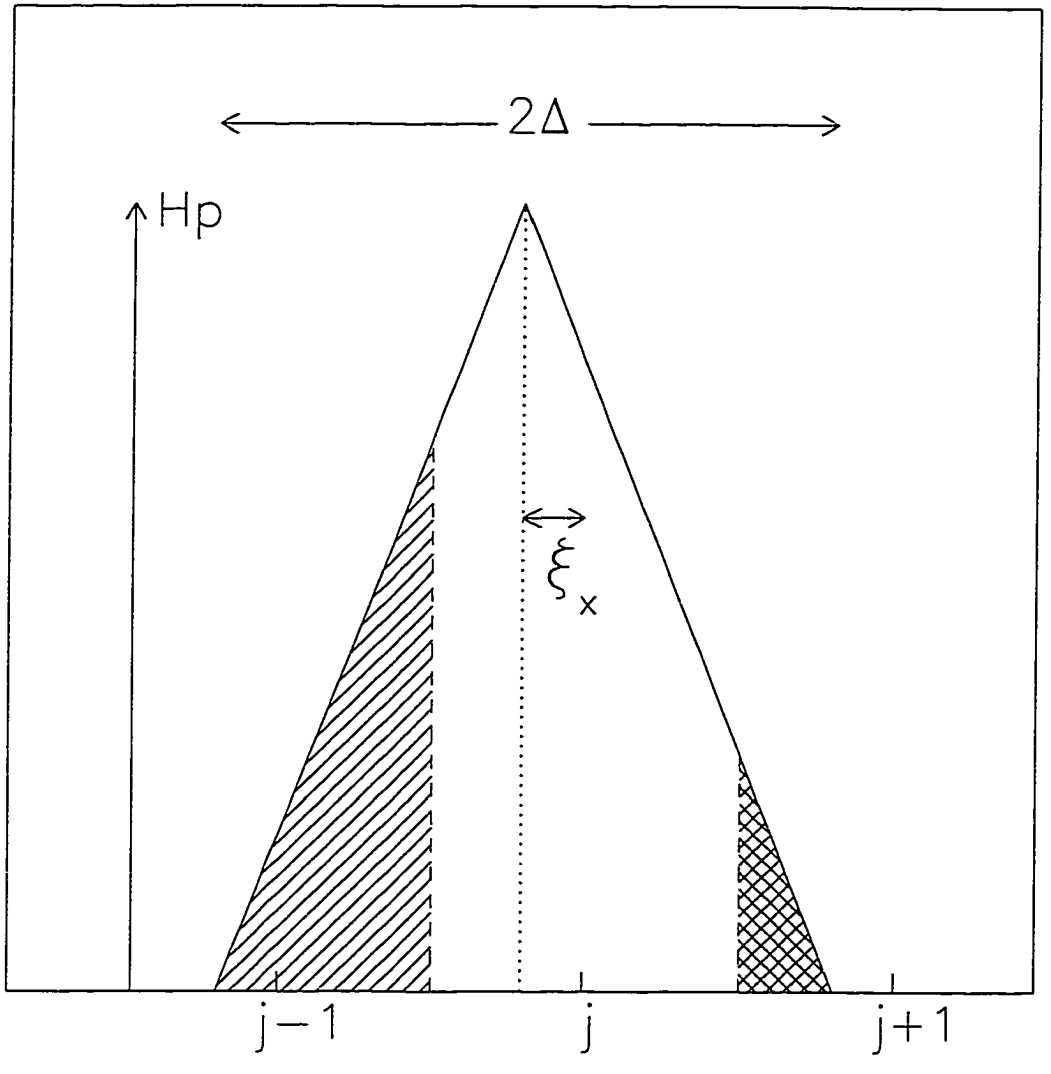

Figure 3: Cross-section of a particle along the x-axis. The hatched, open, and cross-hatched areas indicate the areas partitioned to each of the grid cells $j-1, j$ and $j+1$, respectively. The vertical dashed lines indicate the boundary of the cells.

$$h_{i,j} = \sum_{p=1}^{N_{i,j}} w_p h_p, \tag{39}$$

where p is the particle number and $N_{i,j}$ is the number of particles that overlap into cell i, j. After the heights of all particles are interpolated to the grid, second order accurate gradients are calculated and then interpolated back to the particles using the same weights. It should be noted that in evaluating (39), a census of the particles need not be taken to determine which particles influence which grid points. Rather, the interpolation is performed for all particles. Only the nearest grid point to a particle must be determined, then the height of the particle is interpolated to the surrounding grid points (9 grid points, in general). When this is completed for all particles, (39) will have been evaluated for all grid points.

Previous PIC applications in oceanography have used linear weighting functions and equally weighted the four corners of each cell which the particle overlies. Such weighting may produce a rough height field and thus smoothing must be introduced. Typically, the height field is smoothed at each time step. This explicit smoothing inherently introduces artificial damping into the calculation. However, as demonstrated in this study, the use of TSC weights and the consistency between interpolation and differentiation can eliminate the need for all explicit smoothing. Of course, there is some smoothing implicit in the interpolation.

3.5 Parallel Implementation

The models developed were coded to run on parallel computers with distributed memory architecture. This gives a computational advantage by distributing the computational workload and memory requirements amongst multiple processors. The PIC algorithm is ideally suited for parallelization.

The PIC algorithm can be parallelized in the following manner. Each processor is made responsible for only a subset of the particles while retaining a copy of the

entire grid. (In the two-layer model there is a grid for each layer.) Each processor interpolates the heights of its particles to its copy of the grid. When all processors have finished this operation, a gather–add–scatter command is issued for the grid data; this command directs each processor to communicate its designated data to a common processor which adds all of the incoming data and then communicates the result back to all processors. Each processor's grid then contains the sum of heights from all processors and thus the sum of the interpolated heights from all particles. After computing gradients on the grid, each processor interpolates those gradients back to its subset of particles and updates their position and velocity by integrating the equations of motion. This algorithm is shown in schematic form in figure 4. Generally, the number of particles per processor is much greater than the number of grid points, thus there is little advantage to parallelizing the grid operations, as was confirmed with experiments. This algorithm is nearly ideal, since communication between nodes is only necessary at one point in each iteration. Thus, time spent communicating information between nodes is minimal.

The above scheme has been implemented using the Message Passing Interface (MPI) on the IBM SP2 located at the Maui High Performance Computing Center (MHPCC). MPI is a library of routines designed to communicate information between nodes of a parallel computer. Unlike many message passing libraries, it is relatively easy to implement as well as being portable and efficient. Most libraries are either platform-specific and efficient or portable but highly inefficient. The SP2 at MHPCC consists of over 400 processing elements in parallel. Each element is an IBM RISC System/6000 (RS6000) with at least 128 MB of RAM. The processors are interconnected via a high performance switch fabric which provides a mechanism for internal message passing.

The models used in this study were run on between 1 and 32 nodes of the SP2. Speedup results of the parallelization will be discussed in section 4.4.

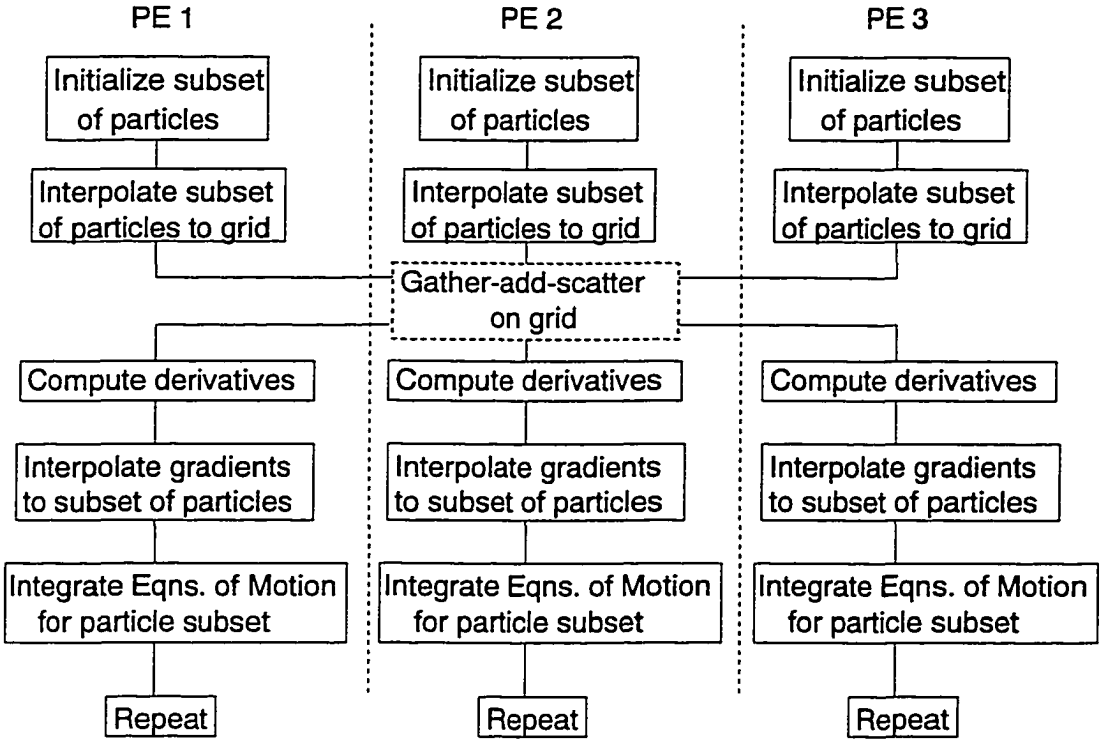

Figure 4: Flow diagram of the parallel PIC algorithm with three processing elements (PE1, PE2, and PE3).

3.6 Boundary Conditions

In the reduced gravity model the lower layer is considered to be infinite in horizontal extent, thus there are no lateral boundaries to consider. However, the domain of the two-layer model is finite so the issue of lateral boundary conditions must be addressed. Periodic boundary conditions are not appropriate since gravity waves will quickly traverse the model domain; their re-entrance at the opposite side of the model would be unrealistic and undesirable. As no information is known beyond the domain of the model, open boundary conditions (OBCs) are the most appropriate. Chapman [1985] provides an excellent review and evaluation of several numerical formulations of OBCs.

Experimentation with several forms of OBCs found methods using a "sponge layer" most appropriate for the PIC model. The sponge layer consists of a region around the model domain in which bottom friction is increased. This acts to damp

wave motion so that little energy exists at the domain boundaries. Several parameters determine the characteristics of the sponge. These include the size of the sponge (i.e., the number of grid points), the maximum and minimum friction in the sponge, and the equation determining the friction as a function of position. With the friction increasing linearly in the sponge layer, the friction is determined by,

$$r = (r_M - r_m)(x_{iB} \pm x_i)/ns \tag{40}$$

where r_M, r_m are the maximum and minimum friction, respectively, ns is the number of grid points in the sponge, x_i refers to the coordinate in the i direction, where $i = 1, 2$, and x_{iB} is the boundary point in that direction. The upper (lower) sign in (40) refers to the right (left) boundary.

The damping in the sponge layer is physically unrealistic; it is simply a computational convenience to avoid energy reflection at the model domain boundaries. Therefore, the solution in the sponge layer is unrealistic and not of interest. Thus, although it may be desirable to make the sponge quite large for better absorption characteristics, it is not practical to dedicate a large portion of the domain to the sponge layer. The friction in the sponge must also be determined carefully. If it is too large or increased too suddenly, wave energy may be reflected from the sponge. If the friction is too small or the sponge too narrow, energy may not be damped adequately before reaching the boundary. Experimentation with the PIC model indicated that a sponge layer 16 grid points wide with a maximum friction of 0.25 was adequate. Thus, the sponge width was one-eighth the width of the model domain (128 grid points). Being on all four lateral boundaries, this equates to approximately 44 percent of the total area of the model domain.

Other implementations of OBCs may be used in conjunction with or instead of sponge layers. Most of these formulations are based on the Sommerfeld radiation condition, which in one-dimension is given by,

$$\phi_t \pm c\phi_x = 0 \tag{41}$$

where ϕ is a dynamical variable in the model, c is the phase speed of wave propagation, and the subscripts t and x denote partial differentiation with respect to time and space, respectively. The upper (lower) sign in (41) corresponds to the right (left) boundary.

The various formulations of the Sommerfeld radiation condition discussed in Chapman [1985] mostly differ in the calculation of the phase speed, c. This calculation and the details of its finite difference implementation can significantly alter the characteristics of the OBCs. The range of success varies from highly reflective conditions to some that radiate energy quite effectively.

Implementing these radiation conditions with the PIC model is difficult. These conditions require height (or pressure) and velocity data to be known on a standard finite difference grid. However, with the hybrid nature of the PIC model only height is known on a regular grid while velocity is known at the particle positions. Because of this difficulty, these radiation conditions were not used in the two-layer PIC model.

4 RESULTS

4.1 Reduced Gravity Model

The reduced gravity model was tested against numerical solutions to the lens equations. The results are detailed in Kirwan et al. [1997] and are reviewed here for completeness and for purposes of model validation.

The PIC model was tested with two cases. The PIC model and lens equation solution were initialized identically. In both tests the lens was initially circular with a parabolic depth profile. In the first test, the "pulson" case, the velocity field contained only divergence and vorticity. The solution is expected to remain circular and pulsate between shallow and deep modes. The pulson solution is an analytical solution to the lens equations; for details of the solution, see Kirwan and Liu [1991]. In the second test, the "deformation" case, deformation (normal and shear) was added to the velocity field of the lens. In this case, the solution is expected to be that of an elliptical eddy which rotates anticyclonically and pulsates.

Figure 5 shows the time series of the centerline height (i.e., the height at the geometric center of the eddy) of the PIC and lens solutions for the pulson case. The PIC model result is the solid line and the analytical lens solution is the dashed line. The lens oscillates at the inertial frequency between a broad, shallow mode and a deep, narrow one. The lens remains circular and pulsates between these two modes. Clearly, the PIC model does a very good job of reproducing the lens solution. There is only a slight difference in the amplitude of the peaks of the solution and the phase agrees almost exactly. Power spectra of the two time series are nearly identical and indicate that approximately 98% of the energy is at the inertial frequency. The two signals have a cross-correlation coefficient of 0.9985 at zero lag. The energy invariant from a 30-day simulation is shown in figure 6. The solid line is the potential energy, the dashed line is the kinetic energy, and the dashed-dotted line is the total energy.

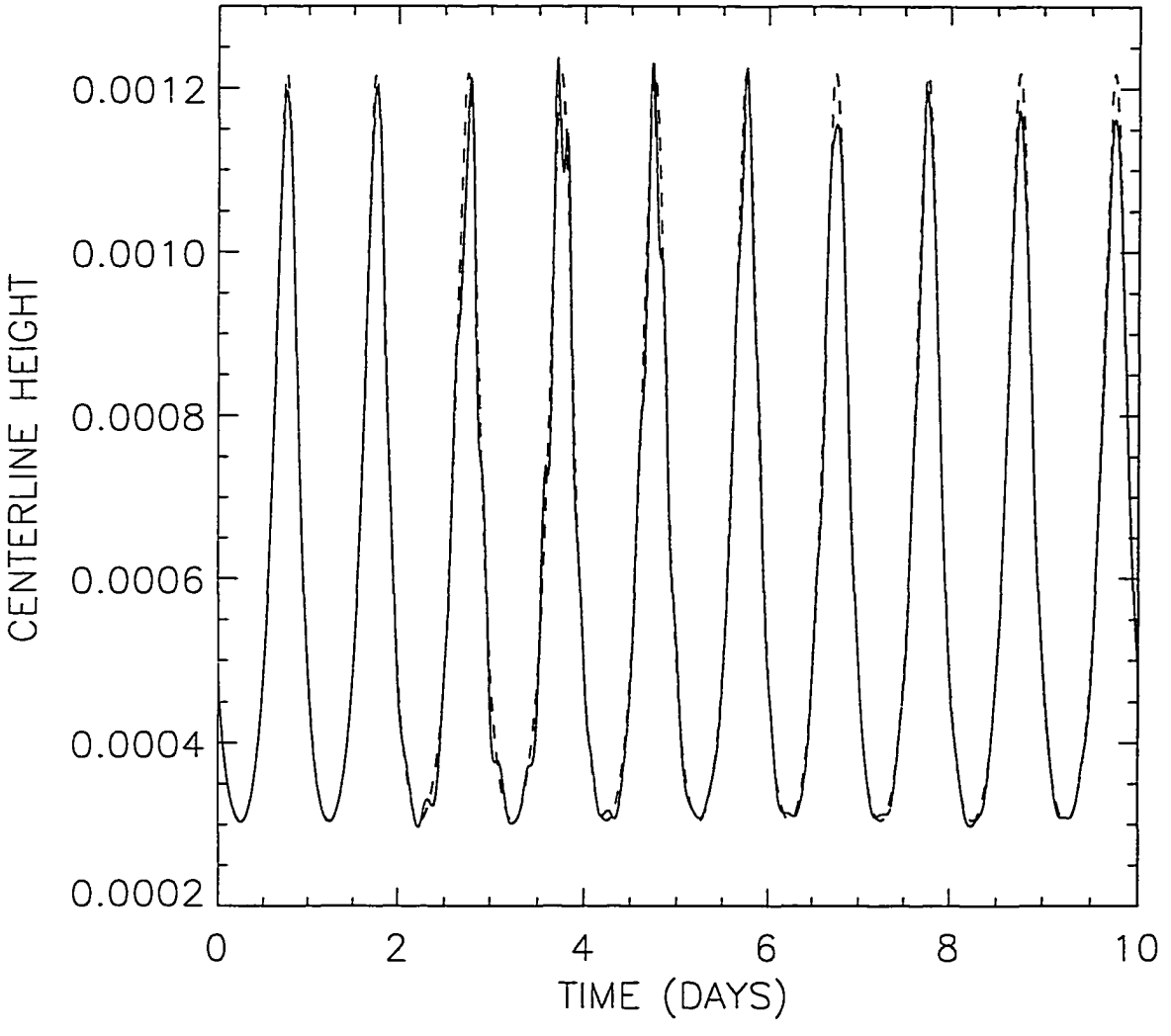

Figure 5: Time series of the centerline height of the eddy in the pulson case. The solid line is the PIC model solution and the dashed line is the lens solution.

Here, the lens can be seen to be exchanging potential and kinetic energy as it oscillates between the shallow and deep modes. The total energy is conserved to within 2% over the 30-day simulation.

The time series of the centerline height for the deformation case is shown in figure 7. The inertial oscillation is apparent as is a low-frequency modulation. Overall, the PIC model satisfactorily reproduced the low-frequency signal. Again, there is a slight discrepancy in the amplitude of the peaks, but the phase in the two solutions agree very well. As in the previous case, power spectra of the two signals are essentially identical and 98% of the energy is in the inertial signal. The two time series have a cross-correlation coefficient of 0.9958 at zero lag. As shown in Kirwan et al. [1997] contours of the boundary of the lens from the lens equation solution and the PIC model agree favorably. The two solutions agree very well to about day 5.0. Thereafter, there is a slight discrepancy in the phase of rotation. The energy invariant from a 30-day simulation is shown in figure 8. In addition to the inertial pulsation, the low-frequency modulation is apparent. The total energy is conserved within 2% throughout the 30-day simulation.

The differences between the lens solution and PIC model solutions are expected since the physics of the two approaches are not the same. The lens solution restricts the geometry and form of the velocity fields for all time, whereas the PIC model is completely general. The two approaches share only the same initialization. Thereafter, the PIC solution may take any form, whereas solution to the lens equations is constrained to have a parabolic shape and linear velocity profile for all time. The differences in the amplitude of the peaks of the signal in figures 5 and 7 were investigated by examining profiles of the eddy at times coincident with the peaks in the amplitude. This analysis indicates that the PIC-modeled eddy is slightly broader, and thus shallower, then the lens equation solution at these times. Some of this broadening may be attributed to the fact that, as described in section

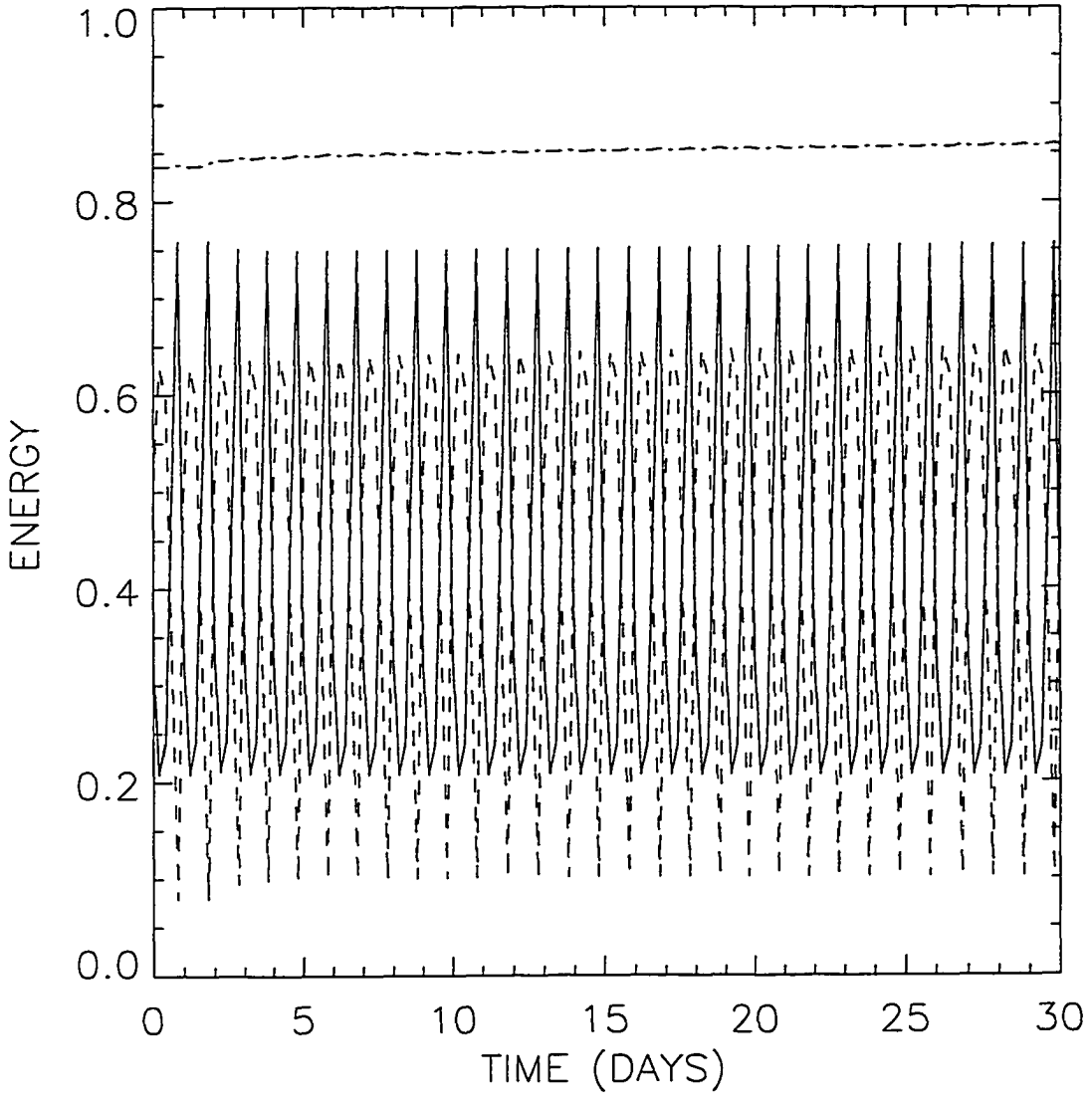

Figure 6: Time series of the energy invariant over a 30-day simulation of the pulson case. The solid line is the potential energy, the dashed line is kinetic energy, and the dash-dotted line is the total energy.

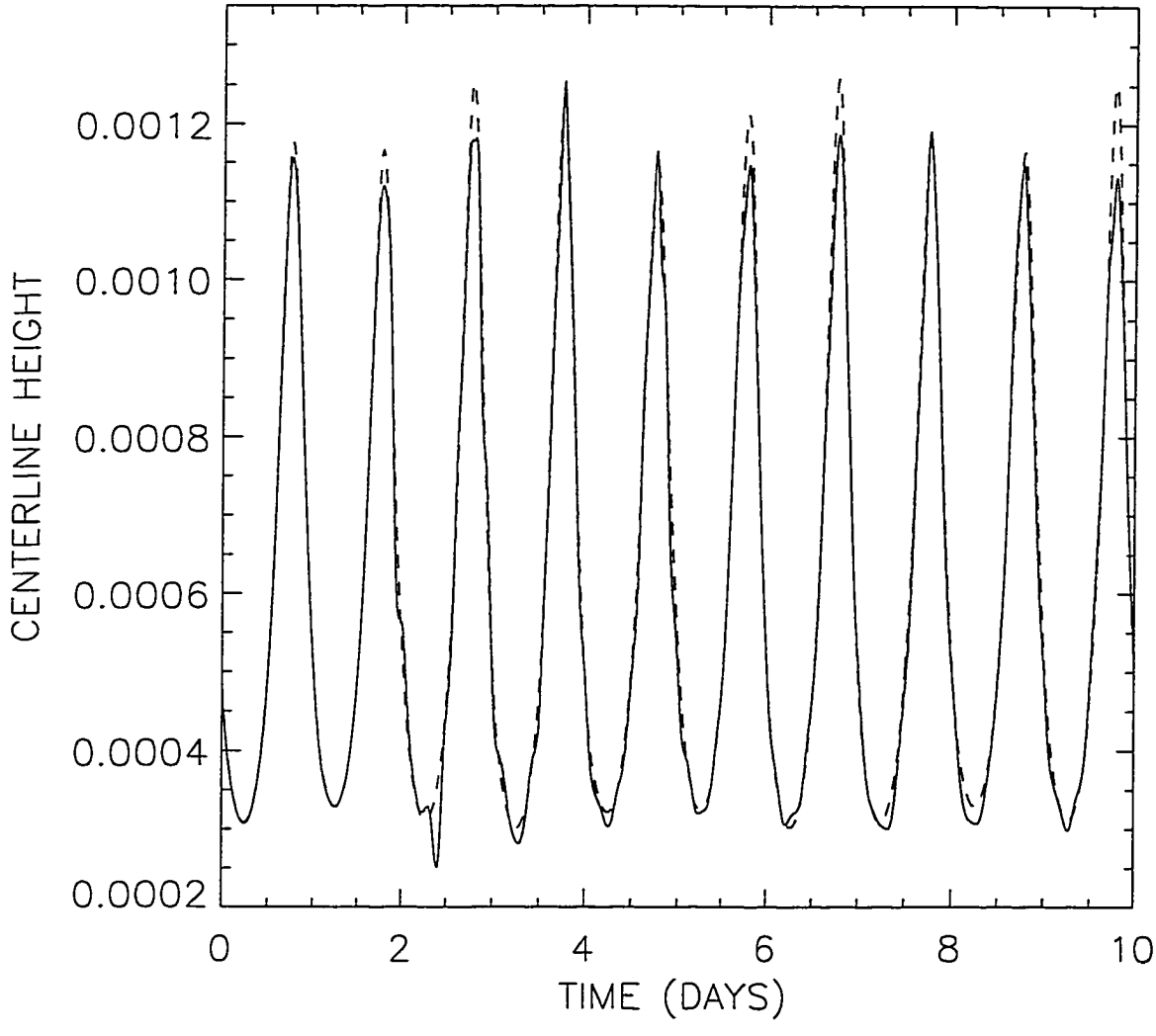

Figure 7: Time series of the centerline height of the eddy in the deformation case. The solid line is the PIC model solution and the dashed line is the lens solution.

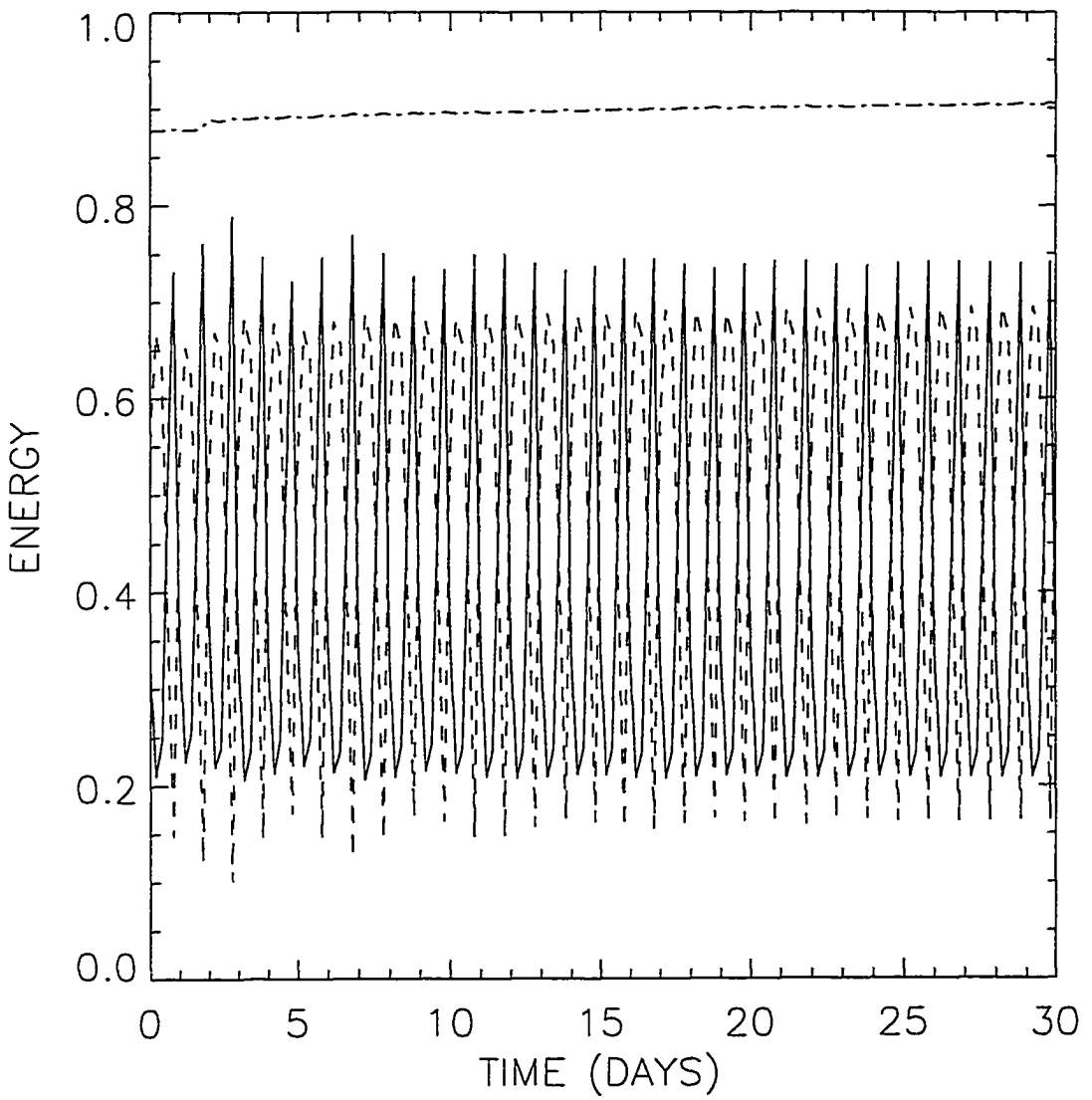

Figure 8: Time series of the energy invariant over a 30-day simulation of the deformation case. The solid line is the potential energy, the dashed line is kinetic energy, and the dash-dotted line is the total energy.

3.4, a particle's height is interpolated to the nine grid points nearest its center.

The conservation of the energy invariant by this PIC model is encouraging. In contrast, Pavia and Cushman-Roisin [1988] reported an 11% increase in an energy invariant over a 15-day simulation with their PIC model. Presumably, their inability to conserve invariants better than this was due to inconsistencies between their interpolation and finite difference operations. They used a first-order interpolation scheme with a second-order spatial difference scheme. As mentioned in section 3.4, this will cause fictitious pressure forces at the particles. The smoothing that they necessarily introduced into the calculation also contributed to the non-conservation of the invariants.

It is understood that some characteristics of the solutions presented above are probably not representative of real oceanic lenses. For instance, the four-fold oscillation in amplitude of the lens thickness, depicted in figures 5 and 7, is much greater than what is expected in nature. Presumably viscosity, which is not included in this formulation of the model, suppresses these oscillations. Nevertheless, these experiments serve as a severe test of the PIC model. Previously, the only reported test of an oceanographic PIC model was of its ability to reproduce and maintain a steady-state solution [Pavia and Cushman-Roisin, 1988]. The success of the model in reproducing the pulson and deformation solutions show that the PIC method is capable of resolving scales of motion not achievable with other techniques.

4.2 1.5-layer Model

This section addresses effects of environmental forcing on a lens by using the 1.5-layer model described in section 3.1.2. The model with prescribed lower layer flow was used to determine how vorticity, divergence, and deformation in the velocity field of the exterior layer affect the evolution and characteristics of a warm-core ring.

Very little work has been done to study environmental forcing on a lens; most studies consider only an isolated lens. Nof [1985] found two analytical configurations for a lens embedded in a simple strain flow. Each solution consisted of steady elliptical eddy of which the orientation depended on the sense of the strain flow. Ruddick [1987] made an analytical study of anticyclonic lenses in strain and shear flows. His study focused on applications to lenses of Mediterranean water, or "Meddies", trapped between two fluid layers. He solved the lens equations with simple forcing in the upper and lower layers and found steady solutions which consisted of an elliptical eddy aligned 45° from the principal axis of the forcing velocity field. The ellipticity of the lens was determined to increase with forcing magnitude, and a limit to the forcing magnitude above which no physical solutions exist was determined. The study concentrated on steady solutions and could only speculate on the evolution of non-steady solutions. Brickman and Ruddick [1990] extended the work of Ruddick [1987] and studied the stability of elliptical lenses in strain and shear fields. They found two steady-state solutions and one unstable configuration, referred to as a "raingutter" or "infinite channel" solution. A stability limit was determined as a function of exterior forcing, lens Rossby number, and ellipticity. As in Ruddick [1987], this paper made use of the lens solution, which restricted the geometry and height and velocity structures. The limit between stable and unstable regimes was consistent with the work of Ruddick [1987], but again only speculation was made on time-dependent solutions or those with more complex geometries, such as filamentation or shedding of satellite eddies. Brickman and Ruddick [1990] also undertook a laboratory study which agreed well with the analytical result. With this agreement, they suggested that the lens solution was a reasonable approximation to nature. In particular, they noted that the assumption of the decoupling of the layers in the 1.5-layer model was reasonably accurate. Kirwan et al. [1992] studied the effects of environmental deformation on the evolution of negative potential

vorticity lenses. They found three types of solutions to the lens equations. The first was an oscillatory type, and the other two types were equilibrium solutions. One of these was similar to the raingutter solution. The other was an infinitely thin, circular eddy, which they termed a "pancake" solution.

These studies shed light on the stability of elliptical lenses in the presence of a simple exterior forcing. They suffered from the consequences of using the lens equations and its consequent restrictive solution form. In addition, the exterior forcing was quite simple and only considered shear. Furthermore, these studies focused on steady-state solutions.

Many of these short-comings are eliminated by the 1.5-layer PIC model. The initial lens was circular in plan form with a parabolic depth profile and linear velocity profile. However, with the use of the PIC model there was no restriction on the evolution of the shape, depth or velocity profile. In fact, although not reported here, the PIC model could be initialized in essentially any form.

In the experiments described below, the lens was chosen to be initially circular and in geostrophic balance. This choice was considered appropriate since observations suggest that warm-core rings exist mostly in nearly circular shapes and in near geostrophic balance [e.g., Kennelly, 1985]. The vorticity of the lens was taken as $G_R = -.25$, which is within the range of $-.28 - -.17$ measured by Joyce and Kennelly [1985] from observations of WCR 82-B. The exterior forcing velocity field is completely general and can include normal and shear deformation, vorticity, and divergence.

A parameter study was undertaken in which G_N, G_S, G_R, and G, the normal and shear deformational, rotational, and divergent components of the exterior velocity, respectively (see equations (11) and (12)), were varied. Figure 9 shows velocity vectors of the forcing fields for each of the components. For clarity only the central portion of the domain is shown. Notice that the deformational forcing components,

G_N and G_S, produce saddle points at the origin. With normal deformation, the inflow and outflow axis are aligned with the x and y axes. Positive values of G_N correspond to inflow along the y-axis and outflow along the x-axis, while negative values indicate the opposite. Shear deformational forcing also corresponds to a saddle point at the origin, however the inflow and outflow axes are rotated 45° so that positive values indicate inflow along the $\Theta = -45°$ axis and outflow along $\Theta = 45°$ (Θ as measured from the x-axis). These two components of deformation differ in their orientation with respect to the Coriolis acceleration. The rotational component, G_R, corresponds to rotation about the origin. Positive values indicate cyclonic motion and negative values indicate anticyclonic motion. The divergent component, G, indicates divergent flow, outward from the origin, for positive values and convergent flow for negative values. Also note that for all components the magnitude of the velocity increases linearly with radius.

These velocity components derive from a decomposition of the velocity field, G_{ij} (**G**) which is presented in appendix B. Furthermore, they obey certain rotational transformations (also presented in appendix B). The divergent, G, and rotational, G_R, components are invariant under a rotation normal to the plane. The normal and shear deformation components exhibit symmetry characteristics. Thus, the experiments below focus on points in only one quadrant of the G_N, G_S plane. Points in other quadrants can be determined from the symmetry relationships presented in appendix B.

In the first set of experiments the rotational and divergent components of the exterior flow were taken to be zero ($G_R = G = 0.0$) and a matrix of values of normal and shear deformation, G_N and G_S, were chosen. Three solutions regimes were found. The first consists of an anticyclonically rotating ellipsoid. In the second regime, an elliptical eddy forms which then sheds satellite eddies or filaments, leaving a smaller eddy which then rotates as in the first regime. This regime does not exist in

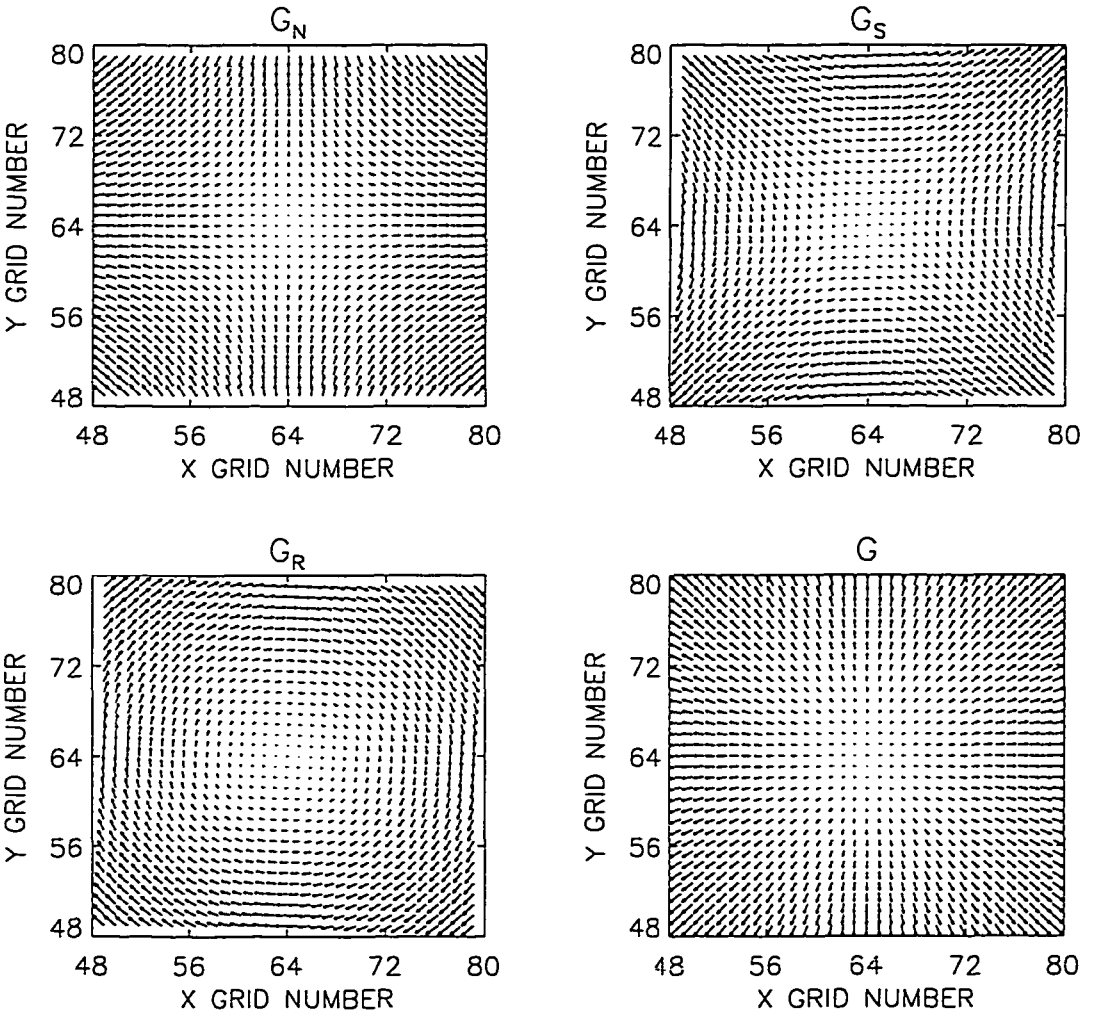

Figure 9: Forcing flow field for each of the components G_N, G_S, G_R and G, normal and shear deformation, rotation, and divergence, respectively. For clarity only the central portion of the grid is shown.

the lens equation solutions. The third regime is the so-called "raingutter" solution in which the eddy is stretched into an elongated filament. These three regimes will be referenced respectively as regimes I, II, and III. Figure 10 is a diagram of the parameter matrix in the G_N, G_S plane. Each symbol plotted represents a model run with the corresponding forcing parameters and indicates which solution type resulted. Regimes I, II, and III are indicated by diamonds, triangles, and crossed-squares, respectively. Notice that regime I predominates at lower levels of deformation. Regime II results from slightly higher magnitudes of forcing, and regime III results from the most severe forcing.

It is interesting to compare the results here to those of Ruddick [1987]. For the given rotation rate of the lens ($G_R = -0.25$), Ruddick [1987] (from his fig. 5) predicts a maximum rate of strain to be approximately $0.020f$, where f is the Coriolis parameter. Although it should be noted that regime II can not be represented in the formulation used by Ruddick, this result agrees quite well with those presented in figure 10, which shows the stability limit to be between $0.015f$ and $0.020f$. Also of note is a relationship between the forcing magnitude and the rotation rate of the eddies in regime I. This will be discussed after and in conjunction with the next set of experiments.

Figure 11 shows an example in which the forcing on the lens produced a rotating ellipsoid. This solution type is designated as regime I. In this example, $G_N = 0.005, G_S = 0.0075$, and $G_R = G = 0.0$. In this simulation the initially circular lens deforms into an ellipse and rotates anticyclonically at rates between 3° and 6° per day. Furthermore, a pulsation mode is apparent, as the lens oscillates between a shallow, broad mode and a deep, narrow one. This is depicted in figure 12, which is a time series of the centerline height of the lens. The pulsation is at the inertial frequency and the amplitude is approximately ± 25% of the average height. Spectral analysis of the time series of the centerline height indicates that approximately 95.8%

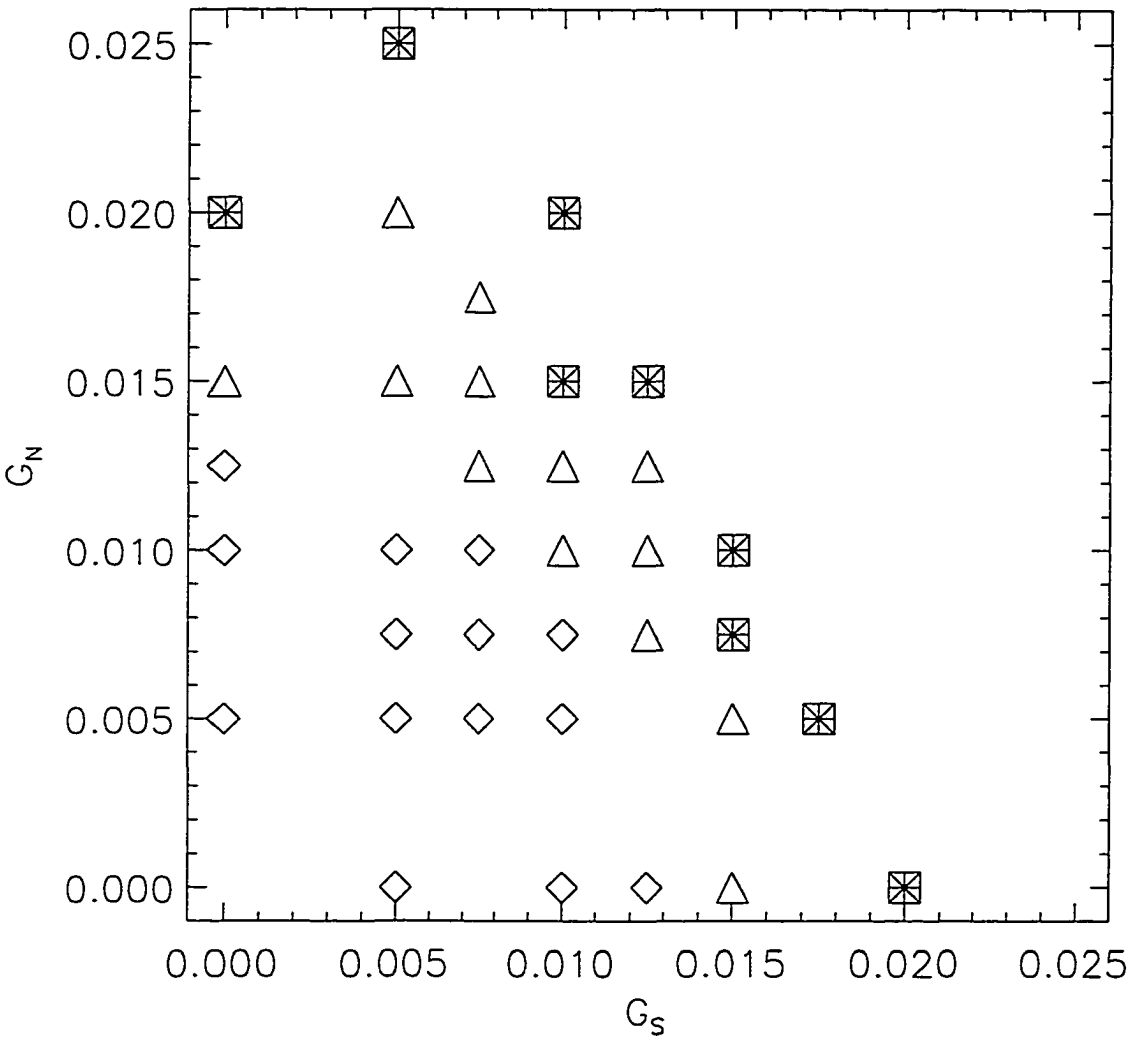

Figure 10: Stability diagram for the experiments with no vorticity ($G_R = 0.0$). Solutions in regimes I, II, and III are indicated by diamonds, triangles, and crossed-squares, respectively.

of the energy is at the inertial frequency. There is no indication of an instability in this simulation.

This solution mode of a rotating elliptical eddy is unlike that which Ruddick [1987] speculated as the fate of a circular eddy subjected to shear flow. He suggested that the lens would elongate and rotate to a steady-state position in which the major axis of the lens was oriented along the outflow axis of the forcing field. In hindsight, his speculation seems unlikely since the lens would have rotational inertia as it approached the steady-state position. The rotating mode found in the PIC simulation may be a consequence of the lens approaching and over-shooting the steady-state configuration, then readjusting, rotating towards an equilibrium configuration, and repeating the process.

An example of regime II, in which the eddy sheds satellite vortices is shown in figure 13, which shows contours of the lens boundary at 2.5 day intervals. Here the exterior velocity field was specified with $G_N = G_S = 0.01$ and $G_R = G = 0.0$. In this case, the eddy deforms into an ellipse and begins to rotate anticyclonically. However, when the major axis of the ellipse is aligned along the x-axis, the ellipse stalls and begins to elongate. Apparently, the magnitude of the normal deformation is great enough to cause this elongation. Recall from figure 9 that a positive value of G_N corresponds to flow towards the origin along the y-axis and outward from the origin along the x-axis. This is consistent with the stretching in this case. By day 20, the lens is elongated to an eccentricity of 0.98. This is well beyond the eccentricity limit of 0.84 for stability found by Cushman-Roisin [1986b] in a linear stability analysis of large, elliptical rings. By day 25 the ends of the ellipse begin to show signs of pinching off. At day 30, these ends have shed in the form of two satellite vortices, leaving an elliptical lens in the central region. To further explore the shedding event and the fate of the resulting configuration, this same case was run on a larger domain for a 50-day simulation. The boundary of the lenses from days

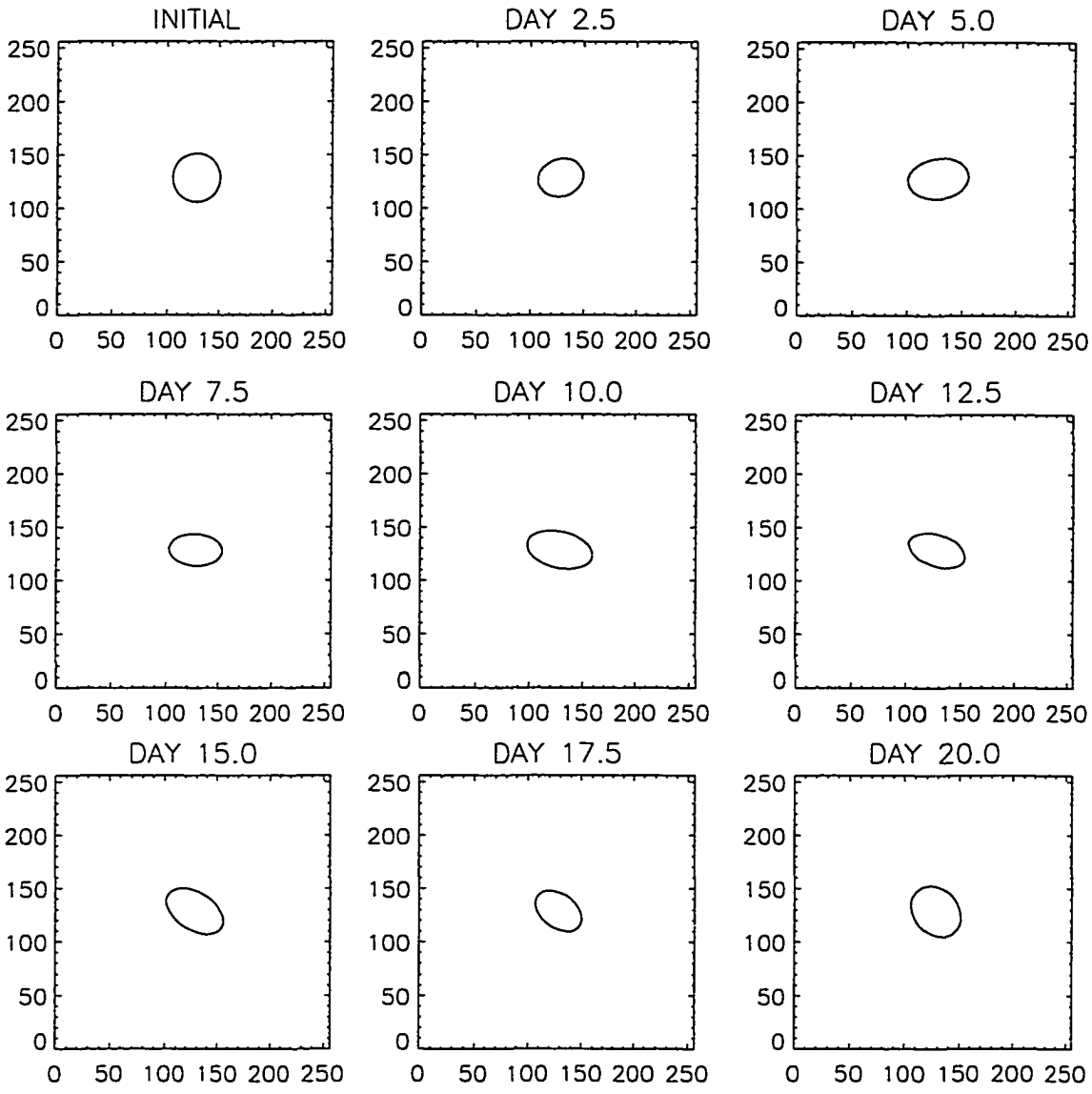

Figure 11: Evolution of the boundary of a lens in solution regime I. Here, $G_N = 0.0075, G_S = 0.005$, and $G_R = G = 0.0$. The axes labels are the grid points in each direction.

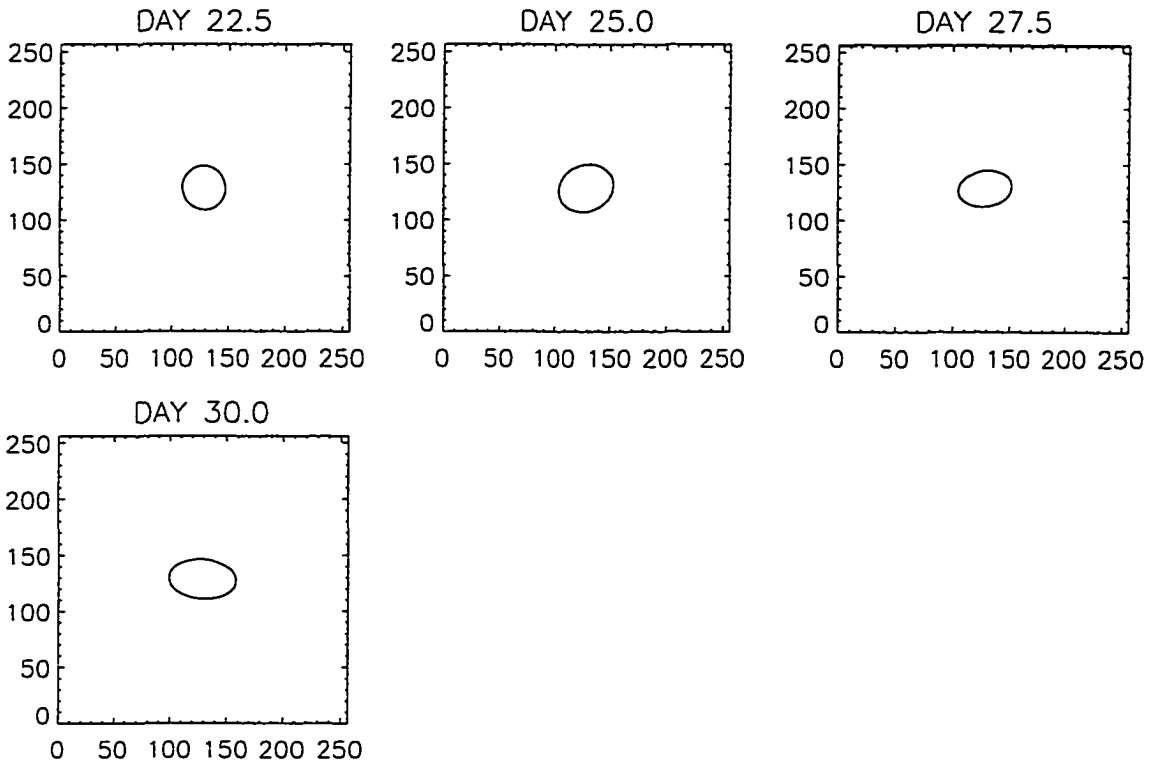

Figure 11: Continued.

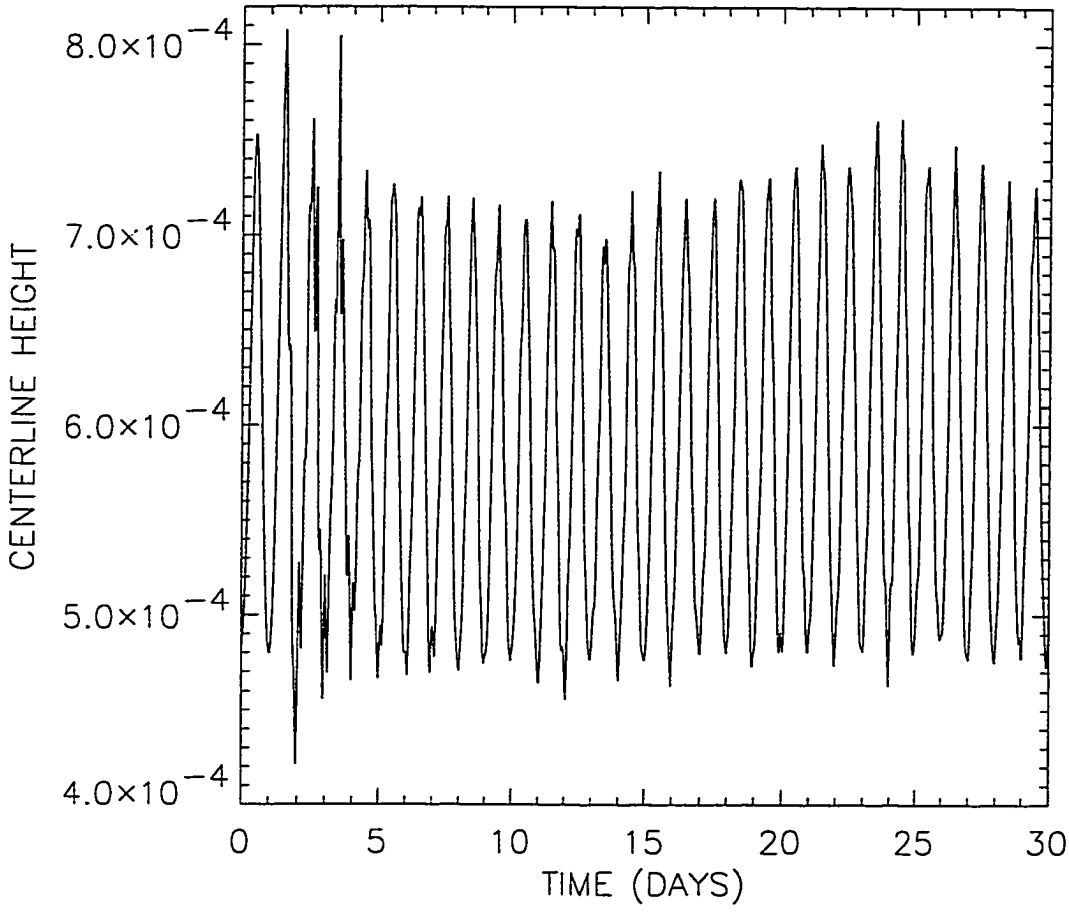

Figure 12: Time series of the centerline depth of the eddy depicted in figure 11.

30 to 50 is shown in figure 14. After the satellite eddies are shed, they are advected away from the lens along the axis of the outflow and eventually out of the model domain. The central lens remains elliptical and rotates anticyclonically at rates varying from 10° to 20° per day and shows no signs of splitting again throughout the remainder of the 50 day simulation. The two shed eddies have a maximum depth roughly equivalent to that of the main lens at the time of splitting and each contains approximately 32% of the total volume of the initial lens. The central eddy is accordingly reduced in size. As noted above, the magnitude of the forcing velocity field increases linearly with radius. Thus, this smaller eddy will experience less severe forcing than initially and is unlikely to undergo another shedding event.

The shedding event is also readily apparent in the time series of the centerline height, shown in figure 15. The lens pulsates at the inertial frequency as in the previous case. However, there is a steady decrease in the centerline height with time as the lens stretches along the x-axis. By day 25, the average centerline height is roughly 61% of that of the initial oscillation. Shortly afterwards, the shedding event is complete, and the lens then oscillates about a lower average depth for the remainder of the simulation. A low frequency modulation is apparent, as well as the inertial signal. Analysis of the autocorrelation function and power spectrum of the time series of centerline height indicates that the signal is dominated by the low frequency of the shedding event; 82% of the energy is in a broad peak at the lowest resolved frequencies. The remainder of the energy is at the inertial frequency.

This simulation presents an intriguing result in which the forcing caused the initially circular lens to deform into an ellipse and then bifurcate by shedding two vortices. After shedding the eddies, the lens remained elliptical and rotated anticyclonically. There were no signs of the process repeating throughout the remainder of a 50 day simulation. This process is consistent with the speculation in Ruddick [1987] that after shedding eddies, a lens would assume a more stable configura-

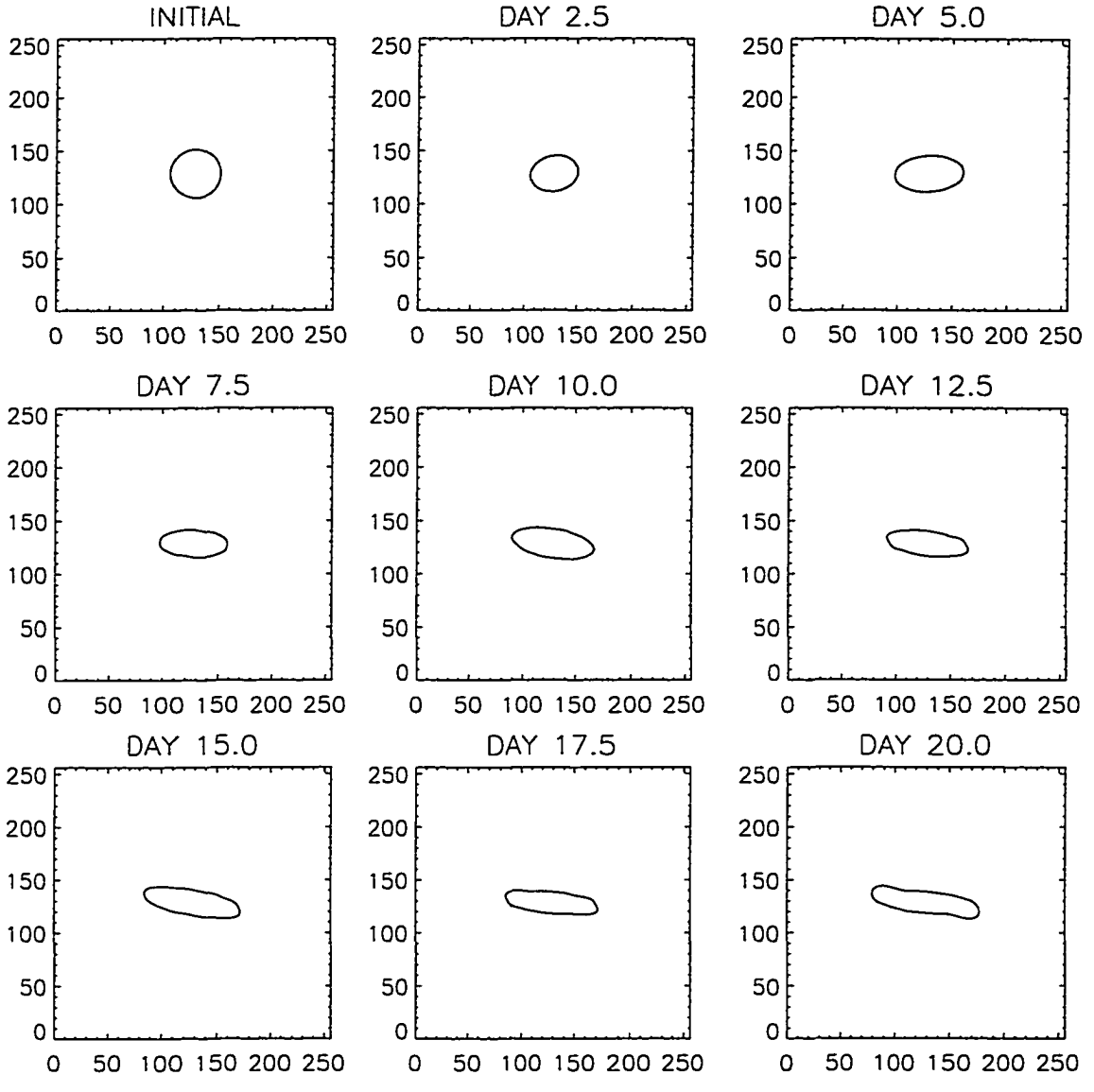

Figure 13: Evolution of the boundary of a lens in regime II. Here, $G_N = G_S = 0.01$ and $G_R = G = 0.0$. The axes labels are the grid points in each direction.

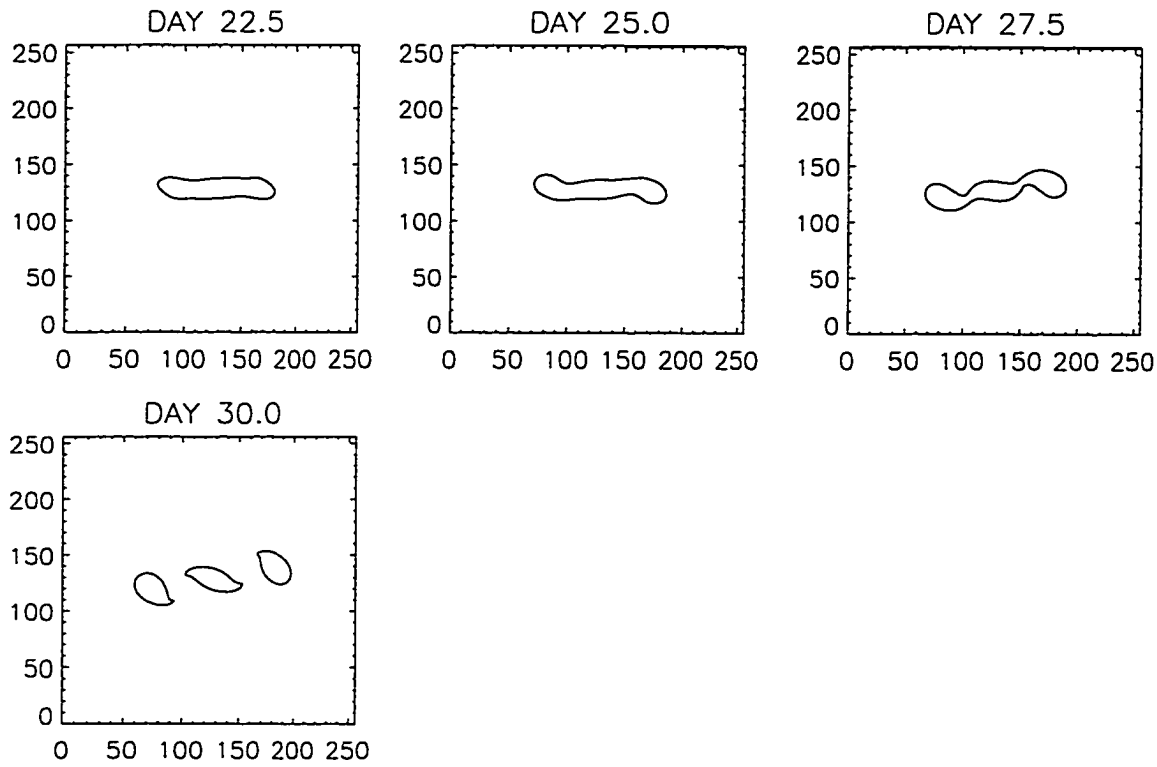

Figure 13: Continued.

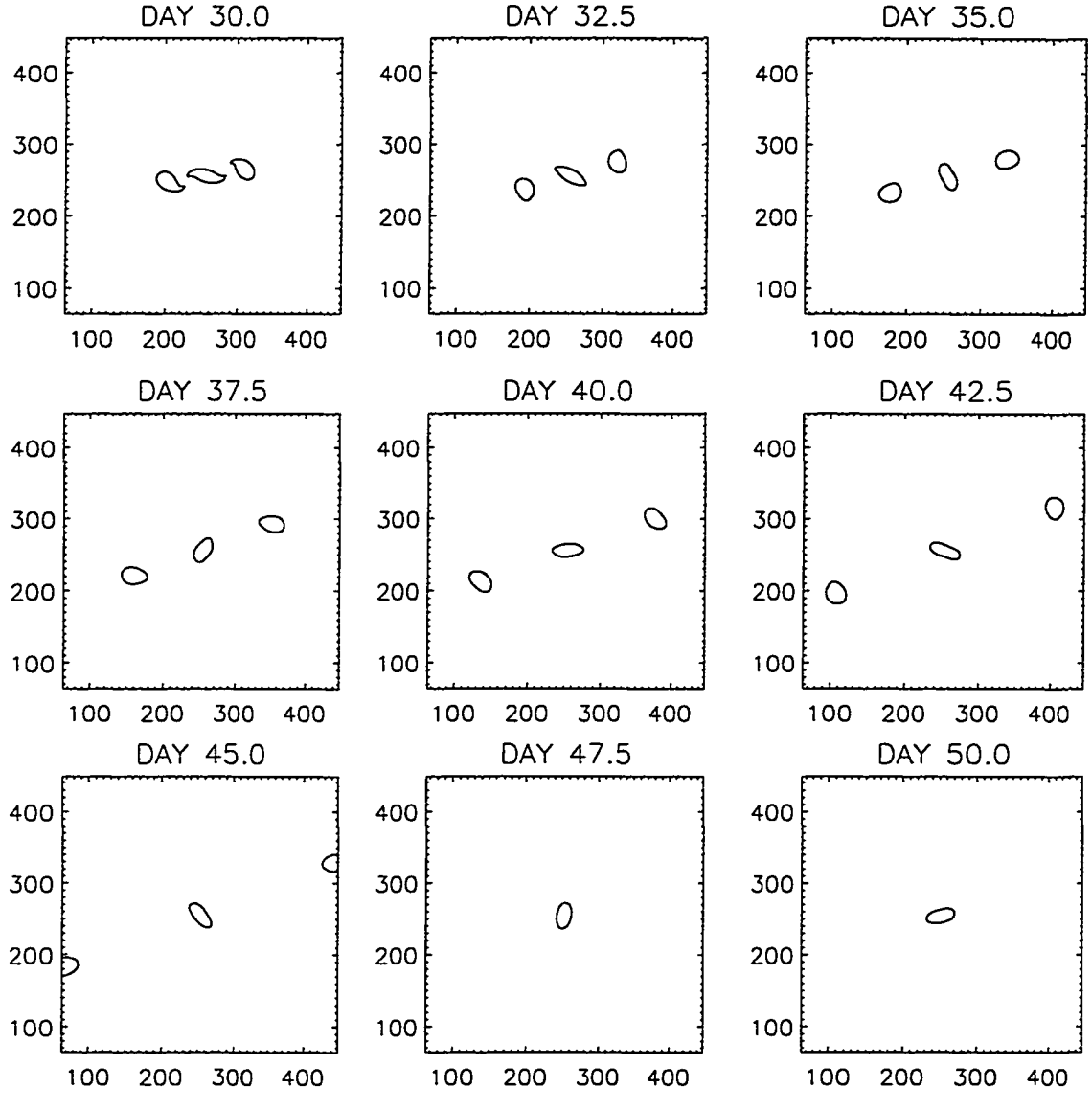

Figure 14: Continuation of the simulation shown in figure 13 but run on a larger domain for a length of 50 days.

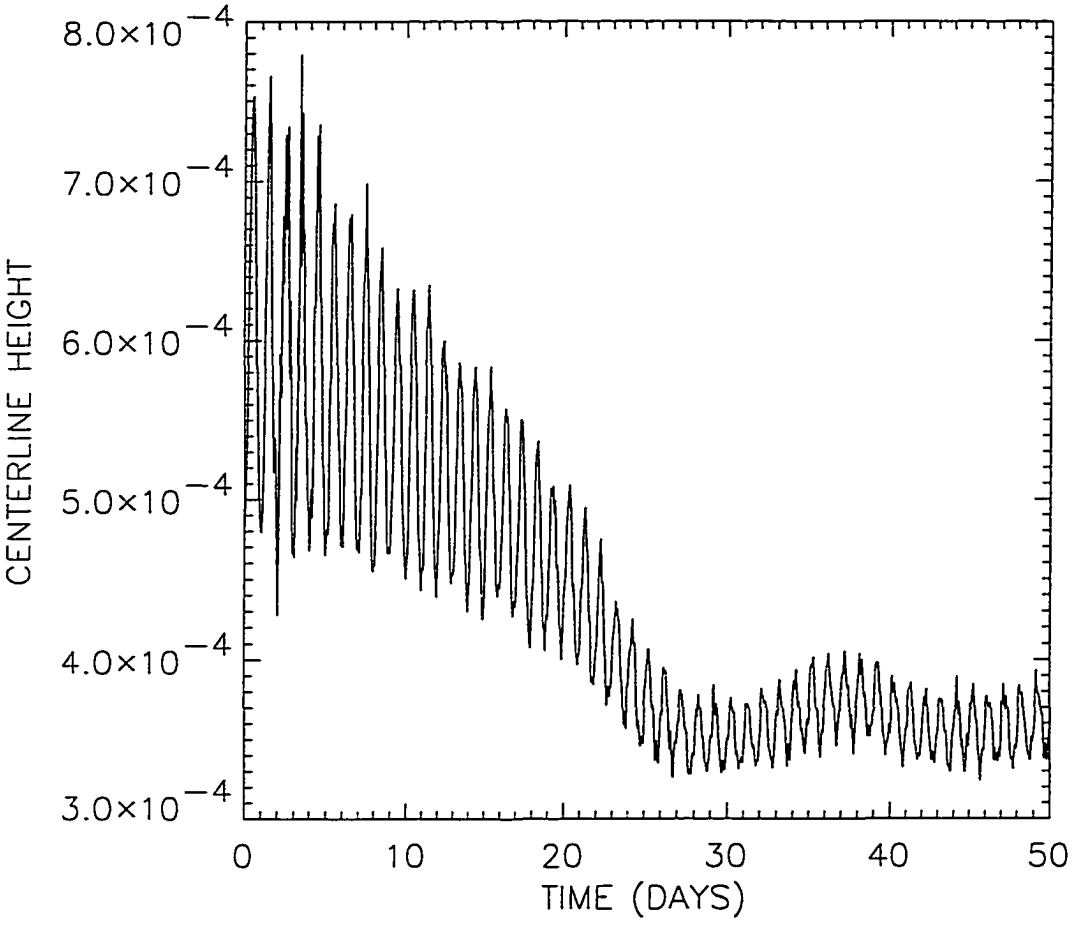

Figure 15: Time series of the centerline depth of the eddy in figures 13 and 14.

tion and continue to rotate without further shedding. In addition, Cushman-Roisin [1986b] speculated that rings which become highly eccentric might assume a more stable configuration by splitting into several smaller, more circular rings.

It is interesting to compare the solution with the PIC model to that of the lens equations with the same forcing. As noted above, the lens equation solutions are incapable of representing the lens as anything other than a rotating ellipsoid. Figure 16 shows the lens equation model solution for the centerline height, h_0, with forcing as $G_N = G_S = 0.01$ and $G_R = G = 0.0$. For the first 20 days of the simulation the solution is very similar to that of the PIC model. However, in the lens equation model solution the height continues to decrease with time. By the end of the 50 day simulation, the height predicted by the lens solution is only 30% of that predicted by the PIC model and is continuing to decrease. The lens solution can not reproduce the shedding event which moves the solution to a new state in the PIC simulation. Another interesting feature to note is that a super-inertial frequency develops in the lens solution at about 30 days, which coincides with the time of the shedding event in the PIC model. By the end of the simulation there are two oscillations per day in the centerline height. The difference between the two solutions is also evident in time series plots of the major and minor axes of the lens and the ratio of the two, as shown in figure 17. In the lens solution, the major axis increases greatly with time (to 26 times the initial value) while the minor axis decreases with time (to about one-sixth of the initial value). The ratio of the major to minor axis is on the order of 150 by the end of the simulation which indicates that the lens has stretched into a long, thin filament. This is unlike the PIC simulation, which produced a rotating ellipsoid after the shedding of the two smaller vortices. At the end of the PIC simulation, the ratio of the major to minor axes of the central eddy is only 1.59.

This comparison demonstrates the utility of the PIC model. Since the lens

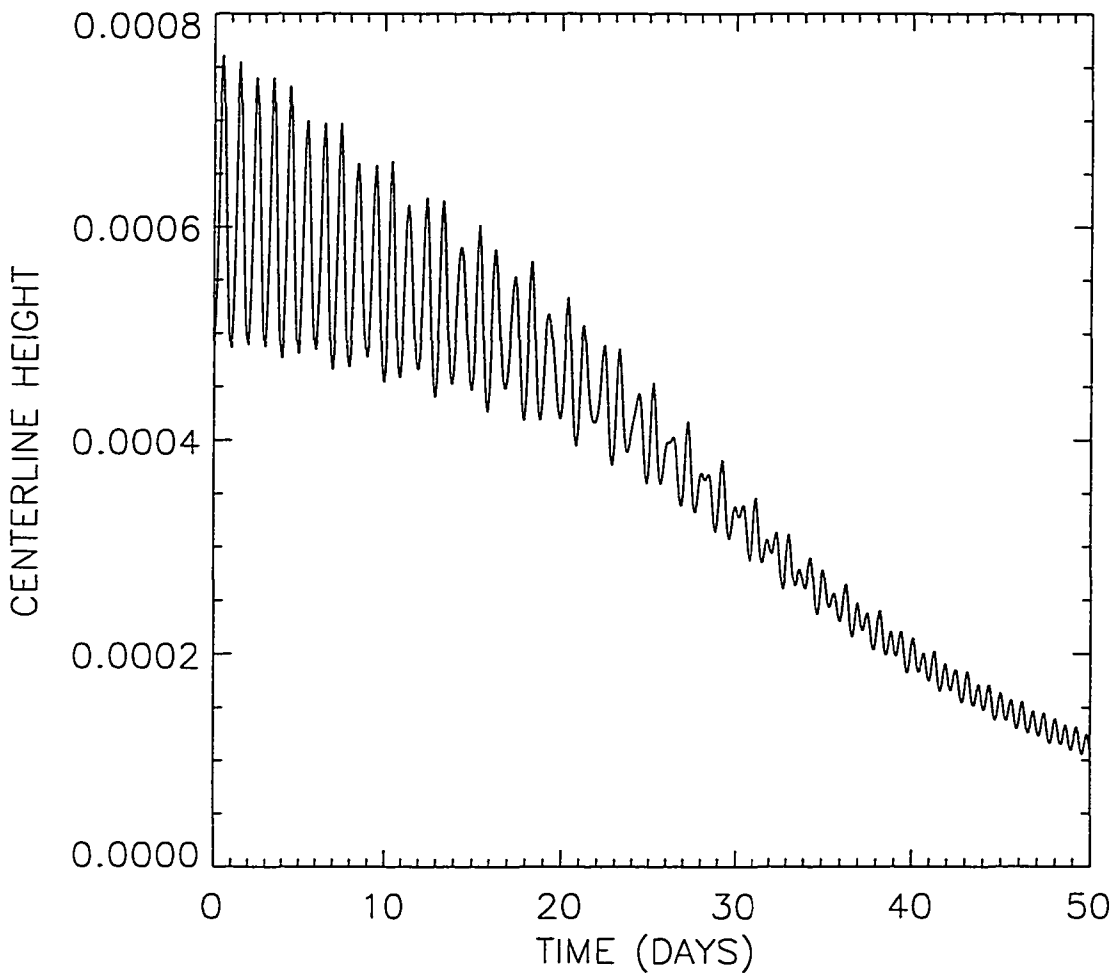

Figure 16: Time series of the centerline depth from the lens solution with $G_N = G_S = 0.01$.

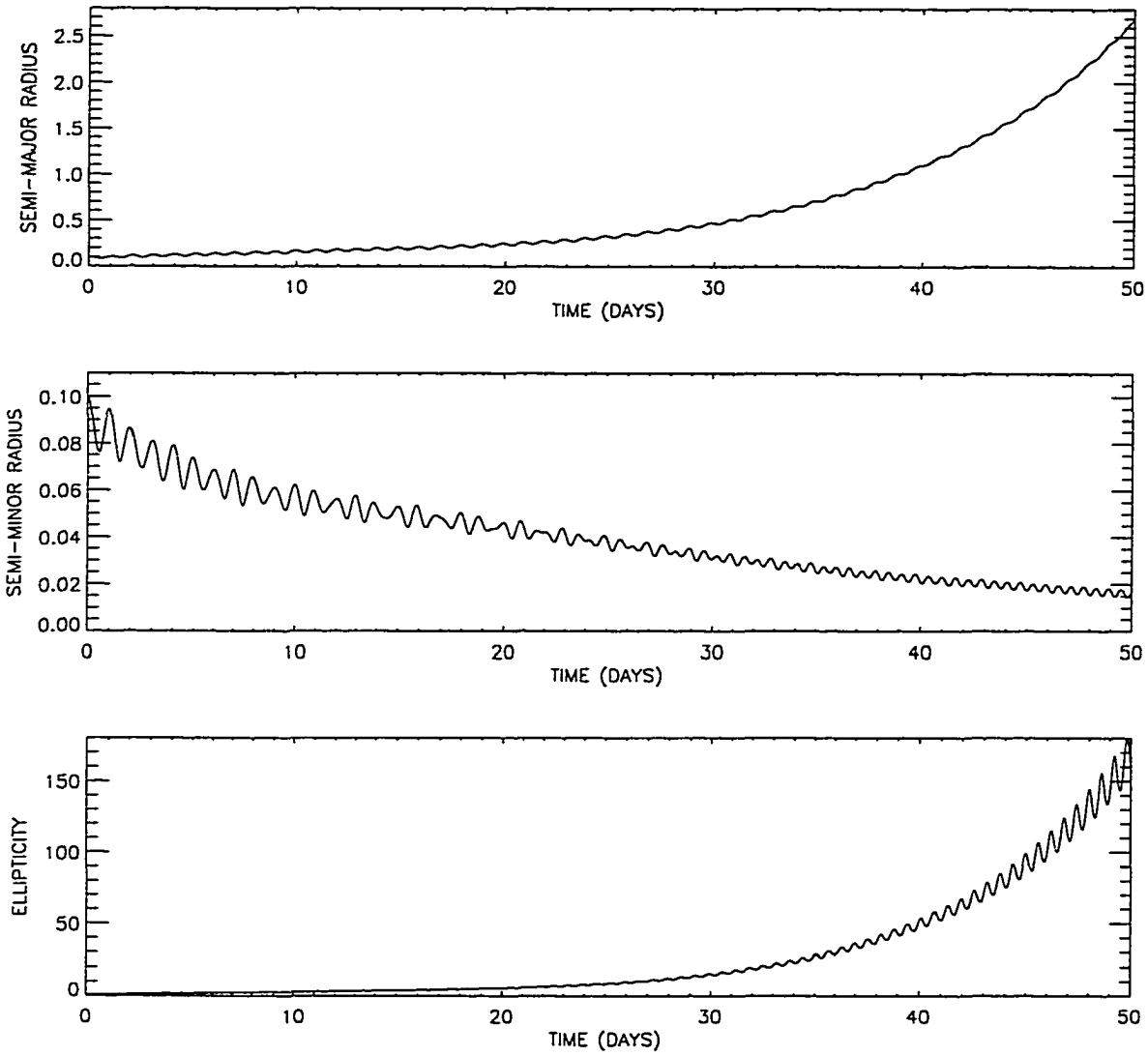

Figure 17: Time series of the major and minor axes of the lens from lens solution with $G_N = G_S = 0.01$. The upper panel is the major axis, the middle panel is the minor axis, and the lower panel is the ratio of major to minor axes.

solution can not simulate a shedding event, the PIC simulation presents a new solution to the forced problem. Previously, solutions to this problem could only be classified in two regimes, the stable, rotating ellipsoid or the unstable raingutter. The PIC model offers a new, intermediate solution regime.

Figure 18 shows an example of regime III, in which the forcing was so severe as to stretch the eddy into a long, thin filament – the so-called "raingutter" solution described by Brickman and Ruddick [1990]. In this case the forcing was $G_N = 0.01, G_S = 0.02$ and $G_R = G = 0.0$. In this example the lens deforms into an ellipse and begins to rotate anticyclonically. However, as the lens approaches an orientation aligned with the outflow axis of the forcing field, it begins to elongate dramatically. By day 15, the eddy has stretched into a long, thin filament. Shortly after day 17.5 the filament approached the edges of the model domain and the simulation was stopped. At no point later in time will the solution again resemble a coherent eddy. The orientation of the raingutter coincides with the outflow axis of the forcing field. Figure 19 is a time series of the centerline height of the lens and is consistent with the above analysis. The signal oscillates at the inertial frequency while the amplitude decreases with time as the lens elongates. Spectral analysis indicates that nearly 95% of the energy is at the lowest frequencies resolved, and only 5% of the energy is at the inertial frequency. By day 20, the inertial signal is difficult to discern. At the end of the 30 day simulation, the centerline height has decreased to only 16% of the average value of the initial oscillation and appears to be continuing to decrease.

Table 1 is a summary of the above results, showing the initial conditions and listing the corresponding figures for the example solutions for each of the regimes.

In the next set of experiments, anticyclonic vorticity was introduced into the forcing flow. The value of vorticity was prescribed to be $G_R = -0.01$ for all cases in this set. Figure 20 shows the matrix of parameters for this experiment and uses the same shapes as indicators of the regimes as in figure 10. Comparison of the solution

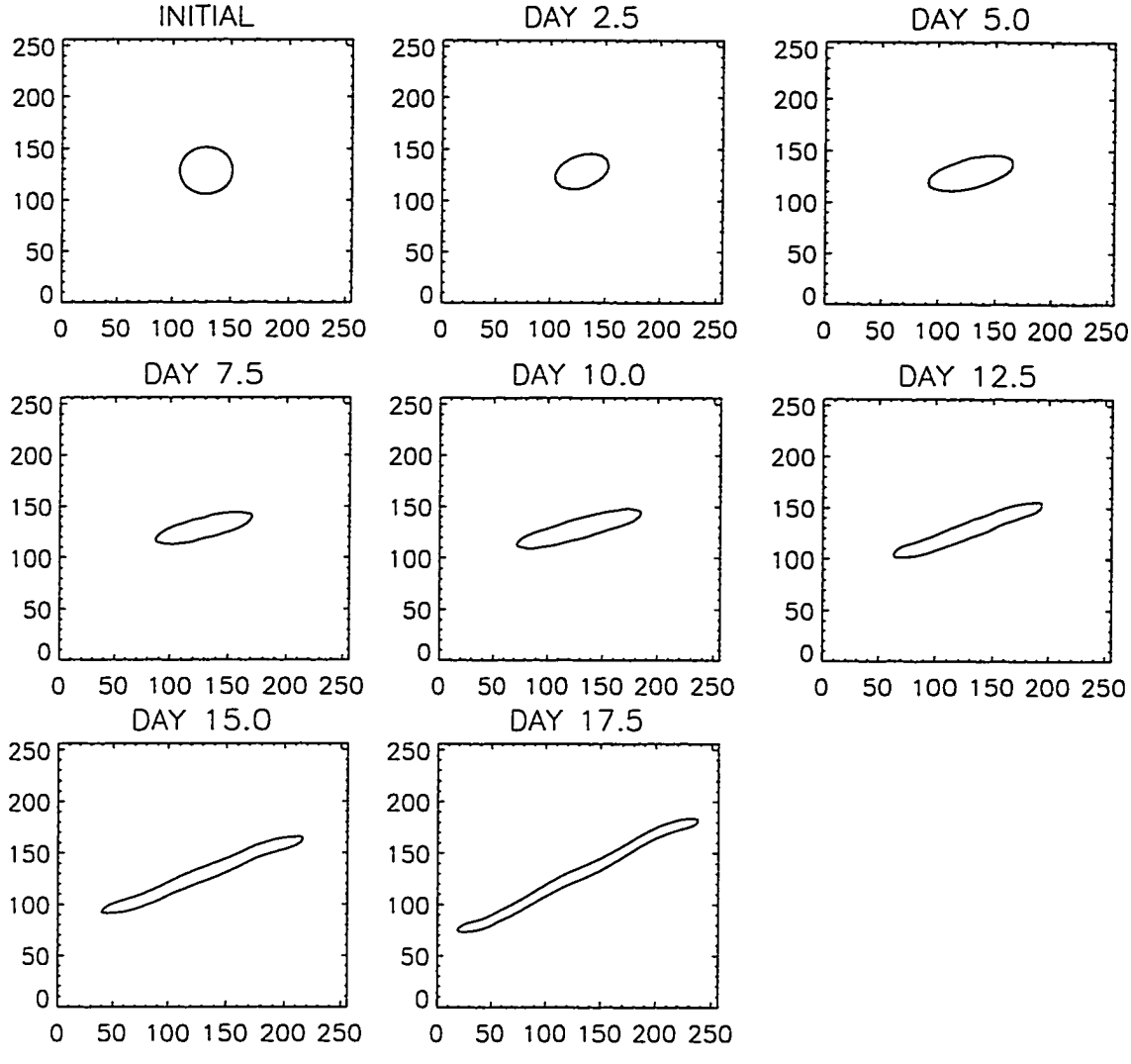

Figure 18: Evolution of the boundary of a lens in regime III. Here, $G_N = 0.01, G_S = 0.02$ and $G_R = G = 0.0$. The axes labels are the grid points in each direction.

Table 1: Initial conditions and corresponding figures for the three solution regimes with $G_R = G = 0$.

G_N	G_S	Simulation figure	Classification
0.005	0.0075	Figure 11	I – Rotating ellipsoid
0.01	0.01	Figure 13	II – Shedding ellipsoid
0.02	0.02	Figure 18	III – Unstable - Raingutter

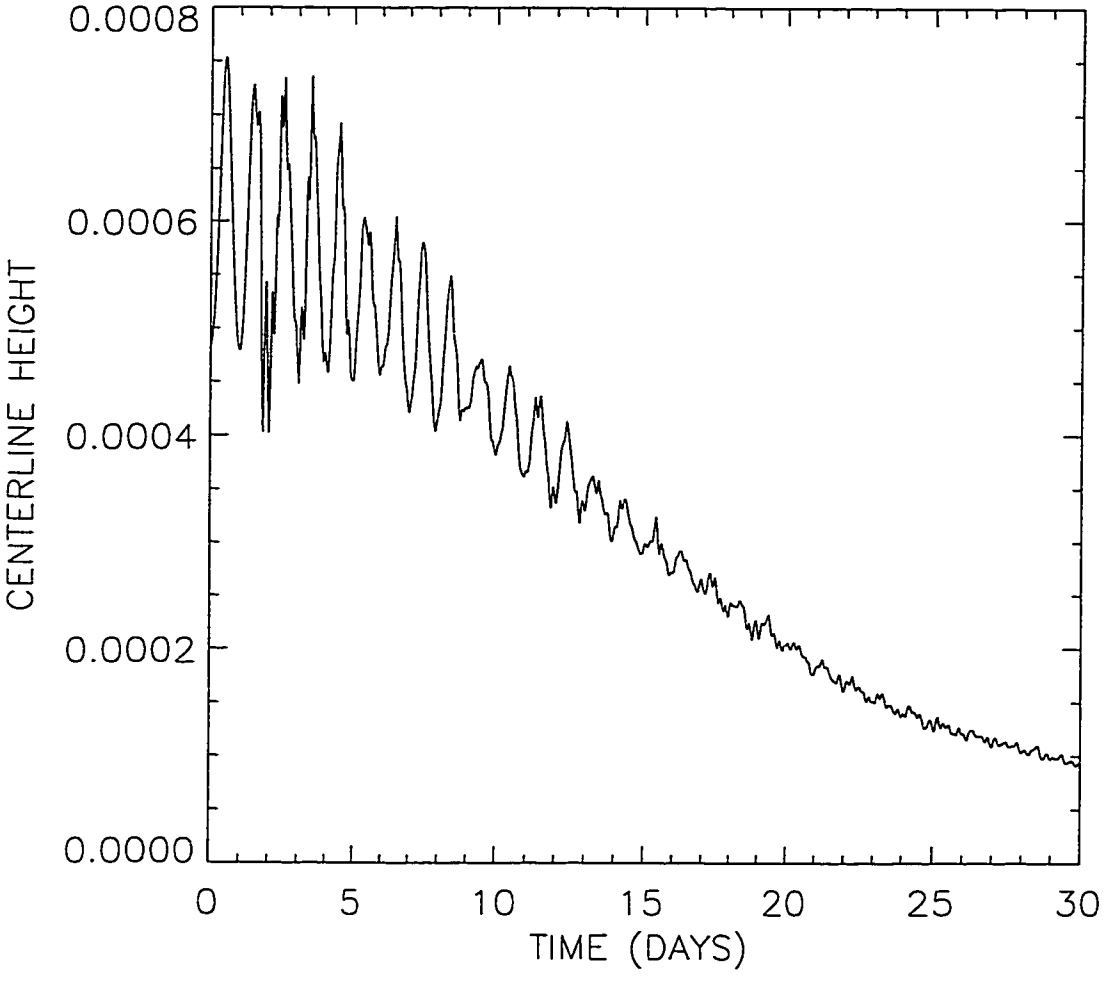

Figure 19: Time series of the centerline depth of the eddy in figure 18.

type between figures 10 and 20 for similar values of normal and shear deformation indicates that the anticyclonic vorticity in the exterior flow has a stabilizing effect. At values of deformation which previously caused the eddy to shed satellite eddies, the solution is now is one of a stable, rotating ellipsoid. Similarly, at forcing levels which pushed the eddy into the raingutter configuration with $G_R = 0.0$, the solution is now of the shedding type. Thus, the effect of introducing anticyclonic vorticity into the forcing field is to shift the boundary between regimes I, II and III to higher values of deformation.

A limited number of experiments were performed with cyclonic vorticity added to the lower layer flow. This had the opposite effect of the anticyclonic vorticity and acted to de-stabilize the eddy, i.e., the boundary between the regimes was shifted to lower magnitudes of deformation. For example, with $G_N = G_S = 0.0125$, $G_R = 0.01$ and $G = 0.0$, the solution was of the raingutter type (regime III). From figures 10 and 20 it can be seen that the solution was in regime II with $G_R = 0.0$ and regime I with $G_R = -0.01$.

Neither set of experiments considered divergence in the lower layer flow. Joyce and Kennelly [1985] measured little or no divergence below the thermocline in WCR 82-B. Furthermore, a constant, prescribed divergence in the lower layer flow would indicate an area of constant upwelling or downwelling beneath the eddy, which is unrealistic.

In both sets of experiments, with $G_R = 0.0$ and $G_R = -0.01$, for the solutions in regime I there exists a relationship between the magnitude of the forcing and the average rotation rate of the eddy. Figure 21 shows the rotation rate as a function of forcing magnitude, G_D, where $G_D = \sqrt{G_N^2 + G_S^2}$. There is a trend for the average rotation rate to decrease with increased forcing magnitude. The local minima in the curve for $G_R = -0.01$ is a result of G_D being a non-unique function of G_N, G_S. However, for any given value of G_N (G_S) the rotation rate of the eddy decreases

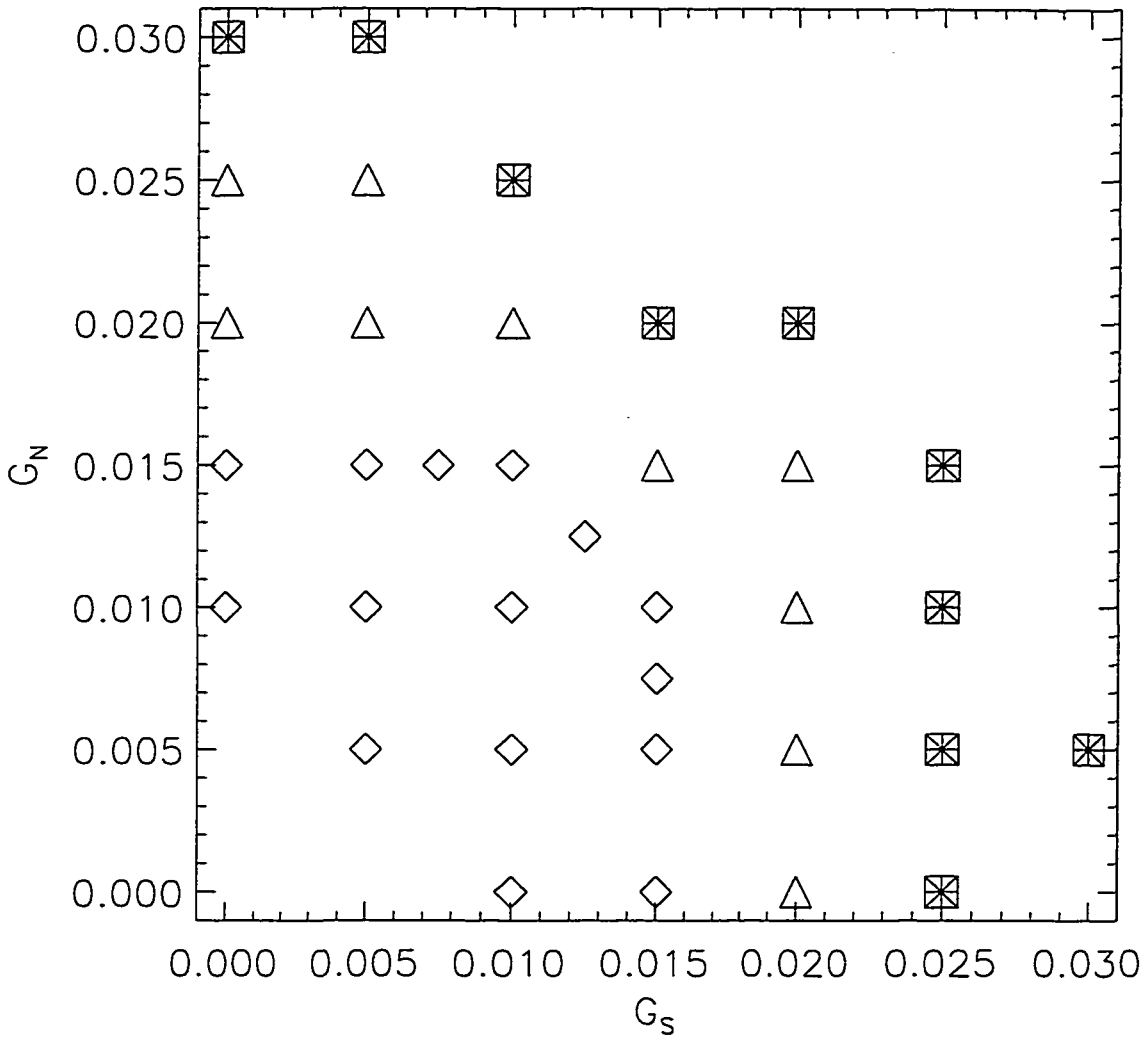

Figure 20: Stability diagram for the experiments with anticyclonic vorticity ($G_R = -0.01$). Solutions in regimes I, II, and III are indicated by diamonds, triangles, and crossed-squares, respectively.

monotonically with G_S (G_N). Also note that for a given forcing magnitude, the rotation rate is greater in the experiments with vorticity in the exterior flow than in the cases with zero vorticity. The range of rotation rates reported here is consistent with values observed of warm-core rings. Hooker et al. [1997] derived rotation rates of 4° to 10° per day from AVHRR satellite imagery.

A relationship also exists between the forcing magnitude and the maximum ellipticity attained by the lens. This is shown in figure 22 for the experiments with $G_R = 0.0$ and $G_R = -0.01$. This figure shows that ellipticity increases monotonically with the forcing magnitude. This is consistent with the findings of Ruddick [1987]. In addition, for a given magnitude of forcing, the ellipticity is greater for the cases with $G_R = 0.0$ than in those with $G_R = -0.01$.

The cause of these relationships is likely that as the forcing magnitude is increased, the lens is more likely to be oriented with and stretched along the principal axis of the forcing flow. Thus, increased forcing produces more elliptical eddies with slower rotation rates. Adding vorticity to the flow increases the rotation rate and decreases the likelihood that the lens will be oriented or stretched along the principal axis. This explains the increased rotation rate and decreased ellipticity in the experiments with anticyclonic vorticity.

4.3 Two-layer Model

4.3.1 Analytical steady-state solutions to two-layer equations

In order to evaluate the two–layer model, analytical steady-state solutions to equations (7) – (8) are sought. The model can then be tested by its ability to reproduce the steady-state solutions. The following analysis has not been previously given in literature, so the details will be shown here. First, solutions will be sought in which the lower layer is motionless outside the region below the upper layer. Then, the solution is adapted to include motion in the exterior region.

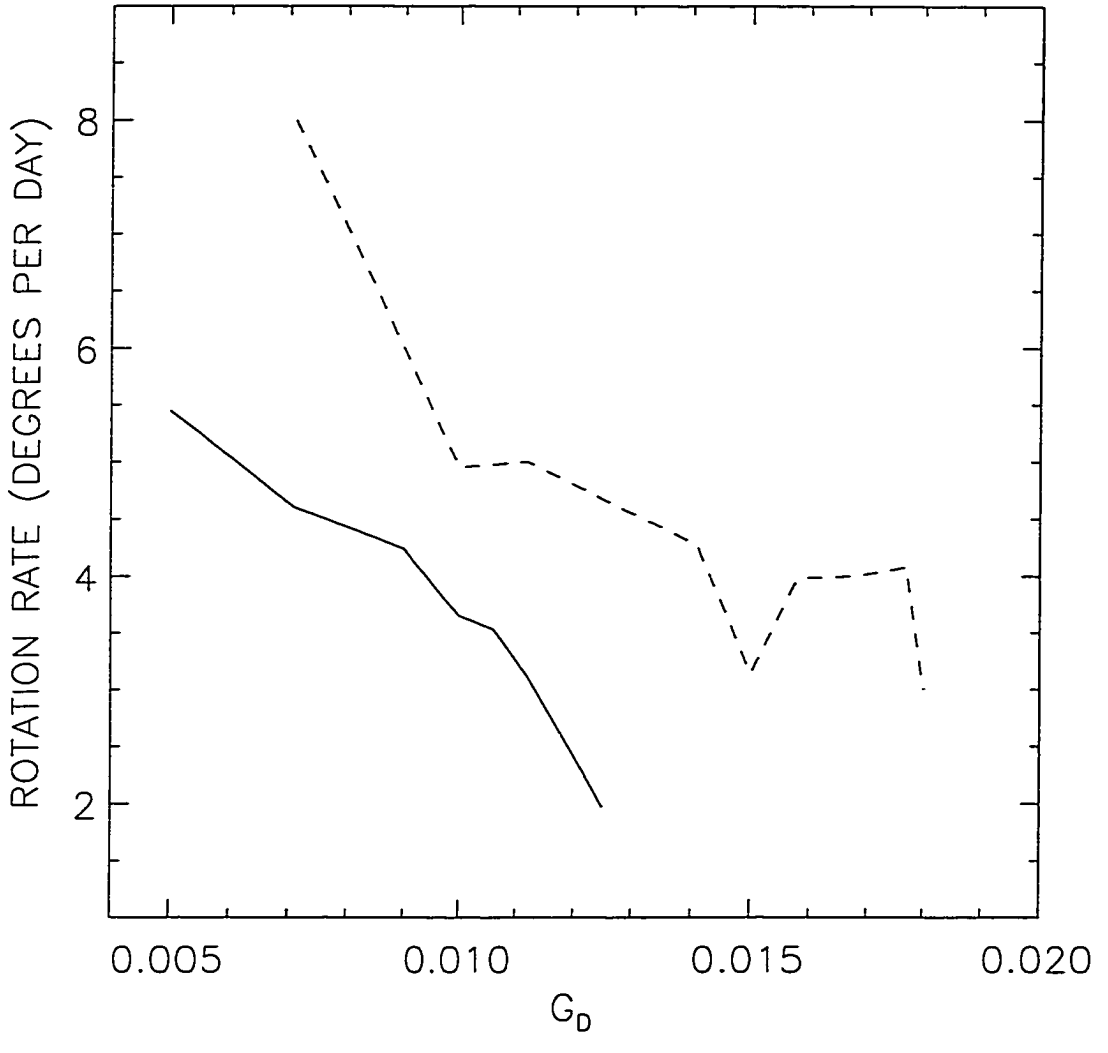

Figure 21: Rotation rate of the eddy versus forcing magnitude. The solid line is from the experiments with no vorticity ($G_R = 0.0$); the dashed line is from the experiments with anticyclonic vorticity ($G_R = -0.01$).

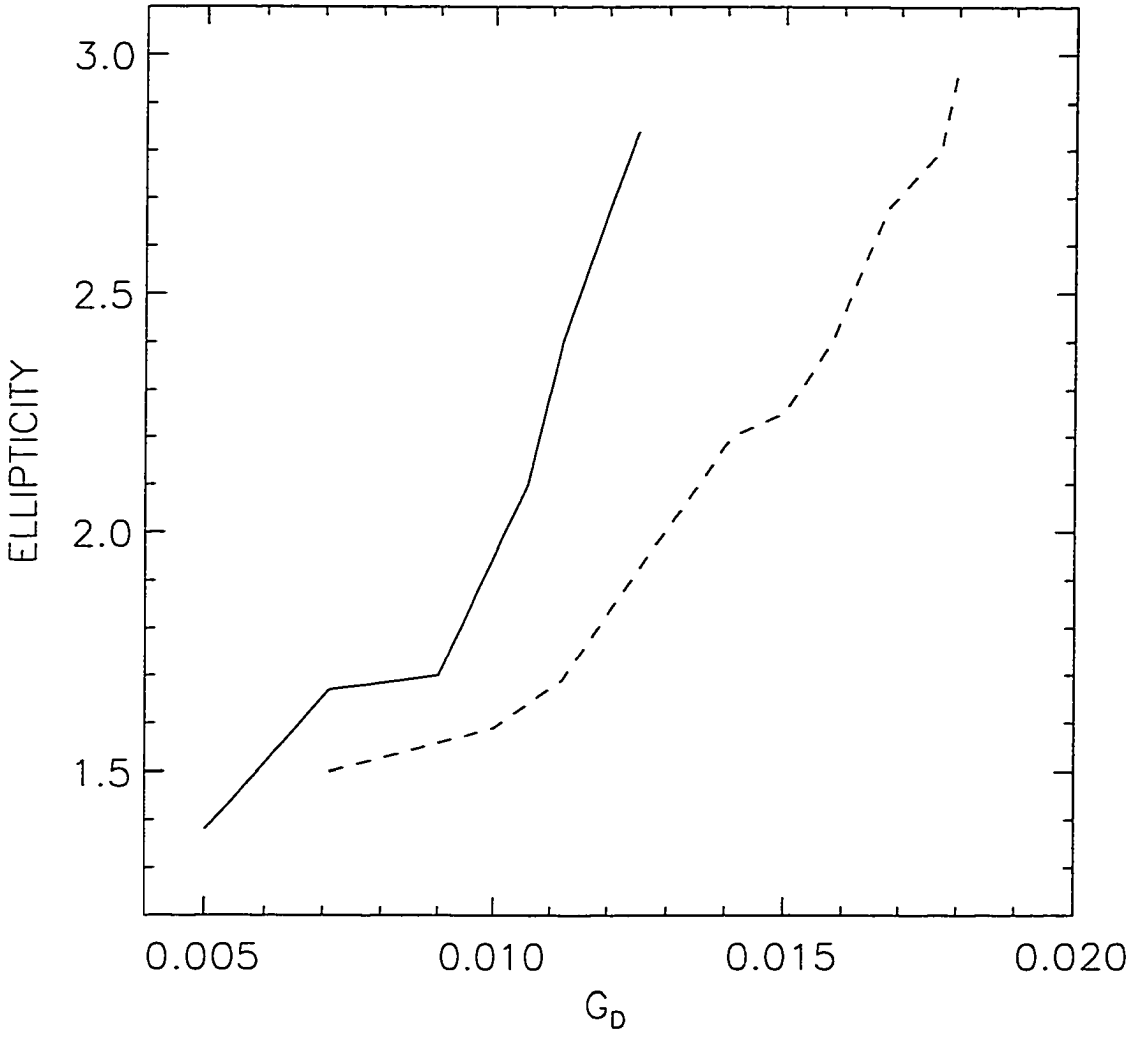

Figure 22: Maximum lens ellipticity as a function of forcing magnitude. The solid line is from the experiments with no vorticity ($G_R = 0.0$); the dashed line is from the experiments with anticyclonic vorticity ($G_R = -0.01$).

Solution with zero exterior velocities

The upper layer is given a parabolic depth profile with a maximum depth of h_0. It extends above the reference level with a parabolic height profile of maximum height of $h_0\alpha$. The lower layer is a constant depth, given by h_{20}, outside the lens and parabolic beneath it. Mathematically, this is given by,

$$\begin{aligned} h_1 &= h_0(1+\alpha)(1-(r/R)^2) && r \le R, \\ &= 0 && r > R, \end{aligned} \tag{42}$$

$$\begin{aligned} h_2 &= h_{20} - h_0(1-(r/R)^2) && r \le R, \\ &= h_{20} && r > R, \end{aligned} \tag{43}$$

where R is the radius of the lens.

The non-dimensionalized equations (7) – (8) then reduce to,

$$\frac{du_1}{dt} - v_1 = -\frac{\partial(h_1+h_2)}{\partial x} = 2h_0\alpha x/R^2, \tag{44}$$

$$\frac{dv_1}{dt} + u_1 = -\frac{\partial(h_1+h_2)}{\partial y} = 2h_0\alpha y/R^2, \tag{45}$$

$$\frac{du_2}{dt} - v_2 = -\frac{\partial(h_1+h_2+\delta h_1)}{\partial x} = 2h_0\alpha x/R^2 - 2\delta h_0(1+\alpha)x/R^2, \tag{46}$$

$$\frac{dv_2}{dt} + u_2 = -\frac{\partial(h_1+h_2+\delta h_1)}{\partial y} = 2h_0\alpha y/R^2 - 2\delta h_0(1+\alpha)y/R^2, \tag{47}$$

where $\delta = (\rho_2 - \rho_1)/\rho_2$ and A_h has been taken to be zero.

For steady-state, $d\mathbf{u}_i/dt = 0$. Now, let $\alpha = C\gamma$, where $\gamma = (\rho_2 - \rho_1)/\rho_1$. There are three cases that arise by the choice of C. In each case, the upper layer is rotating anticyclonically; the three cases differ in the motion of the lower layer in the region directly below the lens. Obviously from equations (42) – (43), no motion exists in

either layer in the region $r > R$. In the first case, let $C = 1$; thus $\alpha = \gamma$. Equations (46) – (47) then reduce to,

$$u_2 = 2h_0 y[\gamma - \delta(1+\gamma)]/R^2 = 0, \tag{48}$$

$$v_2 = -2h_0 x[\gamma - \delta(1+\gamma)]/R^2 = 0. \tag{49}$$

Thus, in this case there is no motion in lower layer.

In the second case $C > 1$; i.e., $\alpha > \gamma$. Then equations (46) – (47) become,

$$u_2 = 2h_0 y[C\gamma - \delta(1+C\gamma)]/R^2 \quad \begin{array}{l} > 0 \text{ for y} > 0, \\ < 0 \text{ for y} < 0, \end{array} \tag{50}$$

$$v_2 = -2h_0 x[C\gamma - \delta(1+C\gamma)]/R^2 \quad \begin{array}{l} < 0 \text{ for x} > 0, \\ > 0 \text{ for x} < 0. \end{array} \tag{51}$$

This describes anticyclonic motion in the region of the lower layer beneath the lens.

In the third case $C < 1$; i.e., $\alpha < \gamma$. Then the equations reduce to,

$$u_2 = 2h_0 y[C\gamma - \delta(1+C\gamma)]/R^2 \quad \begin{array}{l} < 0 \text{ for y} > 0, \\ > 0 \text{ for y} < 0, \end{array} \tag{52}$$

$$v_2 = -2h_0 x[C\gamma - \delta(1+C\gamma)]/R^2 \quad \begin{array}{l} > 0 \text{ for x} > 0, \\ < 0 \text{ for x} < 0. \end{array} \tag{53}$$

In this case, cyclonic motion in lower layer results beneath the upper layer lens.

Physically, the variable C describes the height which the upper layer extends above the reference level relative to that which is expected from a geostrophic balance with the anticyclonic flow in the upper layer; C is the the ratio of γ to α. When C equals 1, $\alpha = \gamma$, and the height is exactly as expected in a geostrophic balance; no motion is present in the lower layer. When C is greater than 1 ($\alpha > \gamma$), the lens extends more above the reference level than is supported by the motion

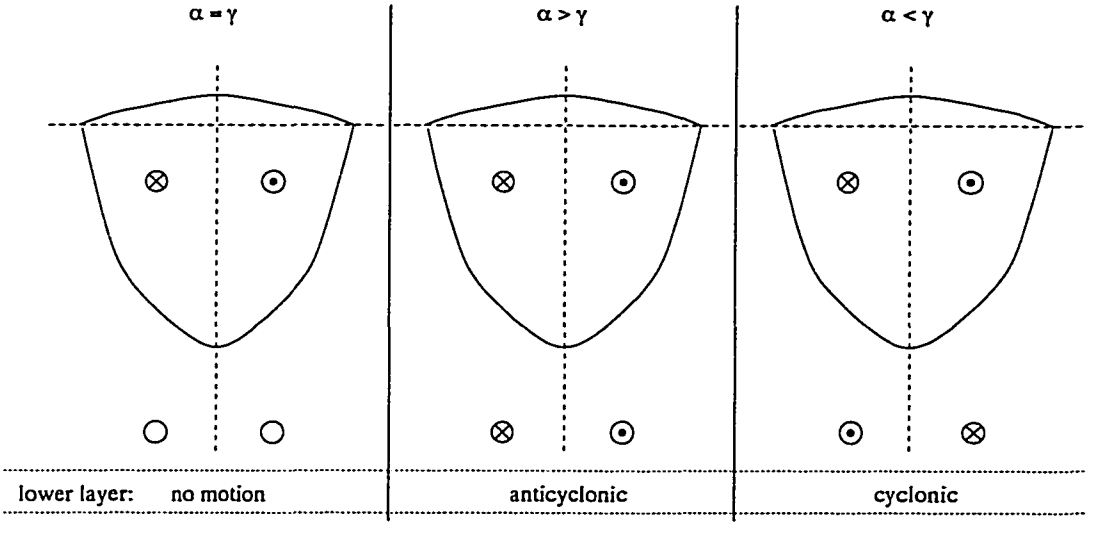

Figure 23: Schematic of the three equilibrium solutions to the two-layer equations. α is a parameter and $\gamma = (\rho_2 - \rho_1)/\rho_1$. Velocities in the exterior region of the lower layer may be zero or exponentially decaying.

of the upper layer. The "source" of this extra height must be anticyclonic motion in the lower layer. Finally, when C is less than 1 ($\alpha < \gamma$), the opposite is true and cyclonic motion must exist in the lower layer. These three cases are shown in schematic form in figure 23. It is worthy to note that Joyce and McDougall [1992] reported observations of cyclonic motion at depth below WCR 82-B.

Solution with non-zero exterior velocities

The above equilibrium solutions are enlightening, however, they lack flow in the lower layer outside of the region beneath the lens. It is desirable to consider solutions with non-zero velocities in the exterior region. Thus, a steady-state solution with exponentially decaying lower layer velocities will be developed. This choice allows a velocity matching condition to be applied at the boundary of the lens and facilitates the application of boundary conditions at model domain boundaries, since there the lower layer velocities will be near zero. First assume the velocities in the exterior region ($r > R$) are given by,

$$u_2 = \Gamma_1 y e^{-r/R}/r, \tag{54}$$

$$v_2 = \Gamma_2 x e^{-r/R}/r, \tag{55}$$

and let,

$$h_2 = \mathcal{H} + \beta e^{-r/R}, \tag{56}$$

The parameters Γ_1, Γ_2, $\mathcal{H}$, and β are yet to be determined. In the region $r \leq R$, the solution is as derived above.

Now from equations (8), the steady-state balance is

$$u_2 = \Gamma_1 y e^{-r/R}/r = \frac{\beta}{R} e^{-r/R} y/r, \tag{57}$$

$$v_2 = \Gamma_2 x e^{-r/R}/r = \frac{\beta}{R} e^{-r/R} x/r, \tag{58}$$

which gives,

$$\Gamma_1 = \frac{\beta}{R}, \tag{59}$$

$$\Gamma_2 = \frac{-\beta}{R}. \tag{60}$$

To achieve continuity of velocity, the interior and exterior solutions should match at $r = R$. Denoting the interior solution with superscript $()^-$ and the exterior solution with $()^+$ this gives,

$$u_2^- = \frac{2h_o y}{R^2}[\alpha - \delta(1+\alpha)] = \Gamma_1 y e^{-1}/R = u_2^+, \tag{61}$$

and

$$v_2^- = \frac{-2h_o x}{R^2}[\alpha - \delta(1+\alpha)] = \Gamma_2 x e^{-1}/R = v_2^+. \tag{62}$$

Then from equations (61) and (62), respectively, Γ_1 and Γ_2 are determined in terms of the physical parameters:

$$\Gamma_1 = 2h_o[\alpha - \delta(1+\alpha)]e/R, \tag{63}$$

$$\Gamma_2 = -2h_o[\alpha - \delta(1+\alpha)]e/R. \tag{64}$$

Finally, from equation (59) or (60), β is determined:

$$\beta = 2h_o[\alpha - \delta(1+\alpha)]e. \tag{65}$$

The final parameter to determine is $\mathcal{H}$. Again by requiring continuity at the lens boundary, it is found to be,

$$\mathcal{H} = H - \beta e^{-1} \tag{66}$$

where H is the reference height of the lower layer.

The above analysis completely describes a steady-state solution with non-zero velocities in the lower layer exterior to the lens. As in the case with no motion in the exterior region, the choice of α will determine if this motion is anticyclonic ($\alpha > \gamma$), cyclonic ($\alpha < \gamma$), or if there is no flow ($\alpha = \gamma$).

4.3.2 Model steady-state solutions

An initial test of the two–layer model is its ability to reproduce the analytical steady-state solutions presented in section 4.3.1. The first case presented here is the solution with anticyclonic motion in both layers and an exponentially decaying velocity field in the lower layer (i.e., $\alpha > \gamma$). The model was initialized in the

steady state and run for a 10-day simulation. Profiles of the lens at several times throughout the simulation (not shown) show no discernable difference with time. The maximum difference between the initial and final height profiles after a 10-day simulation was less than 0.3%. Although some adjustment appears to have taken place, the difference between the initial and final states is minor. Figure 24 illustrates this difference. This shows profiles of the upper layer east-west velocity initially and at several intervals throughout the simulation. A slight adjustment is apparent near the edge of the lens, but otherwise the solution is near the initial state and nearly constant in time. Figure 25 is a similar comparison for the lower layer east-west velocity profile. In the lower layer, the interior of the solution is still linear, indicating solid body rotation. However, the magnitude of the maximum velocity has decreased slightly, and the profile is more rounded near the edge of the lens. In the region exterior to the lens, the velocity goes to zero more quickly and has less (and opposite) concavity than in the initial field. Furthermore, there is a region of near zero velocity near the boundaries; this region coincides with the location of the sponge layer.

A likely cause of the differences between the analytical and numerical solutions is the inclusion of viscosity. As noted in section 3.1 above, viscosity was included in the numerical model; however, it was not considered in the analytical solution presented in section 4.3.1. The differences between the initial and later velocity profiles are most pronounced where there is a change in slope of the profile, i.e., where the viscous terms are largest.

Several tests were done to evaluate the sensitivity of the model to the choice of the horizontal viscosity coefficient, A_h. The typically accepted range of values is $10^2 - 10^5$ m^2 s^{-1}, which when non-dimensionalized for the model equates to a range of $10^{-6} - 10^{-3}$. Because this term parameterizes diffusion effects at scales not resolvable by a given model, smaller values are assumed when modeling smaller-scale

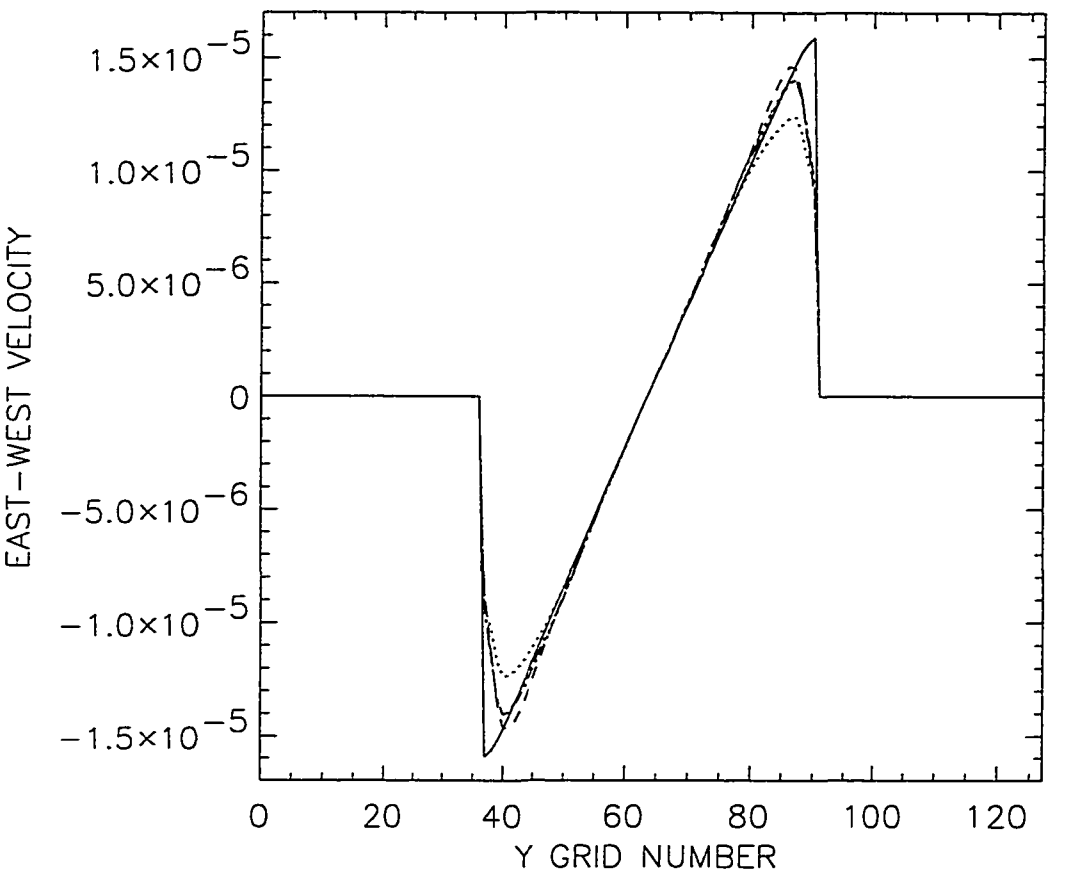

Figure 24: Profile of the upper layer east-west velocity at several times throughout a 10-day simulation for the two-layer steady case with anticyclonic motion in both layers. The solid curve is the initial profile. The dotted, dashed, dash-dotted, and dash-dot-dot-dotted lines are the profiles at 2.5, 5.0, 8.0 and 10.0 days, respectively.

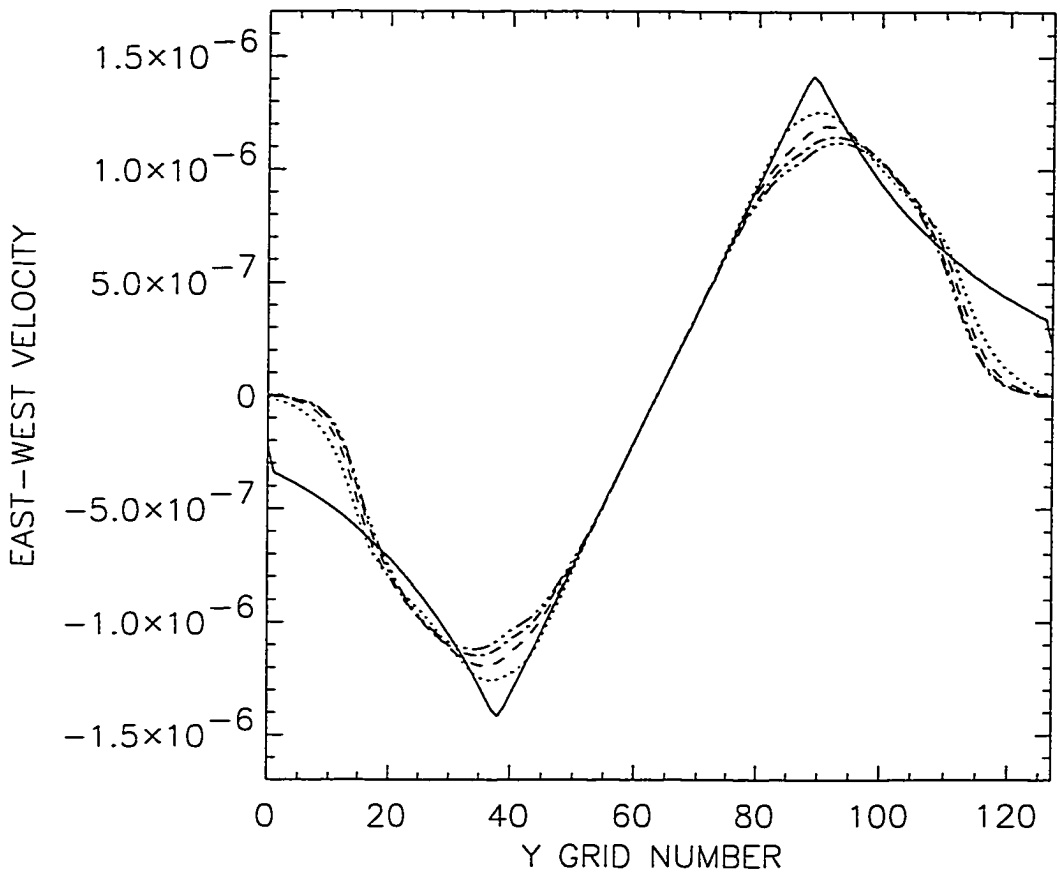

Figure 25: Profile of the lower layer east-west velocity at several times throughout a 10-day simulation for the two-layer steady case with anticyclonic motion in both layers. The solid curve is the initial profile. The dotted, dashed, dash-dotted, and dash-dot-dot-dotted lines are the profiles at 2.5, 5.0, 8.0 and 10.0 days, respectively.

dynamics, and similarly larger values are taken when modeling on larger scales. All results from the two-layer model presented here used a value of $A_h = 1 \times 10^{-5}$. This value being at the lower end of the range is consistent with the nature of the PIC model, since it has high resolution and utilizes particles to describe and define the dynamics. However, all values within the above-stated range produced qualitatively similar results in the PIC model. The expected and observed trend is that higher values of A_h result in more effective damping of short-wave energy. However, it can be shown by linear stability analysis that choosing a value of A_h which is too large can actually cause a dynamic instability. In such a case, wave energy at the shortest wavelengths will be amplified. This behavior was observed in experiments with the PIC model in which the viscosity coefficient was prescribed to a value outside the range given above.

The next experiment was a test of the model's ability to reproduce the analytical solution with cyclonic motion in the lower layer and exponentially decaying velocities in the exterior region (i.e., $\alpha < \gamma$). Motion in the upper layer was again anticyclonic. Figure 26 shows profiles of the lower layer east-west velocity at several times throughout the simulation. The results are similar to those described above in the case with anticyclonic motion in both layers. The velocity profile is somewhat modified in the exterior region but retains the shape and nearly the magnitude of the initial profile in the interior region. The upper layer velocity profile (figure not shown) is nearly identical to that shown in figure 24 for the above case with $\alpha > \gamma$.

4.3.3 Model spin-up experiment

An interesting problem to explore with the two–layer model is the spin-up of the lower layer beneath an anticyclonic eddy. This also serves as a test of the robustness of the model. To study this problem, the upper layer was initialized as in the steady-state case described in section 4.3.1, however, the lower layer velocities were initially

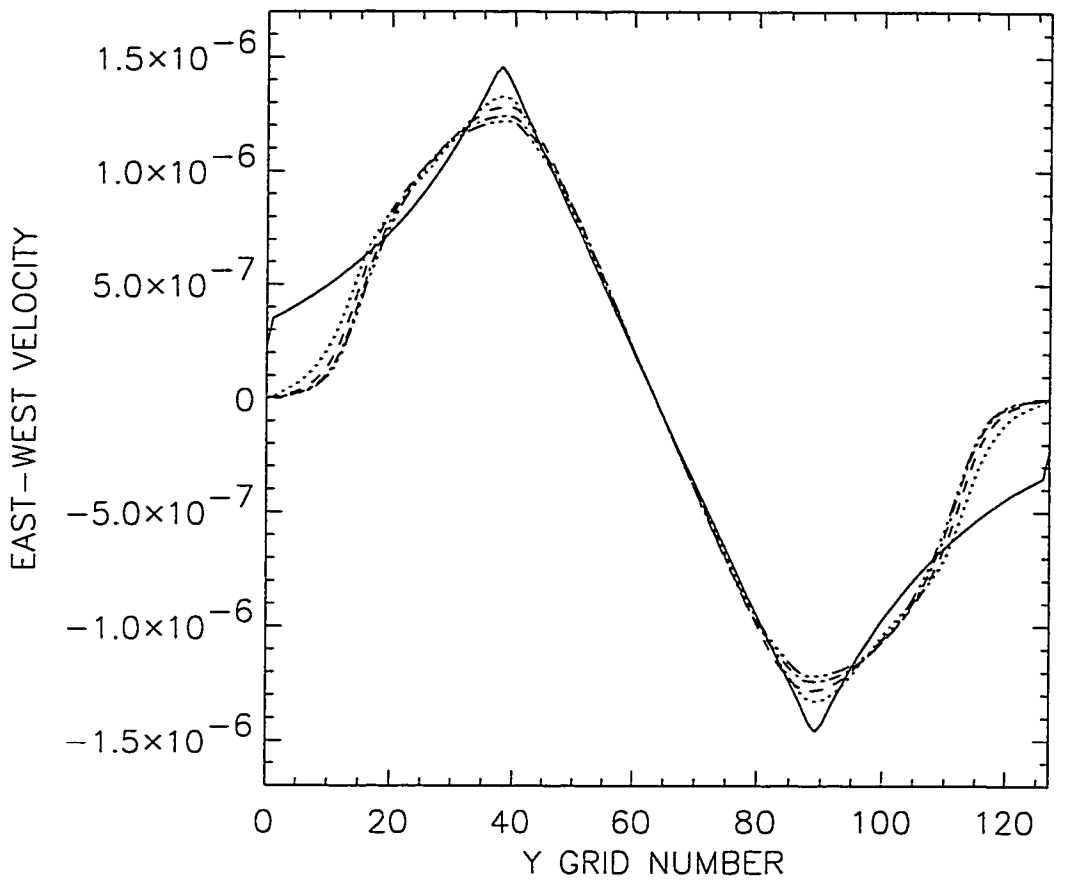

Figure 26: Profile of the lower layer east-west velocity at several times throughout a 10-day simulation for the two-layer steady case with cyclonic motion in the lower layer. The solid curve is the initial profile. The dotted, dashed, dash-dotted, and dash-dot-dot-dotted lines are the profiles at 2.5, 5.0, 8.0 and 10.0 days, respectively.

prescribed to be zero. The height fields in both layers were initialized as in the steady-state case with anticyclonic motion in the lower layer and exterior region.

The model results indicate that the lower layer quickly spins-up towards an equilibrium state. Figure 27 shows the lower layer east-west velocity profile at several times throughout a 10-day simulation. Also shown is the final velocity profile from the numerical steady-state solution discussed in section 4.3.2. The initial lower layer velocity was zero everywhere, but by day 2.5, the velocity quickly spun-up to approximately half the magnitude of the steady-state solution. By day 5.0, the velocity in the lower layer decreased slightly in magnitude but retained the general profile of the steady-state solution. The magnitude of the velocity varied slightly with time, however, by day 8.0 the lower layer velocities were in near equilibrium state and showed very little variability thereafter. In the final state, the magnitude of the velocities is about one-third of that of the steady-state solution. This is a consequence of there being less kinetic (and total) energy in the initial state. Although the magnitude of the lower layer velocities is less than that from the analytical solution, the profile is very similar to that of the numerical solution in the steady-state case. The most significant difference is in the slope of the profile in the interior region. However, as in the steady-state solution, the spun-up profile is nearly linear in the interior, indicating a region of solid body rotation.

There are several other interesting features to note from this experiment. First, the lower layer velocities spun-up to their maximum at day 2.5. This was a reaction to shocking the system with forcing from the initial height field. The lower layer velocities initially overshot the equilibrium state and relaxed towards an equilibrium state thereafter. The energy for this overshoot was taken from the upper layer. As indicated in figure 28, the upper layer velocity profile showed a minimum at day 2.5 but otherwise was nearly constant in time. Second, the areal extent of the core of anticyclonic motion in the lower layer was greater than in the steady-state case;

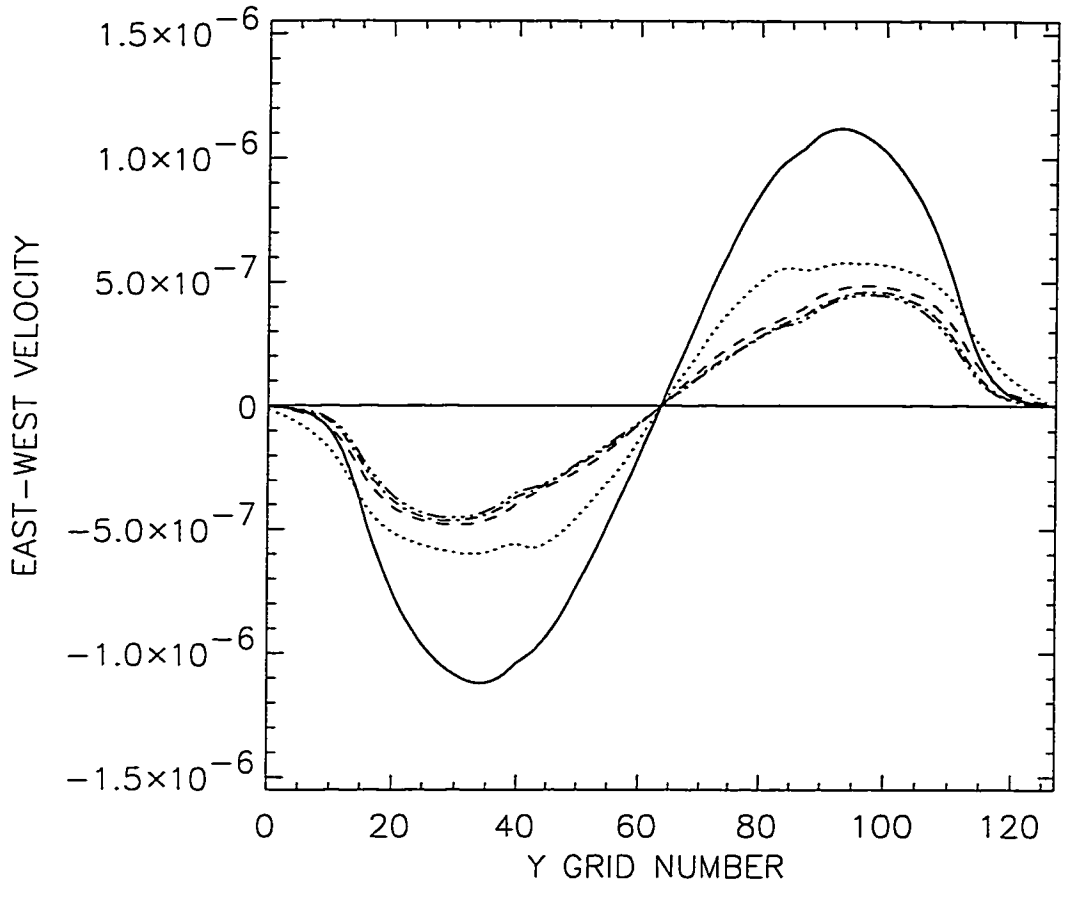

Figure 27: Lower layer velocity profile at several times throughout a 10-day simulation from the spin-up experiment. The solid, flat line is the initial profile. The dotted, dashed, dash-dotted, and dash-dot-dot-dotted lines are at 2.5, 5.0, 8.0, and 10.0 days, respectively. The thick, solid line is the final profile from the steady-state case discussed in section 4.3.2

i.e., the velocity profile has a maximum at a slightly larger radius. Also of note is a slight "kink" in the profiles, most noticeable early in the simulation, near grid points 40 and 85. This kink aligns with the velocity maximum in the upper layer (see figure 28).

The upper layer velocities underwent a slight adjustment as in the steady-state solution discussed in section 4.3.2. Again this is presumed to be due to the difference between the inviscid analytical solution and the numerical solution which included viscosity.

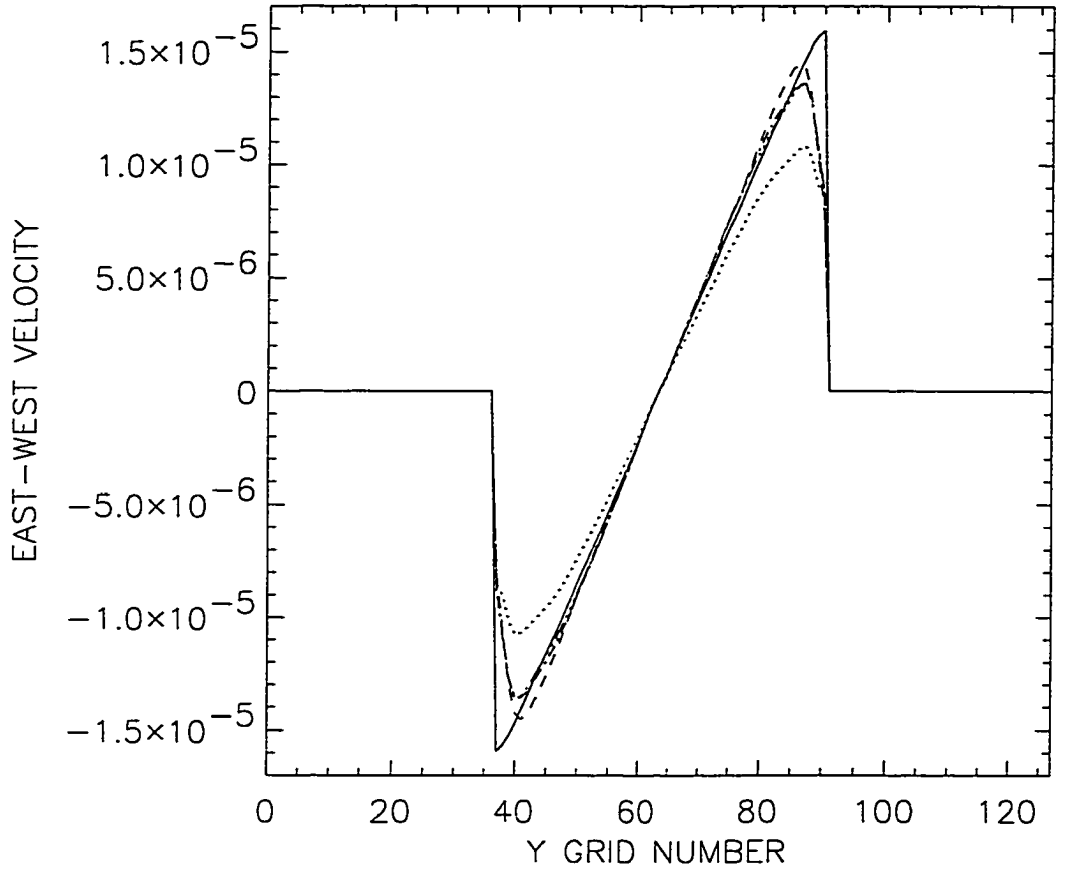

Figure 28: Upper layer velocity profile at several times throughout a 10-day simulation from the spin-up experiment. The solid line is the initial profile. The dotted, dashed, dash-dotted, and dash-dot-dot-dotted lines are at 2.5, 5.0, 8.0, and 10.0 days, respectively.

4.4 Parallel speed-up

As mentioned in section 3.5, the PIC method is ideally suited to parallelization, and all model runs reported in this study were executed on a parallel processing computer. This section describes the speed-up in run time for the parallel algorithm as a function of the number of processors. It is important to note that the same-sized problem was run in all cases discussed here. The speed-up reported is not scaled speed-up in which the problem size is increased with the number of processors.

Figure 29 shows the speed-up as a function of the number of processors, n, for a one-day simulation with the two-layer model. Here, speed-up is defined as the ratio of the run time with one processor to the run time with n processors. Note that it is not practical to run the two-layer model on fewer than four processors, since that model typically uses on the order of 10^7 particles and thus requires a large amount of memory. Table 2 shows the raw data of run time versus the number of processors. There are several interesting features in the data shown in figure 29 and table 2. First, there is a nearly linear speed-up when using up to 16 processors, i.e., the execution time using 16 processors is approximately one-sixteenth of that when using four processors. Although the run time still decreases significantly when using 32 processors, the speed-up is less than linear. With this number of processors communication between nodes becomes a significant factor in run time. Each processor has less work to do and spends a larger percentage of time communicating with other nodes. Note, however, that a larger problem with more particles would better utilize more nodes and the drop off from linear speed-up would occur with a greater number of processors. A second interesting feature in these data is that the speed-up from four processors to eight processors is even better than a factor of two. While at first this seems impossible, the reason behind this is load balancing. The model code is written such that each node is responsible for particles in either the upper or lower

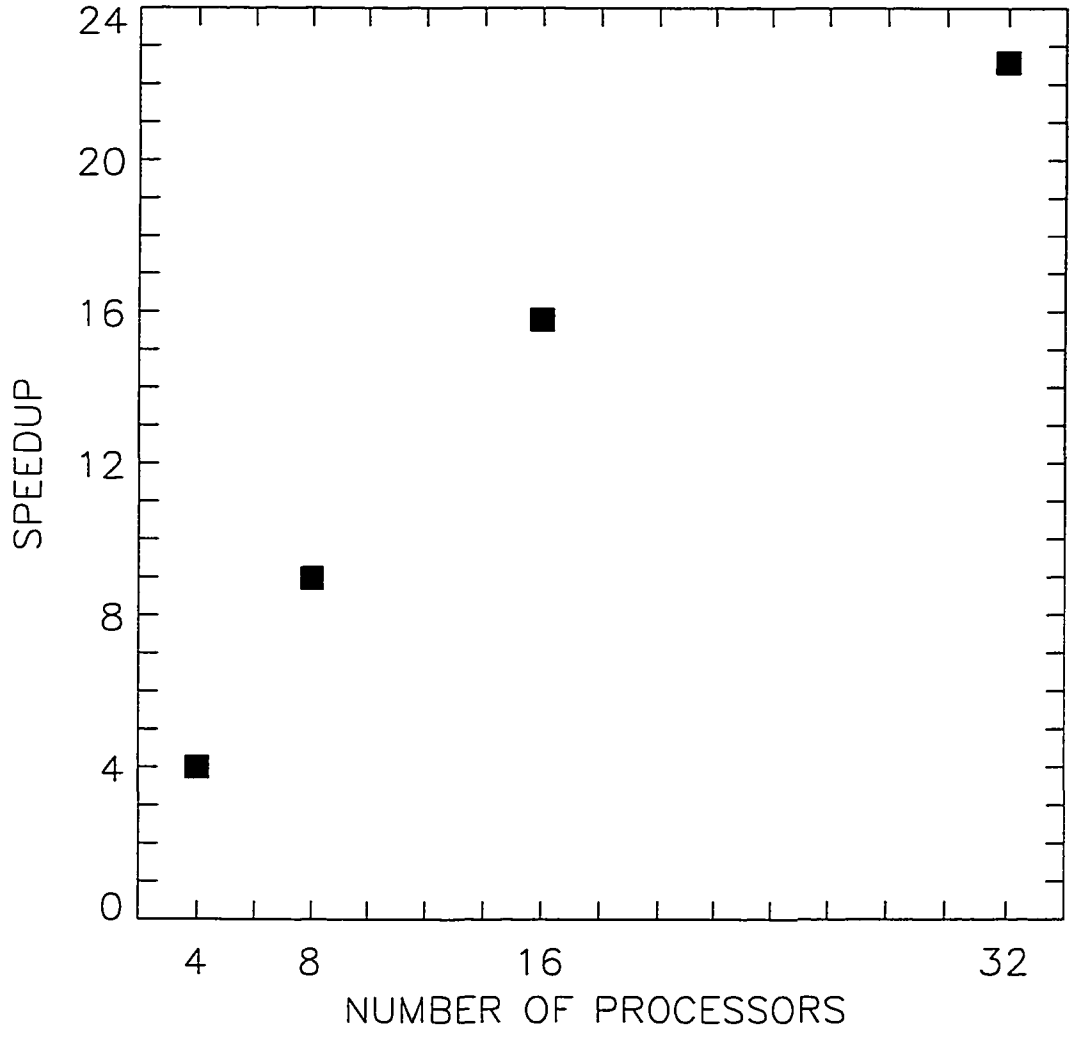

Figure 29: Speed-up of the parallel algorithm as a function of the number of processors for the two-layer model. The speed-up is defined as the ratio of the run time with 1 processor to that with n processors.

Table 2: Timings for the two-layer model.

Number of Processors	Length of Simulation (days)	Time (mins.)
4	1.0	77.6
8	1.0	34.6
16	1.0	19.6
32	1.0	13.8

layer, but not both. Thus, better load balancing is achieved when the ratio of the number of particles in the lower layer to that in the upper layer is an integer. Then, this ratio can be used to determine how many processors to assign to each layer. In the case with four processors, one processor, the minimum possible, was assigned to upper layer while the other three were assigned to the lower layer particles. This ratio of three to one was significantly different from the ratio of the particle count between the two layers, which for these two-layer experiments was close to eight to one. Therefore, the run with eight processors had better load balancing and thus was a more efficient use of the processors. Finally note that although this model was not run with just one processor, an estimate of the run time can be made by extrapolating the data backwards. The result of this is an approximate run time of 4.6 hours. Therefore, the use of parallel processing reduced the run time of this code from 4.6 hours to under 14 minutes for a one-day simulation. This dramatically demonstrates the utility of the parallel environment for the PIC model. The parallel implementation of the model also eliminates restrictions on resolution and particle numbers experienced in previous PIC investigations.

5 DISCUSSION

5.1 Model Results

In several of the simulations, the initially circular eddy deformed into an elliptical shape and eventually split into smaller, multiple eddies. The shedding regime constitutes new solutions to the forced problem. Previous methods of investigation of the effect of environmental shear, which used various solutions to the lens equations, were restricted in the solution forms they could depict. Using PIC techniques, Pavia [1989] showed shedding events resulting from the instability of an elliptical eddy. However, the instability was due to the lens geometry; exterior forcing was not considered.

It is interesting to speculate why there are few observations of such shedding events. First, even with satellite observations, the frequency of observations of warm-core rings is low. Indications from this and other studies are that shedding events are rapid and thus could easily be missed by observations. Second, relatively few studies have utilized zebra palettes for analysis of AVHRR sea surface temperature data. As shown in Hooker et al. [1995], the use of zebra palettes greatly enhances the features resolved in satellite imagery. Thus, it is possible that studies not utilizing zebra palettes may have missed shedding events. Finally, as shown in this study, rings encountering shedding-favorable forcing will in fact shed satellite eddies and then become stable rotating ellipsoids. Eddies undergoing more severe forcing will break up. Thus, the rotating ellipsoid is the final state in two of the three regimes presented here, and it should be the most commonly observed.

Considering the shedding events, a logical question to ask is if adaptive grid methods might be useful with this method. With the fixed grid used in this study, the dimensional grid resolution is on the order of 2 km. In addition, the Lagrangian particles provide some resolution at the sub-grid scale. Nevertheless, an adaptive

grid could be useful to achieve even higher resolution near the features that sometimes split from the main eddy. An algorithm could be written to identify the regions of interest and to reduce the grid spacing there. If desired, additional particles could also be distributed in the region to further increase resolution. Furthermore, with an adaptive grid, resolution could be decreased in areas not of interest to partially offset the added computational load of the increased resolution in other areas. Since the focus of this study was the behavior of warm-core rings, and not the smaller scale phenomena around them, adaptive grid techniques were not employed. Implementing these techniques is essentially a programming task.

5.2 Model Development

The ultimate goal in this line of research is to develop a complete, two-layer PIC model. The first part of this study was to develop an improved reduced gravity PIC model. With developments to the interpolation routines, which allowed the elimination of explicit smoothing, integral invariants were conserved approximately 5 times better than in previous studies. Furthermore, the tests of the reduced gravity PIC model versus analytical and numerical solutions to the lens equation are the most stringent test of the PIC model in oceanography to date. The next phase of this research involved development of a 1.5-layer PIC model which included prescribed flow in the lower layer. This is the first such PIC model developed in oceanography. This development made possible the study of the effects of environmental flow on characteristics of warm-core rings. The generality of the PIC approach allowed new solution regimes to be discovered. The inclusion of general forcing in the lower layer was an advancement to previous (non-PIC) investigations of ring dynamics. Nof [1985], Ruddick [1987] and Brickman and Ruddick [1990] considered only environmental shear, which is just one of four parameters included in this study. Finally, the development of the two-layer PIC model is the first such model in oceanog-

raphy. The two-layer dynamics allow general flow and the inclusion of baroclinic effects. In addition, this model is capable of resolving internal and external gravity waves. There has been speculation in the literature [e.g., Kirwan and Lipphardt, 1993] that gravity waves may play a role in adjustment processes in ring dynamics. The analytic equilibrium solutions to the two-layer problem have not been previously presented in the literature. The success of the PIC model in reproducing the analytic solutions is encouraging.

5.3 Parallel Implementation

The parallel implementation of the PIC algorithm is the first of its kind in oceanography. All previous PIC models in oceanography have been implemented in serial form. This restricted several aspects of the models, the most critical one being the number of particles used. Earlier investigators [e.g., Pavia and Cushman-Roisin, 1988] were forced to compromise between resolution and computational feasibility in choosing the number of particles. The limitation on the number of particles contributed to the need for smoothing, which in turn contributed to the inability to conserve integral invariants to a satisfactory level. With the parallel algorithm, the restriction on the number of particles is essentially eliminated. By dividing the computational workload and memory requirements amongst several processors, the practicality of the PIC model is greatly enhanced. Higher resolution can be achieved by increasing the number of particles, and the total run time can be decreased several-fold. Since the two-layer model requires particles in both layers, the total number of particles is greatly increased, typically by an order of magnitude, from that of the reduced gravity and 1.5-layer models. This almost necessitates the use of distributed memory, parallel machines for the two-layer model. Currently, access to such machines is relatively easy to acquire within academic and government communities. With the currently ongoing rapid advances in computer technology,

parallel machines will likely become commonplace in the near future.

5.4 PIC modeling technique

The focus of this study was the development and implementation of a PIC model for studying the evolution of oceanic rings. However, the PIC technique can be used in a much broader range of problems in oceanography. In particular, the technique is ideal for tracking the development and evolution of fronts in the coastal ocean. The ease in which the technique handles layer outcroppings makes it ideal for such problems. Layer outcroppings are a source of great difficulty in conventional layered models. The only major hurdle remaining in implementing the model in a coastal application is the development of more complex boundary conditions. The sponge layer boundary conditions developed in this study for the two-layer model were appropriate for open-ocean conditions but would likely not be appropriate in the coastal ocean where land and topographic boundaries are important. Also, the inclusion of wind stress might prove to be important to small-scale phenomena in the coastal ocean, however, that development should be rather straightforward. If a coastal ocean PIC model were developed, it could be useful in studying events such as oil spills and the transport of pollutants. Furthermore, as military operations are currently tending towards coastal domains, a coastal PIC model could be useful in military strategic planning and operations.

6 CONCLUSIONS

The first research question posed in the introduction has been answered by the experiments with the 1.5-layer model. The model was used to determine how vorticity, normal and shear deformation in the lower, exterior layer affect the evolution of a warm-core ring. The parameter matrices presented in section 4.2 describe how these lower layer forcing components act in combination and separately to affect the behavior of the warm-core ring in the upper layer. The solutions could be classified into three regimes: the rotating ellipsoid, shedding ellipsoid, and the so-called raingutter. The final state of the first two regimes is an anticyclonically rotating ellipsoid. The end state of the raingutter solution is an elongated filament.

The studies with the 1.5-layer model also addressed the second research question. A limit to the forcing was found beyond which the lens went to the raingutter solution and then at no later time resembled a coherent vortex. The limit between the stable and unstable eddy configurations agreed favorably with Ruddick [1987], and the PIC model was able to resolve more solution regimes and include more forms of forcing than earlier studies.

The third research question posed concerned the utility of the particle-in-cell technique. The problem of resolving the time-dependent frontal boundary of a warm-core ring is difficult to solve using conventional modeling techniques. The PIC technique was shown to be ideal for such problems. First, the comparisons between the reduced gravity model and the analytical solutions to the lens equations were shown for purposes of model validation. The PIC model solutions agreed well with the analytical solutions, even though the analytical solutions had restrictions on their solution form and geometry. The PIC model conserved integral invariants to a high degree including roughly a factor of five better conservation of the energy invariant than in previous PIC studies. In addition, the 1.5-layer and two-layer

models demonstrated the utility of the PIC technique. The 1.5-layer model was used to explore a larger domain in forcing parameter space than in previous, analytical studies. A new solution regime was discovered. This regime was precluded by the restrictions inherent in earlier analytical studies of the forced problem. The two-layer model also was shown to reproduce the new analytical steady-state solutions which were derived in section 4.3.1. Solution of such problems is difficult, if not impossible, with conventional techniques.

Finally, the parallel implementation of the PIC model contributed to the practicality of the model. Model run times were reduced by more than an order of magnitude and restrictions on resolution were eliminated. Design and implementation of the parallel PIC algorithm was an effective example of the use of parallel processing supercomputers to solve practical problems in oceanography.

REFERENCES

Auer, S. J., Five-year climatological survey of the Gulf Stream system and its associated rings, *J. Geophys. Res., 92*, 11709–11726, 1987.

Ball, F. K., Some general theorems concerning the finite motion of a shallow rotating liquid lying on a paraboloid, *J. Fluid Mech., 19*, 240–256, 1963.

Ball, F. K., The effect of rotation on the simpler modes of motion of a liquid in an elliptic paraboloid, *J. Fluid Mech., 22*, 529–545, 1965.

Brickman, D. and B. Ruddick, The behavior and stability of a lens in a strain field, *J. Geophys. Res., 95*, 9657–9670, 1990.

Brown, O. B., P. C. Cornillon, S. R. Emmerson, and H. M. Carle, Gulf Stream warm rings: a statistical study of their behavior, *Deep Sea Res., 33*, 1459–1473, 1986.

Chapman, D. C., Numerical treatment of cross-shelf open boundaries in a barotropic coastal ocean model, *J. Phys. Oceanogr., 15*, 1060–1075, 1985.

Churchill, J. H., P. C. Cornillon, and G. W. Milkowski, A cyclonic eddy and shelf-slope water exchange associated with a Gulf Stream warm-core ring, *J. Geophys. Res., 91*, 9615–9623, 1986.

Cushman-Roisin, B., Frontal geostrophic dynamics, *J. Phys. Oceanogr., 16*, 132–143, 1986a.

Cushman-Roisin, B., Linear stability of large, elliptical warm-core rings, *J. Phys. Oceanogr., 16*, 1158–1164, 1986b.

Cushman-Roisin, B., Exact analytical solutions for elliptical vortices of the shallow-water equations, *Tellus, 39*, 235–244, 1987.

Cushman-Roisin, B., W. H. Heil and D. Nof, Oscillations and rotations of elliptical warm-core rings, *J. Geophys. Res., 90*, 11756–11764, 1985.

Evans, R. H., K. S. Baker, O. B. Brown, and R. C. Smith, Chronology of warm-core ring 82-B, *J. Geophys. Res., 90*, 8803–8811, 1985.

Glenn, S. M., G. Z. Forristall, P. Cornillon and G. Milkowski, Observations of Gulf Stream ring 83-E and their interpretation using feature models, *J. Geophys. Res., 95*, 13043–13063, 1990.

Harlow, F. H., The particle-in-cell computing method for fluid dynamics, *Meth. Comput. Physics, 3*, 319–343, 1964.

Hockney, R. W. and J. W. Eastwood, *Computer Simulation Using Particles*, Institute of Physics, Bristol, England, 1988.

Holdzkom, II, J. J., S. B. Hooker and A. D. Kirwan, Jr., A comparison of a hydrodynamic lens model to observations of a warm core ring, *J. Geophys. Res., 100*, 15889–15897, 1995.

Hooker, S. B. and J. W. Brown, Interpretation of warm-core ring dynamics using satellite imagery, *J. Geophys. Res., 99*, 25181–25194, 1994.

Hooker, S. B., J. W. Brown, A. D. Kirwan, Jr., G. J. Lindemann and R. P. Mied, Kinematics of a warm-core dipole ring, *J. Geophys. Res., 100*, 24797–24809, 1995.

Hurlburt, H. E. and J. D. Thompson, Coastal upwelling on a β-plane, *J. Phys. Oceanogr., 3*, 16–32, 1973.

Joyce, T. M., Velocity and hydrographic structure of a Gulf Stream warm-core ring,

J. Phys. Oceanogr., 14, 936–947, 1984.

Joyce, T. M. and M. A. Kennelly, Upper-ocean velocity structure of Gulf Stream warm-core ring 82B, *J. Geophys. Res., 90*, 8839–8844, 1985.

Joyce, T. M. and T. J. McDougall, Physical structure and temporal evolution of Gulf Stream warm-core ring 82B, *Deep Sea Res., 39*, S19–S44, 1992.

Joyce, T. M., J. K. B. Bishop, and O. B. Brown, Observations of offshore shelf-water transport induced by a warm-core ring, *Deep Sea Res., 39*, S97–S113, 1992.

Joyce, T. M., R. Backus, K. Baker, P. Blackwelder, O. Brown, T. Cowles, R. Evans, G. Fryxell, D. Mountain, D. Olson, R. Shlitz, R. Schmitt, P. Smith, R. Smith, and P. Wiebe, Rapid evolution of a Gulf Stream warm-core ring, *Nature, 308*, 837–840, 1984.

Kirwan, Jr., A. D. and B. L. Lipphardt, Jr., Coherent flows with near zero potential vorticity, *J.Mar. Sys., 4*, 95–115, 1993.

Kirwan, Jr., A. D. and J. Liu, Shallow water equations on an f-plane, in *Nonlinear Topics in Ocean Physics, Course CIX*, edited by A. R. Osborne, pp. 99–132, North Holland, Amsterdam, 1991.

Kirwan, Jr., A. D., B. L. Lipphardt, Jr., and J. Liu, Negative potential vorticity lenses, *Int. J. Engng. Sci., 30*, 1361–1378, 1992.

Kirwan, Jr., A. D., B. L. Lipphardt, Jr., and K.L. Gregory, Nonlinear ocean dynamics, in *The Oceans: Physical-Chemical Dynamics and Human Impact*, edited by S. Majumdar, E. Miller, G. Forbes, R. Schmalz, and A. Panah, pp. 40–55, The Pennsylvania Academy of Sciences, Penn., 1994.

Kirwan, Jr., A.D., C. E. Grosch, and J. J. Holdzkom II, Particle-in-cell simulations of a lens on an f-plane, *Nonlin. Proc. Geophys., 4*, 71–91, 1997.

Lipphardt, B. L., Dynamics of dipoles in the Middle Atlantic Bight, Ph.D. thesis, Old Dominion University, Norfolk, May 1995.

Mathias, B. J., Simulations of vortex evolution and interaction in a two-layer ocean with a particle method, Master's thesis, Thayer School of Engineering, Dartmouth College, New Hampshire, April 1992.

Mied, R. P., A. D. Kirwan, Jr. and G. J. Lindemann, Rotating modons over isolated topographic features, *J. Phys. Oceanogr., 22*, 1569–1582, 1992.

Nof, D., On the β-induced movement of isolated baroclinic eddies, *J. Phys. Oceanogr., 11*, 1662–1672, 1983.

Nof, D., On the ellipticity of isolated anticyclonic eddies, *Tellus, 37*, 77–86, 1985.

Olson, D. B., R. W. Schmitt, M. Kennelly, and T. M. Joyce, A two-layer diagnostic model of the long-term physical evolution of warm-core ring 82B, *J. Geophys. Res., 90*, 8813–8822, 1985.

Pavia, E. G., A numerical study of merging and axisymmetrization of oceanic eddies, Ph.D. thesis, Florida State University, Gainesville, December 1989.

Pavia, E. G. and B. Cushman-Roisin, Modeling of oceanic fronts using a particle method, *J. Geophys. Res., 93*, 3554–3562, 1988.

Pavia, E. G. and B. Cushman-Roisin, Merging of frontal eddies, *J. Phys. Oceanogr., 20*, 1886–1906, 1990.

Ripa, P., On the stability of elliptical vortex solutions of the shallow-water equations,

J. Fluid Mech., 183, 343–363, 1987.

Rogers, C., Elliptic warm-core theory: The pulsrodon, *Phys. Lett. A, 138*, 267–273, 1989.

Ruddick, B. R., Anticyclonic lenses in large-scale strain and shear, *J. Phys. Oceanogr., 17*, 741–749, 1987.

Young, W. R., Elliptical vortices in shallow water, *J. Fluid Mech., 171*, 101–119, 1986.

A APPENDIX

A.1 Initialization of the PIC model

A.1.1 Reduced gravity and 1.5-layer models

Before giving specifics of the initialization, a general scheme for initializing the height and velocity fields is described. The upper layer is first divided into regions bounded by isothickness contours. The area and volume of those regions is then calculated. Dividing this volume by the volume of a particle gives the number of particles for the region. Finally, the particles are equidistantly spaced within each region. In order to keep the number of particles per cell constant between regions of different layer thickness, the height (and thus volume) of the particles may be varied from region to region. Once the initial positions of the particles are determined, each particle is assigned an initial velocity. Since the initialization is a critical step in the model, the details of the initialization of the height and velocity fields for a typical problem are given next.

For the problems described in earlier sections the lens has initially a circular horizontal boundary with a parabolic height distribution. The non-dimensional equation for the initial lens thickness for the problems was,

$$h = h_0[1 - (r/R)^2], \tag{67}$$

where h_0 is the centerline thickness, r is the radial distance from the lens center and R is the initial radius of the lens. The volume occupied by the lens is then,

$$V_L = 2\pi \int_0^R rhdr = (\pi/2)h_0R^2. \tag{68}$$

Integration of (36) shows the volume of a particular particle to be $V_p = \Delta^2 h_p$ so the total volume occupied by the particles is,

$$V_T = \Delta^2 \sum_{p=1}^{N} h_p, \tag{69}$$

where N is the total number of particles. Clearly, $V_T = V_L$ must be required.

In order to allow the same number of particles to be in each cell, h_p must be varied with radius. To achieve an equal number of particles in each cell first note that the volume of an annulus centered at r is,

$$V_A = 2\pi \int_{r-\Delta/d}^{r+\Delta/d} rhdr = 4\pi h_0 r(\Delta/d)[1 - (r/R)^2 - (\Delta/Rd)^2], \tag{70}$$

where Δ/d is the half-width of the annulus. The number of particles required to fill this volume is,

$$N_A = V_A/V_p = 4\pi[h_0/h_p(r)](r/\Delta d)[1 - (r/R)^2 - (\Delta/Rd)^2]. \tag{71}$$

The number of cells in this annulus is the ratio of the annulus area to cell area. A simple calculation gives this number as $N_c = 4\pi r/\Delta d$. If the number of particles in each cell, $N_\# = N_A/N_c$, is to be constant, the particles' heights must be assigned as,

$$h_p(r) = (h_0/N_\#)[1 - (r/R)^2 - (\Delta/Rd)^2]. \tag{72}$$

Adjusting the height of the particles to keep the number of particles in a cell constant makes the calculation of the total number of particles a simple one. The total number of particles is simply the number of particles per cell times the ratio of the area of the lens to the area of a cell, i.e., the number of particles per cell times the number of cells covered by the lens. Thus, the total number of particles needed in the lens is,

$$N_T = N_\# \cdot \pi R^2/\Delta^2. \tag{73}$$

An important consideration with this approach is the appropriate number of particles for each cell, $N_{\#}$. Using different particle geometry and interpolation than in this study, other investigators [Pavia, 1989; Pavia and Cushman-Roisin, 1988, 1990; and Mathias, 1992] used about 15 particles per cell. However, as noted above these investigators used explicit smoothing at every time step. With the geometry and elimination of smoothing used here, $N_{\#} \sim 2.5 \times 10^2$ is appropriate. The total number of particles with this value is on the order of 10^6. Kirwan et al. [1997] demonstrated the deterioration of the solution with an order of magnitude fewer particles.

The particles are placed equidistantly within the lens, so that the radial and azimuthal distance between particles is the same and constant between all particles. Since the radial spacing is specified by the half-width of the annuli, Δ/d, and the size of each cell is fixed, the number of particles per cell is completely determined by the parameter d. A short calculation determines the number of particles per cell to be $N_{\#} = d^2/4$. For most cases reported in this study, d was taken to be 32, which yields 256 particles per cell.

Once the initial position of each particle is assigned, the lens equations (24) – (31) are used to compute the velocity appropriate for each particle. The initial velocity depends only on the initial particle position. The height of each particle is determined from (72).

A.1.2 Two-layer model

The two-layer model requires a slightly more complicated initialization routine. In the reduced gravity model and 1.5-layer models, only one layer is modeled. Thus, there is no reference level or interface between layers to be of concern. However, in the two-layer model the reference level and interface become important to the initialization. In the two-layer model, the height field in the upper and lower layers

is specified respectively as,

$$\begin{array}{lll} h_{10} = & h_0(1+\alpha)(1-(r/R)^2) & r \leq R, \\ h_{10} = & 0 & r > R, \end{array} \tag{74}$$

$$\begin{array}{lll} h_{20} = & H - h_0(1-(r/R)^2) & r \leq R, \\ h_{20} = & H & r > R, \end{array} \tag{75}$$

where H is the reference level depth, h_0 is the depth of the eddy extending below the reference level, and R is again the initial radius of the lens. The upper layer extends above the reference level by the amount $h_0\alpha$, where $\alpha = C(\rho_2 - \rho_1)/\rho_1$ and C is a constant.

As in the previous example, particles in the upper layer are initialized in annuli using radial coordinates. The height of each particle is now slightly modified to be,

$$h_p(r) = (h_0 + \alpha)/N_{\#}[1 - (r/R)^2 - (\Delta/Rd)^2]. \tag{76}$$

The lower layer is initialized slightly differently. Particles are equidistantly spaced using rectilinear coordinates. Again, a parameter, d_l, specifies the spacing between particles in both directions, and the number of particles per cell is defined by this parameter to be $N_{\#l} = d_l^2/4$. Note that there is no requirement for $d = d_l$, although in most cases presented here they were set equal. The total number of particles for the lower layer is simply the number of particles per cell times the ratio of the area of the lower layer (equal to the area of the computational domain) to the area of a cell, i.e.,

$$N_{Tl} = N_{\#l} \cdot 4L_xL_y/\Delta^2, \tag{77}$$

where L_x and L_y are the half-lengths of the domain in the x and y direction, respectively.

The height of the individual particles is determined similarly to the upper layer. Given the number of particles per cell, $N_{\#l}$, it is found from equation (75) to be,

$$\begin{array}{lll} h_{pl} = & (H - H_o(1-(r/R)^2))/N_{\#l} & \text{for } r \leq R, \\ h_{pl} = & H/N_{\#l} & \text{for } r > R. \end{array} \tag{78}$$

Initializing the upper layer radially and the lower layer rectilinearly was found to be the most successful method to approximate the analytical expressions for the height fields. Attempts to initialize the lower layer radially in the region beneath the lens and rectilinearly elsewhere were not as successful. Note that in any case it is impossible to exactly match the analytical expressions for the fields with a finite number of particles. However, the error between the analytical and numerical values is typically less than 1% with $N_{\#} \approx 2 \times 10^2$.

A.2 Decomposition and properties of the velocity field

The velocity field, **G**, described in the models may be decomposed in the following form,

$$\mathbf{G} = G/2 \begin{bmatrix} 1 & 0 \\ 0 & 1 \end{bmatrix} + \begin{bmatrix} G_N & G_S \\ G_S & -G_N \end{bmatrix} + G_R \begin{bmatrix} 0 & -1 \\ 1 & 0 \end{bmatrix} \tag{79}$$

where,

$$G = G_{11} + G_{22},$$

$$G_N = (G_{11} - G_{22})/2,$$

$$G_S = (G_{12} + G_{21})/2,$$

$$G_R = (G_{21} - G_{12})/2.$$

Here, G is the divergence term, G_N is the normal deformation, G_S is the shear deformation, and G_R is the vorticity component.

Any second-order object such as this may be rotated to new coordinates by the following transformation. Define the rotation matrix as,

$$\mathbf{R} = \begin{bmatrix} \cos\theta & \sin\theta \\ -\sin\theta & \cos\theta \end{bmatrix},$$

where θ is the angle of rotation measured counter-clockwise from the x-axis. Then, the transformation is,

$$\overline{\mathbf{G}} = \mathbf{R}^T \mathbf{G} \mathbf{R},$$

where $\mathbf{R}^T$ is the transpose of the matrix $\mathbf{R}$ and $\overline{\mathbf{G}}$ represents the velocity field in the rotated coordinates.

The following results can be obtained for the rotational properties for each of the components in (79):

$$\overline{G}/2 = G/2,$$

$$\overline{G}_R = G_R,$$

$$\begin{bmatrix} \overline{G}_N \\ \overline{G}_S \end{bmatrix} = \begin{bmatrix} \cos 2\theta & -\sin 2\theta \\ \sin 2\theta & \cos 2\theta \end{bmatrix} \begin{bmatrix} G_N \\ G_S \end{bmatrix}.$$

Table 3 presents symmetry relationships for the deformation components for various angles of rotation. Clearly, the divergence and rotational components are invariant under the rotation.

Table 3: Symmetry relationships for rotation of the deformation components.

θ	G_N	G_S
$\pi/4$	$-G_S$	G_N
$\pm\pi/2$	$-G_N$	$-G_S$
$\pm\pi$	G_N	G_S
$-\pi/4$	G_S	$-G_N$

VITA

John James Holdzkom II
Department of Ocean, Earth and Atmospheric Sciences
Old Dominion University
Norfolk, VA 23529

EDUCATION

Ph.D.	Old Dominion University Major: Oceanography	**1998**
B.S.	Old Dominion University Major: Physics; Minor: Mathematics	**1992**

AWARDS AND HONORS

The Meredith Family Scholarship, Old Dominion University, 1996 – 1997.

Outstanding Physics Graduate, Old Dominion University, 1992.

Outstanding Physics Senior, Old Dominion University, 1992.

Clifford L. and Lillian R. Adams Scholarship in Physics, Old Dominion University, 1989 – 1990, 1990 – 1991.

Alumni Honors Association Scholarship, Old Dominion University, 1988 – 1989.

SOCIETIES

American Geophysical Union
The Oceanography Society
American Meteorological Society
Sigma Pi Sigma

REFEREED PUBLICATIONS

Kirwan, A.D., Jr., C.E. Grosch, and J.J. Holdzkom II, "Particle-in-Cell Simulations of a Lens on an f-plane," Nonlin. Proc. Geophys., 1997.

Holdzkom, J.J., II, S.B. Hooker, and A.D. Kirwan, Jr., "A Comparison of a Hydrodynamic Lens Model to Observations of a Warm-Core Ring," J. Geophys. Res., 1995.

Tsonis, A.A., G.N. Triantafyllou, J.B. Elsner, J.J. Holdzkom II, and A.D. Kirwan, Jr., "An Investigation of the Ability of Nonlinear Methods to Infer Dynamics from Observables," Bull. Am. Meteorol. Soc., 1994.

This document was prepared using LaTeX.

IMAGE EVALUATION TEST TARGET (QA-3)

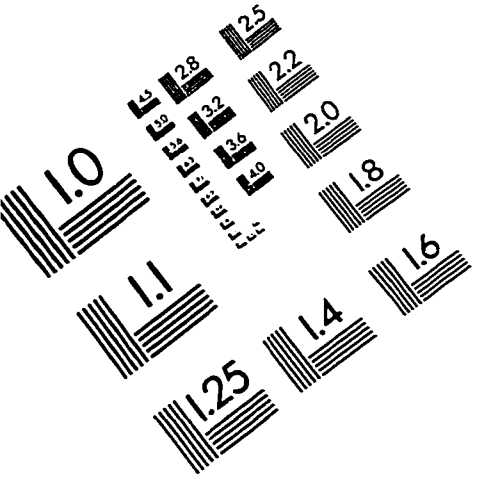

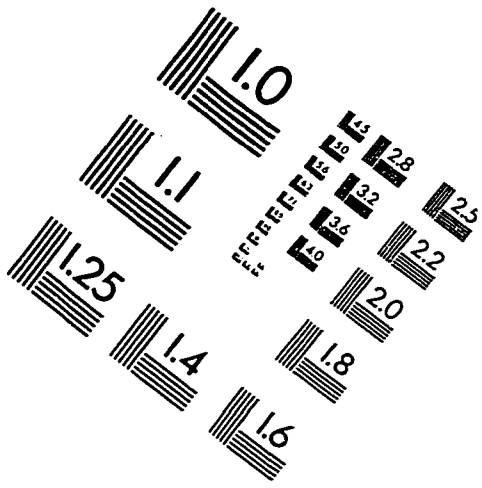

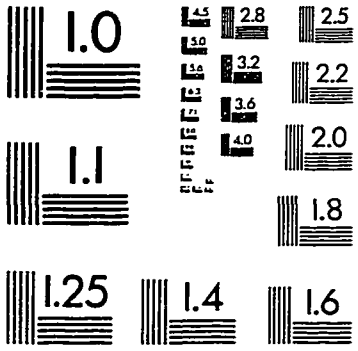

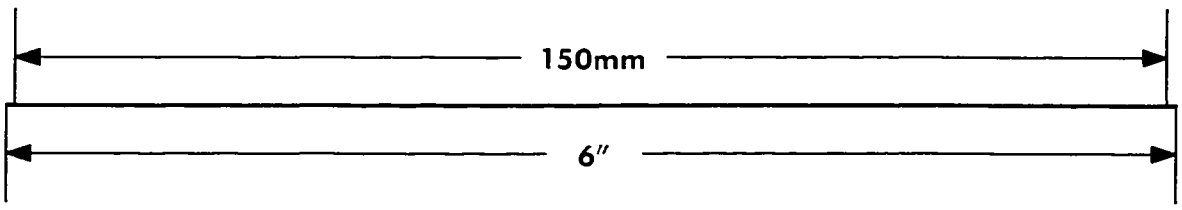

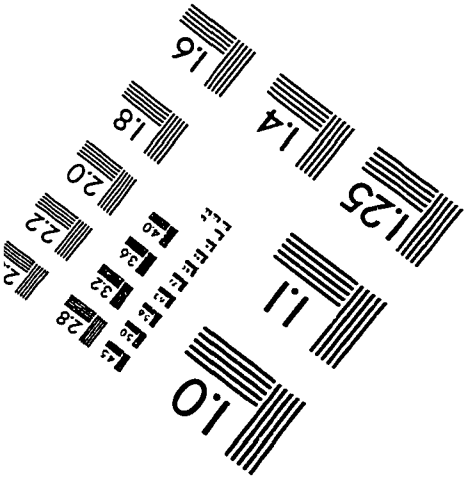

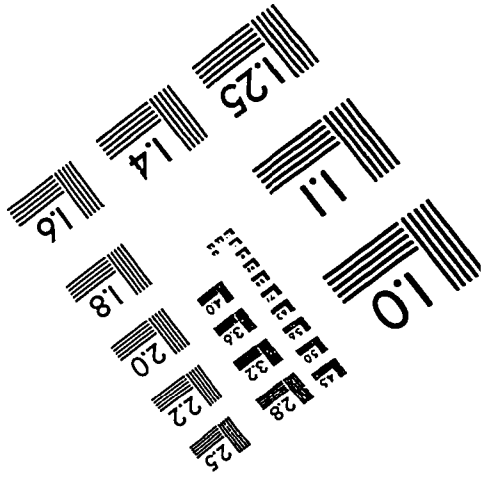

APPLIED IMAGE, Inc
1653 East Main Street
Rochester, NY 14609 USA
Phone: 716/482-0300
Fax: 716/288-5989